Thermal Hydraulics System-Level Code Validation and Transient Analyses for Fluoride Salt-Cooled High-Temperature Reactors

by

Hsun-Chia Lin

A dissertation submitted in partial fulfillment
of the requirements for the degree of
Doctor of Philosophy
(Nuclear Engineering and Radiological Sciences)
in the University of Michigan
2020

Doctoral Committee:

Professor Xiaodong Sun, Chair
Professor Richard N. Christensen, University of Idaho
Professor Krzysztof Fidkowski
Dr. Rui Hu, Argonne National Laboratory
Professor Annalisa Manera

Hsun-Chia Lin

hsunlin@umich.edu

ORCID iD: 0000-0001-7821-8112

This dissertation is dedicated to my husband, Evan,

and our families

for their support and love.

Acknowledgements

This research was performed using funding received from the U.S. Department of Energy Office of Nuclear Energy's Nuclear Energy University Program (NEUP).

Firstly, I would like to thank my advisor, Professor Xiaodong Sun, for his expert guidance, encouragement, and support in my graduate study. He is always helpful and genuinely cares about me and other students. I also want to thank Professor Richard N. Christensen for his insightful comments and encouragement. Many thanks to Dr. Rui Hu for being my supervisor during my student visiting at the Argonne National Laboratory and Dr. Chris Allison of Innovative Systems Software (ISS) for his advice during my internship at ISS.

I would also like to thank my other committee members, Professor Annalisa Manera and Professor Krzysztof Fidkowski, for their suggestions and valuable feedback on my research work. In addition, I want to thank all my friends and lab mates, Dr. Qiuping Lv, Dr. Minghui Chen, Dr. David Arcilesi, Dr. Shanbin Shi, Dr. Xiao Wu, and soon to be Drs. Sheng Zhang, Qingqing Liu, Chengqi Wang, and Xiaoqin Zhang with whom I work hard together during our Ph.D. study.

Finally, special thanks to my husband Evan and my parents, my sister, my brother, my sister-in-law and my parents-in-law. This work would not have been completed without their supports.

Table of Contents

List of Tables

List of Figures

Abstract

Verification and validation (V&V) of thermal hydraulics analysis codes for fluoride salt-cooled high-temperature reactors (FHRs) is identified as one of the key tasks that need to be addressed before FHRs can be licensed and deployed. System-level code validation of thermal hydraulics modeling in support of FHR development and licensing is the main objective of this study. The advanced high-temperature reactor (AHTR), one of the available FHR pre-conceptual designs, is the main focus of this research. FHRs feature passive heat removal capability using Direct Reactor Auxiliary Cooling Systems (DRACS) to remove decay heat during transients and accidents via natural convection/circulation flows. Due to the importance of natural circulation flows to FHR decay heat removal, the key objective of this study is to perform validation of system-level analysis codes on heat transfer performance evaluation for natural circulation flows.

Two system-level analysis codes, namely, RELAP5 SCDAPSIM/MOD 4.0 and System Analysis Module (SAM), are selected for this code validation study. Experimental data from a Purdue University natural circulation water loop and a low-temperature DRACS test facility (LTDF) using water as a surrogate for molten salts at the Ohio State University are utilized for RELAP5 and SAM code validation. An extensive test matrix is developed for the LTDF tests, including DRACS startup and pump trip scenarios. The code simulation results from RELAP5 and SAM show good agreement for fluid temperatures and mass flow rates with the experimental data.

For code validation for molten salt applications, steady-state experimental data obtained from the FLiBe natural circulation loop at the University of Wisconsin is utilized. It was found that the flow resistance in the loop is under-estimated by the SAM model. With higher flow resistance applied in the SAM model for the six tests simulated, the simulation results of the salt temperature differences across a cooler are within 27% compared to the experimental data. The correlated flow resistance is applied to this model due to potential pipe corrosion and salt freezing films near the outlet of the air cooler in the experiment. This research also identifies salt freezing model as an additional need in modeling FHRs with current system codes.

An uncertainty analysis is performed for the SAM code by investigating the effect of the uncertainties in molten salt thermophysical properties on the uncertainties of the predicted quantities of interest. From the sensitivity analysis for the high-temperature fluoride salt test facility (HT-FSTF), which adopts FLiNaK as the primary coolant, it is found that the FLiNaK viscosity and thermal conductivity have a higher influence on the salt temperature while the viscosity and specific heat capacity of FLiNaK can significantly affect the natural circulation flow velocity.

Furthermore, an AHTR reactor model is developed using the similar modeling approach in RELAP5 with a fluted-tube DRACS heat exchanger and a fluted-tube natural draft DRACS heat exchanger. Reactor normal operation and two accident scenarios, namely, station blackout (SBO) and loss of multiple DRACS loops, are analyzed. During SBO, DRACS provides sufficient decay heat removal capability, which leads to sufficient temperature margins from fuel damage and salt boiling. Overall, the simulation results show that during both transients, the reactor decay heat can be sufficiently removed by the ambient air, fully relying on passive natural circulation/convection with the proposed DRACS design in the AHTR.

Chapter 1 Introduction

1.1 Background

Currently, most of the nuclear power worldwide is generated by water-cooled reactors, that are at the second or third generation of nuclear power reactors. Fourth-generation reactors are being researched for commercialization with several advantages, such as enhanced safety, efficiency, and sustainability and reduced waste and cost. There are six main types of nuclear reactors classified as the fourth-generation reactors, including sodium-cooled fast reactors (SFRs), lead-alloy-cooled fast reactors (LFRs), gas-cooled fast reactors (GFRs), very-high-temperature reactors (VHTRs), supercritical-water-cooled reactors (SWCRs), and molten salt reactors (MSRs). The Generation IV International Forum (GIF) was initiated by the US Department of Energy (DOE) and formed in 2001 with contributed efforts from many countries to overcome increasing demands on power and to prevent nuclear proliferation (Abrams et al., 2002).

In the 1960s, the molten salt reactor experiment (MSRE) was operated for about five years from 1964 to 1969 at the Oak Ridge National Laboratory (ORNL) ref. The MSRE successfully demonstrated that a reactor design using molten salt as a coolant with nuclear fuel dissolved can be operated safely and reliably. Several decades later, molten salt cooled reactors started to receive attention globally from research institutes and industry. There are two main types of molten salt cooled reactors that differ based on the form of the reactor fuel. An MSR usually refers to a class of reactor using liquid fuel in which the uranium or thorium fuel is dissolved in the molten salt. A fluoride salt-cooled high-temperature reactor (FHR) is the solid fuel type molten-salt-cooled reactor in which the fluoride salt serves as the coolant only. Although this research mainly focuses on FHRs, many features are also shared with MSRs, such as a molten salt coolant, natural circulation flow, and a high-temperature system.

FHRs leverages improved reactor technologies, including low-pressure fluoride salt coolant, coated particle fuel (TRISO particles), and passive safety systems. This type of reactor also combines the merits of advanced reactors, such as the liquid salt of MSRs, the TRISO particle fuel of high-temperature gas-cooled reactors (HTGRs), and the passive safety system of SFRs (Forsberg, 2005 and Bardet et al., 2008). The advanced high-temperature reactor (AHTR) proposed by Oak Ridge National Laboratory is one of the most well-developed FHR designs. Advanced high-temperature reactors aim to generate 3400 MWth with a 45% thermal efficiency and fully rely on passive decay heat removal during reactor scram (Holcomb et al., 2009 and Varma et al., 2012). In an AHTR, a passive decay heat removal system – namely, a Direct Reactor Auxiliary Cooling System (DRACS) – is introduced to remove the decay heat to the ambient air by natural circulation/convection. The DRACS design concept was originally developed for EBR II (Roglans et al., 1993) and has been widely adopted in pool-type reactors, for example, SFRs and FHRs (US DOE,1980; Forsberg et al., 2003). Experimental studies using surrogate fluids on DRACS, fluidic diode, and heat exchangers have been extensively carried out for AHTR applications (Lv et al., 2015a,b; Lv et al., 2016a,b; Chen et al., 2015; Chen et al., 2016).

Fluoride salt-cooled high-temperature reactor technology has progressed rapidly since early 2000. However, no test reactor for FHR has been built. Several conceptual designs of test reactors have been developed, such as AHTRs. There are several key technical issues that need more study for FHRs or AHTRs, such as tritium control, fuel development and qualification, structural alloy development, the adequacy of models and reactor design, and so on. To accelerate deployment and FHR licensing, modeling and simulation tools in support of reactor safety analyses play an important rule. To assure the credibility of FHR safety analysis, the simulation tools are required to be verified and validated (V&V).

1.2 Challenges of Code Validation for FHRs

Though FHRs possess advanced features as described above, some challenges still remain for licensing review and reactor commercialization. Thermal hydraulics code V&V for FHR applications has been identified as one of the challenges for FHR commercialization due to the following.

- Large molten salt uncertainties of molten salt thermophysical properties: System-level analysis codes such as RELAP5 and TRACE were developed for LWRs. There were no molten salt coolants available as coolants in these codes. To perform simulations for FHRs, molten salt thermophysical properties are required to be implemented into the codes. However, uncertainties of some fluoride salt properties, for example, the thermal conductivity and dynamic viscosity, can be as high as 15-20% (Davis, 2005 and Williams, 2006).

- Lack of experimental data from molten salt test facilities and test reactors: Limited heat transfer and pressure drop correlations were developed for molten salts as working fluids. Fluoride salt-cooled high-temperature reactors are still in the design phase. Prior to operating a test reactor, scaled-down test loops should be used for demonstrating the feasibility of the design concepts. In addition, the passive heat removal system fully relies on the buoyancy force due to the fluid density difference to remove the decay heat. Therefore, accurately predicting fluid temperature is essential to determining the buoyancy force, which depends on heat transfer and pressure drop correlations used in the system-level analysis codes for modeling.

A thermal hydraulics phenomena identification and ranking table (TH-PIRT) study was performed for the AHTR (Lin et al., 2019 and Sun et al., 2017). In the TH-PIRT study, key thermal hydraulics phenomena that warrant further study and research for AHTR analysis were identified to support the validation of thermal hydraulics system-level analysis codes and computational fluid dynamics simulation (CFD) tools. Four scenarios, including station blackout (SBO), simultaneous withdrawal of all control rods, reactor core partial flow blockage, and loss of coolant accidents (LOCAs) were initially proposed as events the initiating events that could significantly affect the safety of an AHTR. Table 1 shows the phenomena have high importance to the figures of merit (FOMs) for SBO. Most of the phenomena should be included in the AHTR safety analysis.

Table 1-1. Phenomena with high importance to FOMs for SBO (Lin et al., 2019 and Sun et al., 2017).

	Figure of merits (FOMs)			
	Average temp. increases of carbonaceous material	Peak vessel temp.	DRACS salt temp. in NDHX	Peak temp. of DHX
Heat capacity of the carbonaceous (ρc_p)	H			
Heat capacity of the fuel stripe (ρc_p)	H			
Wall friction	H			
Energy generation rate in the fuel kernel		H		
Thermal properties of FLiBe		H		
Upper plenum mixing		H		
Fluidic diodicity		H		
DRACS piping (friction and form losses)		H	H	H
DRACS heat exchanger (DHX) and natural draft DRACS heat exchanger (NDHX) performance		H	H	H
Piping heat loss		H	H	H
Chimney natural circulation and performance		H	H	H
Thermal properties of $KF\text{-}ZrF_4$		H	H	H

Note: temp.= temperature H= High importance, ρ = density and c_p = heat capacity

1.3 Research Objectives

Thermal hydraulics modeling is critical for reactor safety analysis and licensing review to ensure that a reactor design is able to stay in a safe condition during reactor normal operation and transient and accident conditions. Thermal hydraulics modeling should have the ability to evaluate the decay heat removal and thermal hydraulics impacts on overall system integrity. In addition to the safety analysis, optimization of plant economic performance via thermal hydraulics analysis is essential for designing a reactor system, including pumping power, heat exchanger size, and salt inventory. Computational analyses need to be verified and validated to evaluate the code modeling applicability by comparing simulation results with analytical solutions or scaled experimental data. Furthermore, it is vital to understand the gaps and limitations of the codes in analyzing FHRs since most of the current system analysis codes have been mainly developed for light water reactors (LWRs), and need to be modified in order to be applicable to FHRs.

The objectives of this research are as follows:

- understand the capabilities of existing analysis codes, with necessary modifications, for FHR applications;
- identify additional modifications and improvements needed;
- enhance, with the improved code capabilities, understanding of the reactor response under different transient and accident scenarios in FHRs; and
- inform and improve FHR reactor designs.

1.4 Publications

Two journal papers and four conference papers are published from this research. They are listed as follows:

(a) code validation using experimental data with surrogate fluid for molten salt:

H.C. Lin, Q. Lv, S. Shi, X. Sun, R. Christensen, and G. Yoder, "Code Validation of a Scaled-down DRACS Model in RELAP5/SCDAPSIM/MOD 4.0," *Annals of Nuclear Energy*, **121**, 452-460 (2018).

H.C. Lin, R. Hu, X. Sun, "Validating System Analysis Module (SAM) Models Using Natural Circulation Experimental Data," Proc. 18th International Topical Meeting on Nuclear Reactor Thermal Hydraulics (NURETH-18), Portland, OR, August 18-23, (2019).

H.C. Lin, Q. Lv, S. Shi, X. Sun, R. Christensen and P. Sabharwall, "RELAP5 Model Validation and Benchmark for DRACS Thermal Performance," Proc. International Congress on Advances in Nuclear Power Plants (ICAPP), San Francisco, CA, USA, April 17-20, (2016).

(b) AHTR transient analysis:

H.C. Lin, S. Zhang, X. Sun, R. Christensen, "Transient Modeling of Advanced High Temperature Reactor (AHTR) in RELAP5/SCDAPSIM/MOD 4.0," 26th International Conference on Nuclear Engineering (26th-ICONE), London, UK, July 22-26, (2018).

H.C. Lin, S. Zhang, Q. Lv, X. Sun, G. Yoder, M. Perez and C. Allison, "Modeling of DRACS Test Facility and Advanced High Temperature Reactor (AHTR) Using Relap5/SCDAPSIM/MOD 4.0," 38th Annual Conference of the Canadian Nuclear Society, Saskatoon, Canada, June 3-6, (2018).

(c) FHR TH-PIRT:

H.C. Lin, S. Zhang, D. Diamond, S. Bajorek, R. Christensen, Y. Guo, G. Yoder, S. Shi, Q. Lv, X. Sun, "Phenomena Identification and Ranking Table Study for Thermal Hydraulics for Advanced High Temperature Reactor," *Annals of Nuclear Energy*, **124**, 257-269 (2019).

1.5 Dissertation Organization

There are eight chapters in the dissertation and the summaries for each chapter are as follows.

Chapter 1 introduces the background of this dissertation and outlines the objectives and challenges of this research.

Chapter 2 reviews the literature for FHR analysis and code validation on the FHR application. The design parameters of different systems in AHTRs are reviewed. The chapter also summarizes the important phenomenon identified in the thermal hydraulics PIRT for FHR.

Chapter 3 introduces the two system codes selected for code validation analyses in this study.

Chapter 4 presents the code validation results using surrogate fluids for molten salts experimental data on two test facilities, namely, a natural circulation loop at Purdue University and a low temperature DRACS test facility (LTDF) at Ohio State University (OSU).

Chapter 5 shows the code validation of SAM against data from the FLiBe natural circulation loop at the University of Wisconsin.

Chapter 6 demonstrates the uncertainty analysis of molten salt thermophysical properties with two different transients (overpower and overcooling) on the high-temperature fluoride salt test facility (HT-FSTF) at the University of Michigan. The pump trip scenario at the HT-FSTF is also predicted.

Chapter 7 provides detailed information on the RELAP5 AHTR model and also the prediction results of steady state and the two AHTR transients, including SBO and loss of multiple DRACS loops.

Chapter 8 summarizes the results, conclusions, and main contribution of this research. Future works are also suggested.

Chapter 2 Literature Review on FHR

2.1 MSR History

In the late 1940s, the molten salt reactors were developed at Oak Ridge National Laboratory's (ORNL) Aircraft Nuclear Propulsion program. The fluoride salts offer several advantages, including excellent heat transfer properties, high solubility for uranium, and stable chemical compounds. The Air Reactor Experiment (ARE) was built at ORNL using a mixture of NaF, ZrF_4, UF_4, and BeO as a fuel salt. The piping material was Inconel. No major mechanical and chemical issues were encountered during the operation. The ARE successfully operated and the steady state outlet temperature reached 860°C at power 2.5 MWth for nine days. The ARE demonstrated that UF_4 was chemically stable in the fluoride salt and the fission gas could be separated by the coolant pumps (Bettis et al., 1957, Ergen et al., 1957, Cottrell et al.,1959).

In the 1960s, the Molten Salt Reactor Experiment (MSRE) was started at ORNL, and focused on the graphite-moderated reactor design. The liquid fuel for the MSRE was a mixture of LiF, BeF_2, ZrF_4, and UF_4 (65%, 29%, 5%, and 1%). Graphite was used as the moderator. FLiBe (2liF-BeF_2) served as the secondary coolant. All piping materials and structural components were made of Hastelloy N, which was developed in the Aircraft program for a molten salt environment (Robertson et al., 1965, Prince et al., 1968 and Lindauer et al., 1969). The MSRE was constructed in 1962, with construction completed in 1964. With enriched ^{235}U as UF_4-LiF eutectic to the carrier salt, the reactor first went critical in 1965 in the first phase of the experiment. During a successful six-month operation from 1967 to 1968, it was found that there was no corrosive attack on the metal and graphite by molten fluoride fuel. The fuel was stable, and the reactor equipment was functional. In August 1968, the second phase of the MSRE was begun by extending the liquid fuel to include a substitution of ^{233}U for the fuel salt. ^{233}U zero-power experiments and dynamic tests were performed that agreed with the predicted neutronic characteristics. The MSRE operated successfully for five years, ending in December 1969 with a designed thermal power of 8 MWth. The MSRE demonstrated that the concept of liquid fuel salt is viable for nuclear reactors. The fuel salt was not affected by radiation in the reactor. The graphite in the core kept its integrity and minimal corrosion was found in the Hastelloy-N. The MSRE also used an inexpensive and on-site method to separate rare earth elements from the salt carriers. However, it has been found that Tellurium, one of the fission products, can cause the embrittlement of nickel-base structural material, including Hastelloy-N, and irradiation damage from (n, alpha) reactions. Therefore, multiple shallow cracks were found in the Hastelloy-N in the MSRE (Haubenreich et al.,1970, Shaffer et al., 1971 and MacPherson et al., 1985).

A single-fluid and graphite-moderated design molten salt breeder reactor (MSBR) was developed in the 1970s based on the experience of the MSRE. The MSBR has an increased core size to reduce neutron leakage and a reduced core power density to decrease irradiation to the moderator. ^{233}U was bred in the secondary loop that ^{233}Pa should be removed before it decays to ^{233}U. Through fluorination to UF_6, the ^{233}U can be separated from ^{233}Pa for adding to the primary fuel salt loop. However, the MSBR program was terminated, so the MSBR was never built (Bettis et al., 1970 and Robertson et al., 1971). In the early 1980s, ORNL proposed a design for a denatured molten salt reactor (DMSR), in which ^{233}U and ^{235}U were below the weight percentages of 12% and 20% of uranium, respectively. The DMSR also featured a larger core and lower power density that could extend the lifetime of graphite (Engel et al., 1980).

In 2002, the molten salt reactor was determined to be one of six Generation IV nuclear reactors. Therefore, MSRs have received a lot of attention and increasing interest from research institutes and nuclear industries globally. Molten salt features high heat capacity and excellence in heat transfer, so work including liquid salt has expanded to develop and demonstrate advanced nuclear reactor technology. Utilizing molten salt as a coolant and TRISO particles as a fuel design was proposed in recent molten-salt-cooled reactors, also known as FHRs, with solid fuel or pebble fuel design. In 2004, the AHTR concept was developed in collaboration with ORNL, Sandia National Laboratories, and the University of California at Berkeley to provide robust and innovative technology to achieve higher power outputs and provide the potential for highly competitive economics (Ingersoll et al., 2004 and Peterson et al., 2006). Two integrated research projects (IRPs) were funded by DOE-NE and led by the Massachusetts Institute of Technology (MIT) and the Georgia Institute of Technology (GT). The MIT-led IRP focused on developing PB-FHR (Andreades et al., 2016 and Scarlat et al., 2017), while the GT-led IRP mainly references AHTR design (Zhang et al., 2019). In 2011, the China Academy of Sciences started to work on a thorium-breeding molten-salt reactor (Th-MSR or TMSR) and cooperated with the US Department of Energy on the program. Commercialization of the TMSR is expected in the 2030s (Zou et al., 2018). Overall, after 2005, several pre-conceptual and conceptual designs for FHR concepts have been conducted. These designs include an AHTR (Varma et al., 2012 and Holcomb et al., 2013) and a SmAHTR (Greene et al., 2010) an FHR demonstration reactor (DR) from ORNL (Brown et al., 2017), a PB-FHR from the University of California Berkeley (Andreades et al., 2016 and Scarlat et al., 2017), and an FHR test reactor design developed at MIT(Stempien, 2015 and Sun et al., 2017). Besides the research activity on FHRs in research institutes, molten-salt-cooled reactor designs are under development in nuclear industries, such as Terra Power's molten chloride fast reactor (MCFR), the Kairos Power FHR (KP-FHR), the Moltex stable salt reactor (SSR), the FLiBe liquid fluoride thorium reactor (LFTR), the Terrestrial Energy Integral MSR, the ThorCon MSR, the Elysium Molten Chloride Salt Fast Breeder Reactor (MCSFR), and so on.

2.2 Literature Review

Compared to LWRs, the phenomenology of thermal hydraulics in FHR is unique, such as high Prandtl number in molten salt, are highly dependent on natural circulation flow as a safety mechanism, material geometry deformation under temperature change, salt freezing, and radiative heat transfer (Scarlat et al., 2017). Sabharwall et al. identified several technical challenges for commercializing advanced reactors such as AHTRs. For challenges in thermal hydraulics, code should have the capability to understand bypass flow, graphite thermo-mechanics, and fluid flow in the AHTR fuel region. Also, coupled thermal hydraulics and multi-physics codes are needed to capture the relevant physics and heat transfer from the fuel to the coolant during the transition from turbulent to laminar flow in AHTRs. Scaled thermal hydraulics experimental data with uncertainties reported should be used to support code V&V activities (Sabharwall et al., 2013).

To understand the responses of FHRs under different scenarios, several plant-level safety analyses are carried out for the different reactor designs. The development of system-level models also helps in optimizing the system component designs and evaluating their performance. A scaled

PB-AHTR model was developed in the RELAP5-3D code for analyzing the steady-state conditions and transient problems. The results of transient analyses show that DRACS is capable of maintaining the peak coolant temperature below the safety limits during accidents (Galvez., 2011). The study also points out that the problem of overcooling can be prevented by controlling the air flow rate. The TRAC/RELAP Advanced Computational Engine (TRACE) was developed by the US Nuclear Regulatory Commission (NRC) for analyzing transient and steady-state neutronic-thermal-hydraulic behaviors in nuclear reactors (NRC, 2007). The AHTR model simulated by the TRACE code is utilized for developing the design for AHTRs and performing the transient analyses (Wang et al., 2015). Steady-state normal operation and loss of forced flow (LOFF) transient are simulated using the TRACE code, and the steady-state results agree with the design values. However, the authors stated that the implemented correlations for heat exchangers were mainly for low the fluids of Prandtl numbers, and experiments would be needed to validate the correlations for molten salts of relatively large Prandtl numbers. Additionally, Verma et al. investigated the heat losses and structure temperatures during various transients in AHTRs (Varma et al., 2012). Two thermal shields are utilized for the reactor silo cooling system to reduce the heat losses to the silo wall from 15 to 5 MW. The response of an AHTR to an accident has been analyzed with passive decay heat removal by DRACS and through two thermal shields. The results indicate that the emissivity of the surfaces of those shields significantly affects the heat loss rate.

Tritium is one of the concerns of FHRs since the production rate is expected to be significantly higher than that in the light water reactors by several orders of magnitude. A double-wall heat exchanger with sweep gas is proposed by Zhang et al. to decrease the tritium leakage rate. Zhang et al. (2018) built models of a heat transfer sub-model and a mass transport sub-model to benchmark the heat exchanger model against experimental data. For the heat transfer sub-model using water as a coolant, the discrepancies for the predicted temperatures and heat transfer coefficients compared with their individual experimental data are less than 16% and 24% respectively. For the mass transport sub-model from a hydrogen separation experiment, the relative discrepancies between the model predictions and the experimental data are 23–44%. The authors suggested that other factors, such as thermal stress, susceptibility to creep, and manufacturability should be extensively investigated for the heat exchanger design for FHRs.

The University of California at Berkeley has designed separate and integral effects test facilities to investigate pebble bed heat transfer and natural circulation flow using a simulant coolant that has a similar Prandtl number as FLiBe. It is suggested that the new correlation should be established for pebble beds due to disagreement between current correlations and experimental data. A compact integral effect facility (CIET) was built for testing in forced flow and natural circulation conditions. The working fluid for representing fluoride salts in low temperature tests in CIET test bay is the Dowtherm A oil, due to similar Prandtl numbers in both fluids. Code V&V for RELAP5-3D and FANCY has been performed in both a DRACS loop alone and coupled loops. The simulation results show that both codes are in good agreement with mass flow rates – within 13% of experimental data of steady-state natural circulation in CIET (Zweibaum et al., 2015).

To demonstrate that SAM is applicable for modeling MSRE, the analyses of MSRE for code-to-code comparison were performed, including zero power physics tests, the fuel pump start-up, pump coast down tests, and the natural circulation transient (Leandro et al., 2019). In the SAM MSRE hydraulic mockup, the simulation result of SAM is within a 6% difference from the experimental data. For the second complete MSRE primary loop model, the primary coolant temperature distribution at different axial positions in the primary loop matched the expected axial coolant temperature change from historical calculations by Engel and Haubenreich (Engel et al., 1962). However, for the loss-of-flow transient simulation in MSRs, the authors state that that neutronics coupling is needed to improve the model's delayed neutron precursor drift and reactivity feedback changes, which are also affected by temperature in the core.

Liquid-salt coolant thermophysical properties have been reported in the literature, along with their uncertainties of 2- 20% (Davis, 2005 and Williams, 2006). A methodology was developed by Romatoski (2019) to incorporate a Monte Carlo statistical sampling uncertainty propagation and limiting safety systems settings (LSSS) approach for thermal-hydraulic safety analysis for FHRs. To compare operating regions and maximum power, the model has been used for TMSR-SF1 pebble bed design and MIT's transportable FHR prismatic core design with FLiBe (LiF-BeF2) and nafzirf (NaF-ZrF4) as coolants and under different flow conditions. The study demonstrates thermal conductivity dominates in the prismatic design, while convection affects the pebble bed more. This research also revealed that the pebble bed is more attractive than a prismatic fuel design for thermal-hydraulic safety (Romatoski et al., 2019).

Previous research related to FHRs was reviewed. However, the research gap of existing system-level codes is lack of validation with experimental data using molten salt as the working fluid especially in natural circulation. Recently, natural circulation molten salt experimental data is published (Britsch, 2019) and code validation can finally be performed.

2.3 Overview of the AHTR Plant Design

The introduction to AHTR design as follow focuses on thermal hydraulics related design, including core, reactor vessel, reactor coolant systems, and reactor safety system in the AHTR. AHTR is an FHR design concept developed by ORNL with a thermal power output of 3400 MW (Varma et al., 2012 and Holcomb et al., 2011). There are three primary loops and three intermediate loops that are coupled to a supercritical steam power cycle in AHTR as shown in Figure 2-1. Based on thermal hydraulics and neutronics features, the molten salt FLiBe ($2LiF-BeF_2$) is designed as the AHTR primary coolant, while a mixture of KF and ZrF_4 featuring a low melting point is used as the intermediate coolant. For decay heat removal, three DRACS loops in AHTR are the main path via natural circulation/convection flow. The DRACS also employs $KF-ZrF_4$ as the coolant in the DRACS circuit that is coupled to the ultimate heat sink, the ambient air.

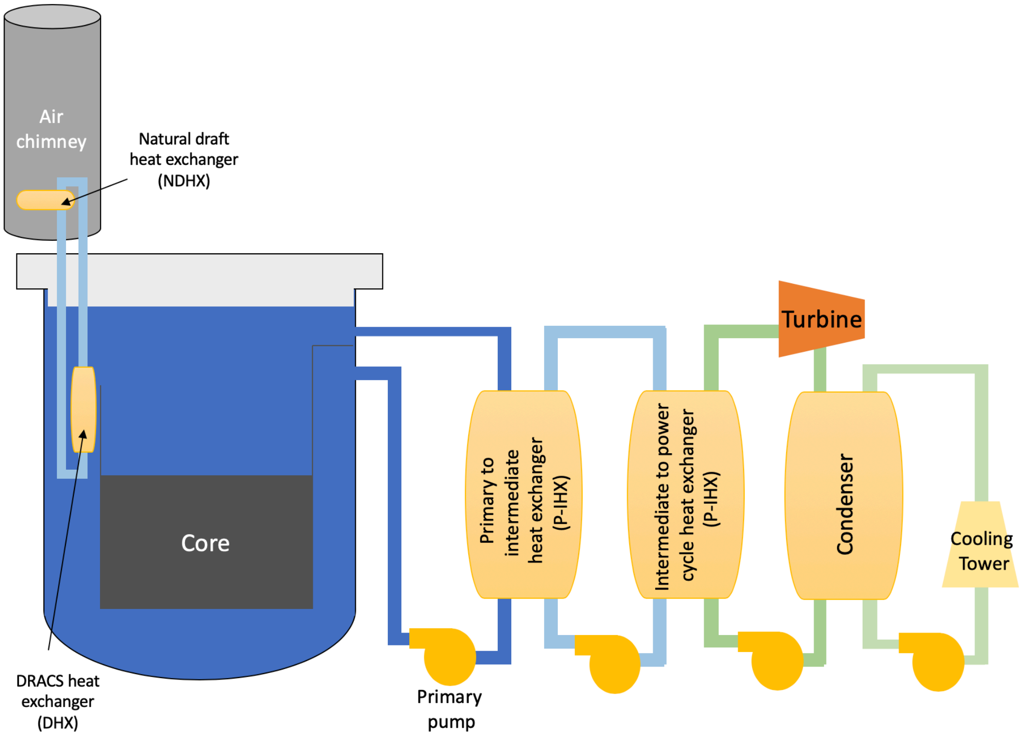

Figure 2-1. A schematic of AHTR

During reactor normal operation, the forced flow provided by the primary pump first enters the reactor vessel, flowing downward in the downcomer to lower plenum, flowing upward and being heated up in the core region, and then returning to the primary to the intermediate heat exchanger (P-IHX). The primary coolant exchanges heat with the intermediate coolant in the P-IHX and transfers heat to the supercritical steam power cycle. There is also a portion of forced flow passing the DRACS heat exchanger (DHX) from lower plenum to upper plenum, transferring heat to the DRACS coolant and maintaining it in the liquid state. The passive flow controllers, fluidic diodes are employed in each bypass channels to limit this parasitic flow (upward flow) by large flow resistance and, accordingly, the parasitic heat loss into the DRACS during reactor normal operation. Upon the loss of the forced flow and reactor shutdown, a natural circulation flow will develop in the downward flow direction in the bypass channel with low flow resistance in the fluidic diode.

Table 2-1 lists the AHTR design parameters. Due to limits regulated by the ASME code for the structural materials, the average core outlet temperature for AHTR design is limited to 700 ^{o}C. One of the safety features of AHTR is the atmospheric operating pressure in the salt loop due to the high melting point of molten salt. For the fuel design, the AHTR utilizes the TRISO particle with a fuel enrichment of 9.00 wt%. Detail design parameters of the reactor core, heat transfer loop designs, and safety systems are provided in the following sections. (Holcomb et al., 2011 and Varma et al., 2012).

Table 2-1. AHTR general design parameters (Varma et al., 2012)

Design Parameter	**Value**
Core Thermal Power/ Net Electrical Power (MW)	3,400/ 1,530
Fuel Type	TRISO
Fuel Enrichment (wt%)	9
Primary Coolant Salt	FLiBe
Core Inlet /Outlet Temperature (^oC)	650/700
Primary Coolant Flow Rate (kg/s)	28,500
Primary Coolant Pressure	Atmospheric
Number of Primary/ Intermediate / DRACS Loops	3/3/3
Intermediate Coolant Salt	$KF-ZrF_4$
Intermediate Loop Cold /Hot Leg Temperature (^oC)	600/675
Intermediate Coolant Flow Rate (kg/s)	43,200
Intermediate Coolant Pressure	Atmospheric
Fluid to High Pressure Turbine	Supercritical Steam
Turbine Supply Temperature (^oC)	650
Turbine Supply Pressure (MPa)	24
DRACS Loop Coolant	$KF-ZrF_4$
DRACS Loop Pressure	Atmospheric
DRACS Heat Sink	Air
Single DRACS Loop Maximum Power (MW)	8.75

The AHTR neutronics preconceptual design was originally developed by Holcomb et al. (2011) and subsequently revised by Varma et al. (2012). The fuel enrichment value was 19.75 wt% that has been lowered to 9 wt%. Also, the carbon-to-heavy metal (CHM) atomic ratio has been enhanced from 200 to 400 for lower fuel costs. A higher density carbonaceous matrix material (1.75 kg/m^3) has been employed in the new design to achieve a higher discharge burnup. The updated AHTR baseline neutronics design are summarized in Table 2-2.(Holcomb et al., 2011; Varma et al., 2012).

Table 2-2. AHTR neutronics design characteristics (Varma et al., 2012)

Parameter	**Value**
Assembly Lattice Type	Hexagonal
Fuel Type	TRISO
Moderator and Reflector	Graphite
Core Height (including axial reflector) (m)	6.0
Core Diameter (including radial reflector) (m)	9.56
Average Power per Grain (MW/particle)	77
Average Power Density in Fueled Region (W/cm^3)	97
Volumetric Core Power Density (MW/m^3)	12.9
Mass of Heavy Metal (fresh core) / Mass of Fissile (MT)	17.48/1.6
Fuel Cycle Length (once-through, no BP/ with BP) (years)	0.80/0.72
Fuel Residence Time in Core (two batch) (years)	1.0
Average Fuel Discharge Burnup (GWd/MT-heavy metal)	71
Maximum Fuel Temperature (average assembly) (°C)	837

2.3.1 Reactor Vessel

The candidate material for the AHTR reactor vessel is Incoloy 800H, which can yield strength of 20 MPa at 700ºC. Inside of the reactor vessel, a 1-cm-thick of Hastelloy N liner is applied to prevent potential corrosion attack by the FLiBe. AHTR is a high temperature system, therefore, thermal expansion is one of the concerns. To minimize the vessel stresses due to thermal expansion, the reactor vessel is designed to hang from its upper flange, as shown in Figure 2-2. The flange design with a diameter of 11.6 m and a thickness of 35 cm is shown in Figure 2-3. The parameters of the reactor vessel are listed in Table 2-3. Outside of the reactor vessel is the reactor guard vessel that can prevent loss of primary salt. Even when failure of the reactor vessel, the salt level of FLiBe can still be kept inside the guard vessel and still cover the reactor core to prevent core exposure. The reactor guard vessel is surrounded by a concrete silo. The gaps between the reactor vessel, guard vessel and silo wall are filled with a noble gas, such as argon.

Table 2-3. AHTR reactor vessel design parameters (Varma et al., 2012)

Parameter	Value
Exterior Vessel Diameter (m)	10.5
Vessel Height (m)	19.1
Primary Salt Depth Above Upper Support Plate (m)	7.15
Primary Piping Interior Diameter (m)	1.24
Primary Salt Mass (MT)	3,076
Core Barrel Material	C-C Composite
Vessel and Primary Piping Material	Incoloy 800H w/Hastelloy N Lining
Number of Fuel Assemblies	252
Upper and Lower Core Support Plates	SiC-SiC Composite

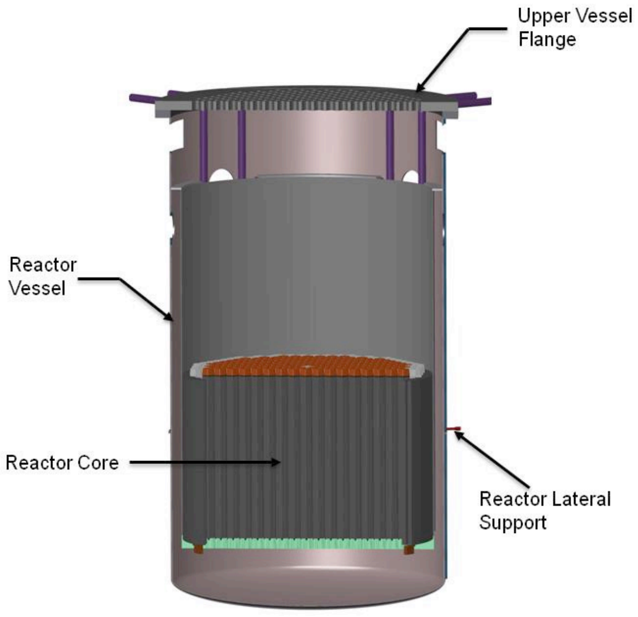

Figure 2-2. Sectional view of the AHTR reactor vessel (Varma et al., 2012)

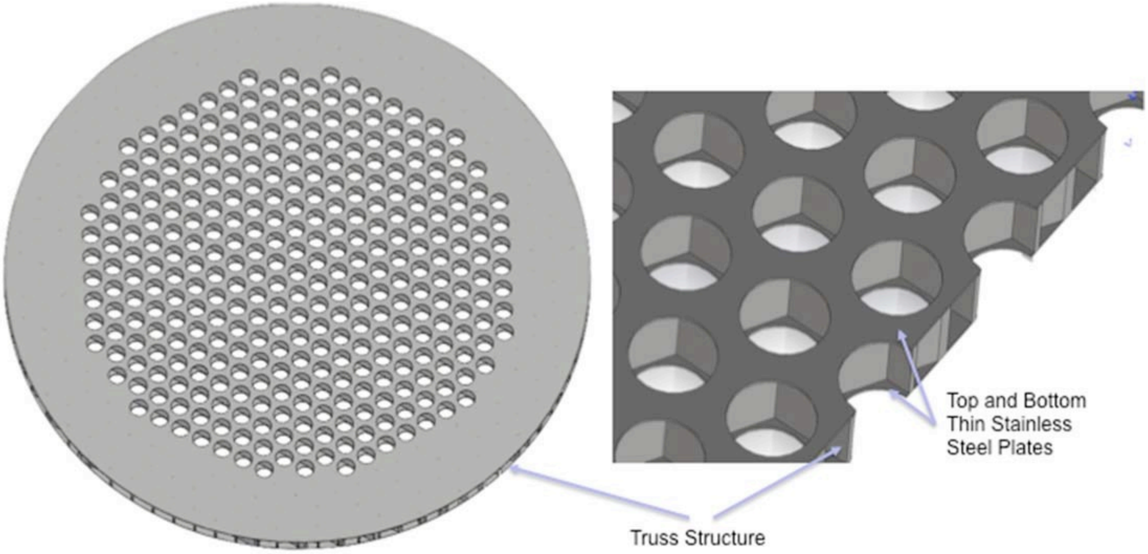

Figure 2-3. Top flange of the AHTR reactor vessel (Varma et al., 2012)

2.3.2 Reactor Core

As shown in Figure 2-4, the reactor core consists of 252 hexagonal fuel assemblies surrounded by replaceable reflector assemblies made of graphite. Outside of the replaceable reflector assemblies are a permanent graphite reflector. The core barrel encloses fuel assemblies and reflector assemblies with a 2-cm thick carbon-carbon (C-C) composite. The annulus formed between the barrel and reactor vessel is vertically divided into eight compartments, including three downcomer regions, three DRACS heat exchanger regions (bypass channels), one maintenance cooling system, and one refueling lobe, as illustrated in Figure 2-5.

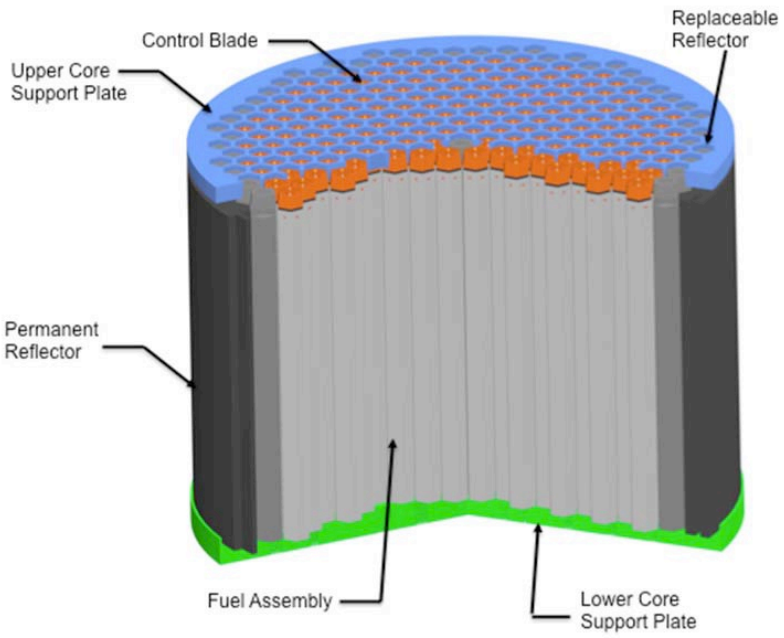

Figure 2-4. Cross-sectional view of the reactor core (Varma et al., 2012)

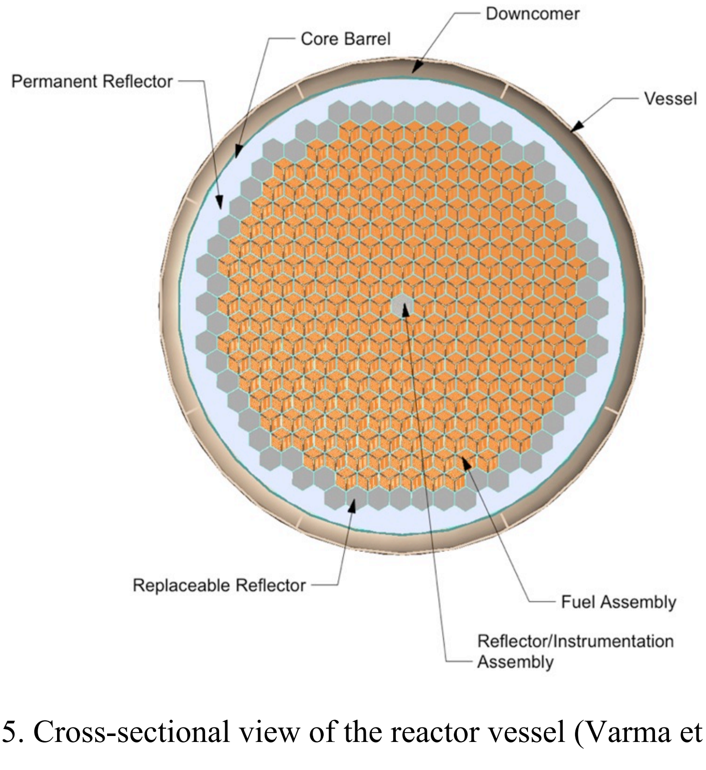

Figure 2-5. Cross-sectional view of the reactor vessel (Varma et al., 2012)

Table 2-4. Geometric parameters of the AHTR reactor core (Varma et al., 2012)

Parameter	**Value**
Equivalent Core OD (fueled region) (m)	7.81
Equivalent Replaceable Reflector OD (m)	8.69
Equivalent Permanent Reflector OD (m)	9.56
Boron Carbide Layer OD (m)	9.58
Barrel OD (m)	9.62
Core Height (fueled region) (m)	5.5
Core Height (including axial reflector) (m)	6.0
Vessel OD (m)	10.50

2.3.3 Fuel Assembly

In fuel assembly, there are eighteen fuel plates enclosed in a hexagonal prismatic box made of C-C composite. The length for each fuel assembly is 6-m. In Figure 2-6, the eighteen fuel plates with a thickness of 2.55 cm each are divided into three sections with a Y-shaped C-C composite structure. The gaps between two fuel plates (0.7-cm-wide) and between fuel plates and assembly box (0.35-cm-wide) are the flow channel for the primary salt. In addition, the gap between the two neighboring fuel assemblies is 1.75 cm thick. The Y-shape vacancy in the center is for the control rod/blade insertion. The geometric parameters of the fuel assembly are listed in Table 2-5.

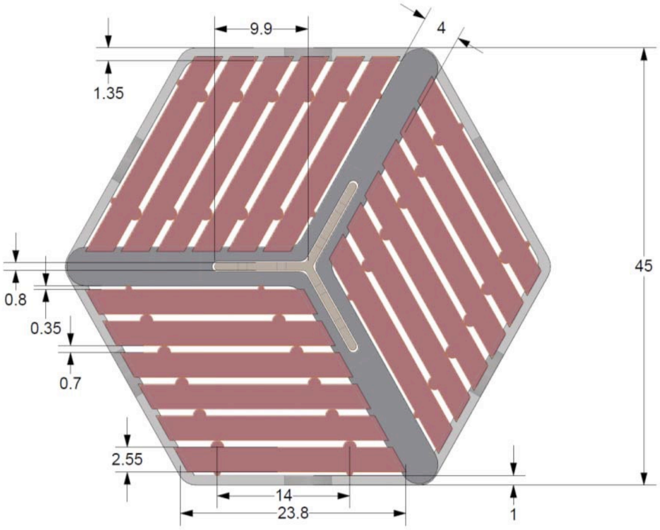

Figure 2-6. Cross section of the fuel assembly, Unit: cm (Varma et al., 2012)

Table 2-5. Geometric parameters of the AHTR fuel assembly (Varma et al., 2012)

Parameter	**Value**
Total Height (m)	6.0
Fueled Region Height (m)	5.5
Fuel Assembly Pitch (m)	0.47
Outer Apothem (m)	0.23
Channel Box Wall Thickness (cm)	1
Y-structure Thickness (cm)	4
Coolant Thickness between Plates (cm)	0.7
Coolant Thickness between Plate and Wall (cm)	0.35
Fuel Plate Thickness (cm)	2.55
Number of Fuel Plates	18

2.3.4 Reactor Coolant Systems

During reactor normal operation, the heat generated from the core is transfer through, the P-IHX, and the primary salt pump. The three primary loops are coupled with three intermediate loops through the P-IHX's to power conversion cycle. The piping in both primary and intermediate loops are made of Hastelloy N (Varma et al., 2012). For the primary loop, each pipe has an inner diameter of 1.24 m with a total length of 25 m including the hot leg and the cold leg (Wang et al., 2015). Other more detailed design parameters are summarized in Table 2-6. However, there is still no specific design for P-IHX. The shell and tube heat exchanger is proposed as the candidate design for P-IHX by Wang et al. (2015), where the design parameters can be found in Table 2-7.

Table 2-6. P-IHX design parameters and coolant thermal properties (Wang et al., 2015)

Parameter	**Primary Loop**	**Intermediate Loop**
Coolant Salt	$2LiF\text{-}BeF_2$	$53\%KF\text{-}47\%ZrF_4$
HX Inlet Temperature (K)	973	873
HX Outlet Temperature (K)	923	948
Coolant Flow Rate (kg/s)	9,500	14,400
Coolant Specific Heat Capacity (J/kg-K)	2,416	1,051
Coolant Prandtl Number	13.32	12.95

Table 2-7. P-IHX design (Wang et al., 2015)

Parameter	**Shell Side**	**Tube Side**
Loop Allocation	Primary	Intermediate
Coolant Salt	$2LiF\text{-}BeF_2$	$53\%KF\text{-}47\%ZrF_4$
Tube Length (m)	-	20.0
Tube ID (cm)	-	1.9735
Tube Wall Thickness (cm)	-	0.1245
Number of Tubes	-	18,000
Tube Pitch (cm)	-	1.5 OD
Tube Arrangement	-	Square array
Shell Inside Diameter (m)	5.18	-
Baffle Spacing (m)	2.0	-
Baffle Cut	25%	-

2.3.5 DRACS Cooling System

During accident conditions, the decay heat from the core is mainly removed by three DRACS loops in AHTR via natural circulation/convection. Each DRACS is capable of removing 0.25% (8.5 MWth) of the nominal core power. The schematic of the DRACS system is shown in Figure 2-7. There are two heat exchangers in each DRACS loop, namely, DHX and natural draft DRACS heat exchanger (NDHX), that can transfer heat from the reactor core to the ambient air.

The DHX locate in a bypass channel where the primary side is coupled with the AHTR primary salt system. The DHX tube side and NDHX tube side are in the DRACS loop which uses KF-ZrF_4 as the coolant due to lower freezing temperature compared to other molten salts. The NDHX is in a higher elevation than DHX which can benefit the formation of natural circulation in the DRACS loop. AHTR also consists of three air chimneys for each DRACS loop with NDHX located inside, the air flow also fully relies on natural convection to remove heat to the ambient air. However, there is still no finalized design for DHX and NDHX at this stage.

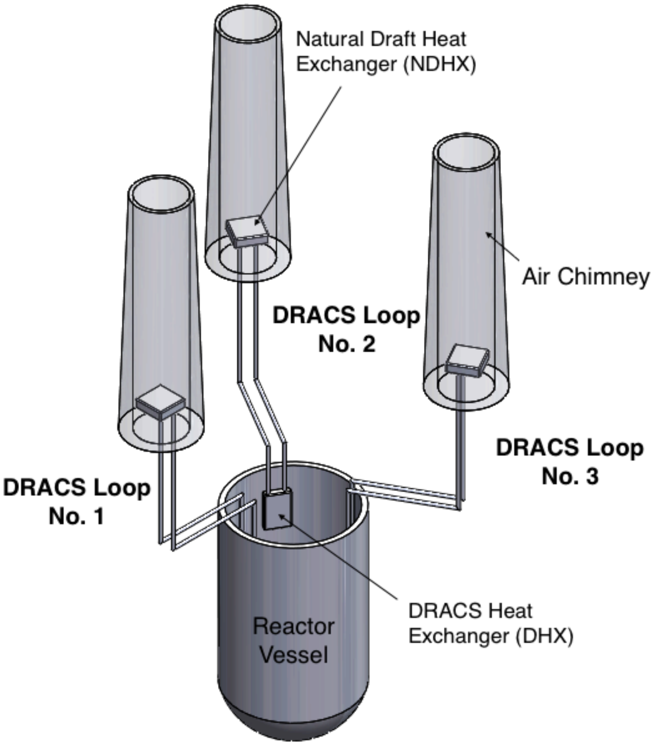

Figure 2-7. Schematic of DRACS in AHTR

2.3.6 Maintenance Cooling System

In addition to the passive heat removal system, the active cooling system i.e. maintenance cooling system is also designed to remove heat during accidents when electricity is available or during reactor maintenance. The heat exchanger of the maintenance cooling system locates in one of the eight bypass channel that uses forced air flow to remove heat. The heat removal capability of the maintenance cooling system is able to remove 5% of the nominal core power (170 MWth).

2.4 FHR TH-PIRT

PIRT has been widely used in the nuclear industry for reactor design and analysis. The final output of PIRT is phenomena ranking tables are the results from an expert elicitation process. The aim of the TH-PIRT is to support FHR modeling, safety analysis, and ultimately licensing by identifying key phenomena that potentially impose significant challenges on thermal hydraulics modeling and simulation of an FHR reference design, i.e., AHTR. A workshop organized by the Ohio State University and ORNL was held on May 24-26, 2016, for the panelists to develop the TH-PIRT for the AHTR (Sun et al., 2017 and Lin et al., 2019). The TH-PIRT for the AHTR adopted the PIRT process for LWRs and the next generation nuclear plant (NGNP) developed by the U.S. Nuclear Regulatory Commission (NRC) (Wilson et al., 1998; Fletcher et al., 2006 and Ball et al., 2008). The FHR TH-PIRT panel was assembled with experts from regulators, industries, national laboratories, and academia. The TH-PIRT panel consisted of fifteen experts specialized in salt reactor technologies, reactor thermal hydraulics, and code and methods development. In the FHR TH-PIRT panel, the panelists determined gaps in experimental databases, modeling, and analysis to validate simulation tools and methods, identified and ranked safety-relevant phenomena that impact the fidelity and accuracy of thermal hydraulics analysis for the AHTR. The TH-PIRT study also provided guidance and insights in designing experiments including separate-effect and integral-effect tests for thermal hydraulics codes validation. The FHR TH-PIRT consists of study process, scenario description, phenomena identification and ranking, knowledge level ranking, and suggested path forward. The TH-PIRT mainly focuses on two events, namely station blackout (SBO) and simultaneous withdrawal of all control rods, which were considered by the panelists as the two of the most important scenarios for reactor safety evaluation of the AHTR.

2.4.1 Identified Phenomena with Systems in AHTR

The phenomena are identified by the panelists and classified into different tables based on the systems and components in the AHTR as follows:

System: Core: fuel and primary coolant

Phenomena:

- Heat capacity of the carbonaceous materials
- Thermal conductivity of the carbonaceous materials
- Heat capacity of the fuel stripe
- Thermal conductivity of the fuel stripe

- Heat capacity of the fuel kernel
- Thermal conductivity of the fuel kernel
- Geometry of the fuel plate
- Energy generation rate in the fuel kernel
- Energy generation rate outside the kernels but within the fuel plates
- Radiative heat transfer
- Surface condition
- Fuel temperature coefficient of the reactivity
- Assembly (graphite) coefficient
- Heat capacity of FLiBe
- Thermal conductivity of FLiBe
- Viscosity of FLiBe
- Core heat transfer coefficient
- Optical properties
- Form loss coefficients
- Wall friction
- Core flow asymmetry
- Bypass flow fraction
- Direct energy deposition

System: Reactor vessel/internals/cavity: upper plenum, lower plenum, fluidic diode, reactor vessel, and cavity

Phenomena:

- Upper plenum mixing
- Fluidic diodicity
- Cover gas entrainment
- Thermal heat capacity of the vessel
- Thermal conductivity of the vessel
- Heat transfer to the upper plenum structures
- Heat transfer to the fusible links
- Heat transfer coefficient to the vessel wall
- Friction factor on the vessel wall in the downcomer
- Mixing in the lower plenum
- Heat transfer to the cover gas and vessel top flange
- Thermal properties of the insulation
- Heat transfer across the vessel to the gas space
- Heat transfer across the second gap to the concrete
- Conduction in the concrete

System: Primary loop: pump, piping, and tube side of the primary to the intermediate heat exchanger (P-IHX)

Phenomena:

- Pump performance
- Pump resistance or the *K* factor
- Form losses in the loop
- Wall friction in the loop

- P-IHX performance
- Heat losses through and from, the thermal inertia of piping
- Impact of the cover gas entrainment on the pump

System: Intermediate loop: pump, piping, and shell side of the P-IHX, tube side of the intermediate to power cycle heat exchanger (I-PHX)

Phenomena:

- Pump performance
- Pump coastdown
- Pump resistance or the *K* factor
- Form losses in the loop
- Wall friction in the loop
- I-PHX performance
- Heat losses from piping
- P-IHX performance

System: Power conversion loop

Phenomena:

- I-PHX performance
- Power cycle performance

System: DHX, NDHX, DRACS salt, chimney, and piping

Phenomena:

- DRACS piping
- DHX performance
- NDHX performance
- Piping heat losses
- Chimney natural circulation and performance
- KF-ZrF_4 thermophysical properties
- Thermal inertia of DRACS and chimney

2.4.2 FOMs for Two Events

FOM defines the evaluation criterion. Since FOMs depend on the scenario, each scenario has different FOMs.

For the event of SBO, four FOMs were identified:

- the peak vessel temperature
- DRACS coolant temperature in the NDHX
- peak temperature of the DHX
- the average temperature increase of the carbonaceous materials in the core.

For the event of simultaneous withdrawal of all control rods, two FOMs were identified:

- the hot-leg salt temperature

- maximum kernel temperature

2.4.4 PIRT Summary

Phenomena identification, importance rankings, and knowledge level rankings were carried out during the TH-PIRT study. Experts suggested that further research is required to increase our knowledge levels, improve the current AHTR design, and perform design evaluation and safety analysis for the AHTR. Besides, the panel strongly suggested CFD simulations and system-level analyses or coupled with neutronics analysis should be performed to demonstrate AHTR safety margin quantification during reactor normal operation as well as transient and accident events.

Form the FHR TH-PIRT for the event of SBO, the following phenomena are categorized that need further investigation:

- Geometry of the fuel plates, i.e., those deviations from their original geometry
- Thermal conductivity of FLiBe
- Viscosity of FLiBe
- Wall friction in the core
- Core flow asymmetry
- Upper plenum mixing
- Fluidic diodicity
- Lower plenum mixing
- DHX performance

- NDHX performance
- DRACS piping heat loss
- Chimney natural circulation and performance
- KF-ZrF_4 thermo-physical properties

Also, the following phenomena are recommended for further investigation form the FHR TH-PIRT for the event of simultaneous withdrawal of all control rods:

- Thermal conductivity of the carbonaceous materials
- Thermal conductivity of fuel stripe
- Thermal conductivity of FLiBe
- Viscosity of FLiBe
- Core heat transfer coefficient
- Primary coolant flow bypass fraction
- Upper plenum mixing
- Heat transfer to fusible links for the control rods
- Primary pump performance
- P-IHX performance
- Intermediate pump performance
- I-PHX performance
- Power cycle performance

Chapter 3 System Level Codes for Code Validation

3.1 RELAP5/SCDAPSIM/MOD 4.0

RELAP5/SCDAPSIM/MOD 4.0 is a one-dimensional system code being developed by Innovative System Software (ISS), LLC and under the SCDAP Development Training Program (SDTP). More than 90 organizations in 30 countries are included in the SDTP. Innovative System Software is mainly responsible for the code configuration control and code distribution. RELAP/SCDAPSIM development is based on code previously developed by the US Nuclear Regulatory Commission, including RELAP5 MOD 3.3 and RELAP5 MOD 3.2. The code can be used to simulate reactors under different conditions such as normal operation, transients, and severe reactor accidents. RELAP/SCDAPSIM/MOD4.0 is the newest version of SDTP that was rewritten to FORTRAN 90/95/2000 based on RELAP or SCDAP/RELAP5. RELAP/SCDAPSIM/MOD4.0 contains advanced features such as improved numeric functions, alternative fluid properties, and an integrated graphic display. The code is also used for modeling reactors and test facilities, such as AP1000, MSRs, thermo-solar test facilities, and ITER related activities.

The advanced features in RELAP/SCDAPSIM/MOD4.0 are :

- **Advanced numeric based on of the RELAP5 governing equations**

Though RELAP5 has been validated for a wide range of flow conditions, there are still some transients are cost more time for modeling. For some transients, it is pointed out that truncation errors introduced in the linearization process can produce mass and energy errors in the non-conservative numerical approximation. Fu et al. proposed a new approach that uses a more consistent set of conservative numerical approximations to solve the non-linearized mass and energy governing equations. This new approach can help improve the overall performance of the code with improved accuracy with different user options (Fu et al., 2014).

- **3D reactor kinetics package interface (NIRK3D)**

NORTUEN and ISS have developed a standard interface for RELAP/SCDAPSIM that provides efficient coupling between thermal hydraulics and 3D reactor neutron kinetics calculation (Martínez-Quiroga et al, 2016). The database of RELAP5 heat structure and SCDAP core components and fuel rod are utilized in the interface in thermal hydraulics calculation. The power distribution is obtained in the 3D reactor kinetics package for data exchange.

- **Graphical user interfaces**

UPV and ISS developed 3D GUI capability in MOD 4.0 (Perez et al., 2015). The new displaying features such as tabular display, such as SCDAP core component temperature display, tabular display and automatically refreshed plots are available in MOD 4.0.

- **Implementation of thermophysical properties alternative fluids**

RELAP5 code was mainly developed for light water reactor transient analyses. Understandably, coolants for advanced reactors were not available in our current RELAP5 code. Initially, four working fluids other than water are implemented in the MOD 4.0, including lead-bismuth (PbBi), lead lithium eutectic (PbLi), sodium (Na) and lithium-beryllium-fluoride (FLiBe) (Trivedi et al, 2014). The thermophysical properties of the other two molten salts, FLiNaK and KF-ZrF4 are also implemented into MOD 4.0 for FHR analysis (Lin et al, 2018).

- **Uncertainty analysis package**

The BEMUSE (Best Estimate Methods - Uncertainty and Sensitivity Evaluation uses the statistical approach based on the Wilks' formula that has been developed and implemented in the MOD 4.0 by Universitat Politecnica de Catalunya (UPC) and ISS (Perez, 2011). The BEMUSE used for uncertainty analysis on LB-LOCA scenarios to evaluate and quality uncertainty bands for parameters that related reactor safety analysis.

3.2 System Analysis Module (SAM)

Under the U.S. DOE Office of Nuclear Energy's Nuclear Energy Advanced Modeling and Simulation (NEAMS) program, the System Analysis Module (SAM) is an advanced and system-level analysis tool that is being developed at Argonne National Laboratory (Hu et al, 2016a). SAM takes advantage of advances in modern software environments based on the MOOSE framework (Gaston et al, 2019), numerical methods, and physical models to build a flexible multi-physics framework for integration with other computational tools. Modeling on advanced reactors such as SFRs, LFRs, and FHRs or MSRs is one of the major targets for the code development of SAM (Hu et al, 2016a).

For SFR analysis, SAM has been coupled with other system-level codes such as SAS4A/SASSYS-1and CFD. SAM has been used for the benchmark study on EBR-II transient tests, such as an unprotected loss of forced cooling flow test and an unprotected loss of heat rejection test. The simulation results in both benchmark studies showed good agreement with experimental data, especially on the transient response of the primary loop flow in a natural circulation regime and thermal stratification in the reactor pool for a heat rejection test (Hu et al, 2016b). For reactor core modeling, an SFR 3-D full-core (hexagon lattice) model for conjugate heat transfer has been developed in SAM and verified by a test problem with seven fuel assemblies. In the 3D core model, the simulation results from SAM showed very good agreement compared with a CFD simulation (Hu et al, 2016c). With its successful validation with experimental results of SFRs, therefore, the code validation of SAM for molten salt-cooled reactors or molten salt facilities was chosen in this study.

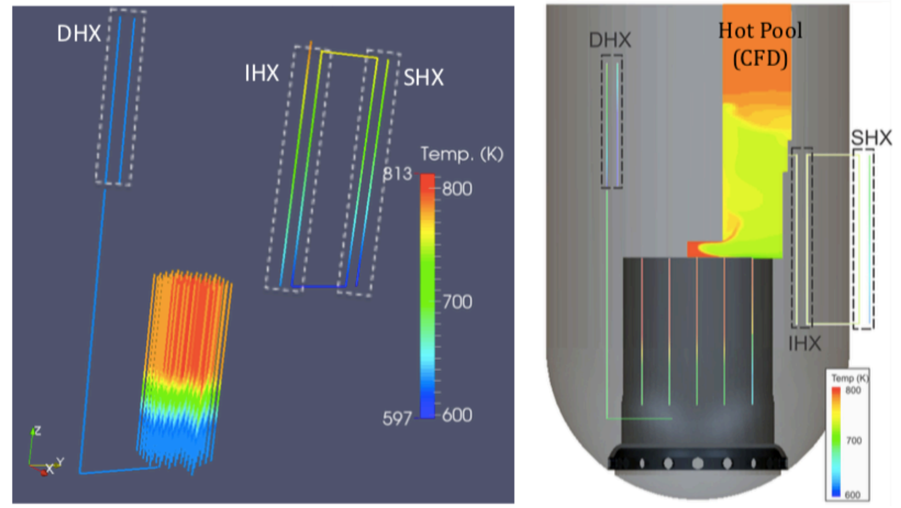

(a) SAM model with 61 core channels
(b) Coupled SAM and CFD code simulation

Figure 3-1 SAM simulation results of an SFR (Hu et al, 2016a)

SAM supports several temporal integration schemes, such as the explicit Euler, implicit

Euler (or backward Euler), backward differentiation formula-second order (BDF2), Crank Nicolson, and Runge-Kutta methods that available in MOOSE. Two time integration schemes are recommended for use in SAM, including the backward Euler and BDF2, as shown in Equations 3.1 and 3.2. For spatial integration, the trapezoidal rule is recommended for the numerical integration for first-order elements while the Gaussian quadrature rule is recommended for second-order elements in SAM. The two numerical schemes are described in Equations. 3.3 and 3.4 respectively.

Backward Euler

$$f(u^{n+1}, t^{n+1}) = \frac{u^{n+1} - u^{n}}{\Delta t} \tag{3.1}$$

BDF2

$$f(u^{n+1}, t^{n+1}) = \frac{\frac{3}{2}u^{n+1} - 2u^{n} + \frac{1}{2}u^{n-1}}{\Delta t} \tag{3.2}$$

Trapezoidal rule

$$\int_{a}^{b} f(x)dx = (b-a)\frac{[f(a) + f(b)]}{2} \tag{3.3}$$

Gaussian quadrature rule

$$\int_{-1}^{1} f(x)dx = \sum_{i=1}^{n} f(x_i)w_i \tag{3.4}$$

where x_i is the quadrature point and w_i is the weighting factor.

In addition, the Streamline-Upwind/Petrov-Galerkin (SUPG) method (Brooks et al.,1982) is also available in SAM to prevent oscillations in convection-dominated problems in the FEM. The method of Jacobian-Free Newton Krylov (JFNK) is utilized to solve non-linear equations in SAM. All the unknowns are solved simultaneously by JNFK and can avoid the errors from operator splitting. Preconditioning is required to solve equations efficiently and effectively. The Jacobian matrix is used for the preconditioning. The calculation time of SAM depends on the numbers of the nonlinear equations solved in the Newton method and linear equations by the Krylov solver (Knoll et al., 2004).

Despite the superb features in these system codes, they still lack code validation as available experimental data using molten salt as the working fluid is limited. Therefore, the following listed issues for modeling molten salt loops should be addressed to understand the gap between experiment and simulation:

- large uncertainties in liquid salt thermophysical properties, and
- lack of heat transfer and friction factor models/correlations for advanced/novel heat exchanger designs.

The versions of codes, RELAP5 and SAM, used in this study are as follows:

- RELAP5/SCDAPSIM/MOD4.0
- SAM V0.9.4

Chapter 4 Code Validation using Experimental Data with Surrogate Fluid for Molten Salt

As stated in the introduction, one of the goals of this research is to support FHR licensing through code validation. To ensure the fidelity of simulation results for FHR applications, thermal hydraulics code V&V is one of the crucial and necessary tasks. Code validation with a surrogate fluid for the molten salt was performed, since the experimental data is more available compared to molten salt data. The code validation results are summarized in this chapter. The experimental data from a natural circulation loop at Purdue University and LTDF at OSU are selected for code validation. In this study, system-level analysis codes – RELAP5 and SAM – are selected for code validation due to their flexibility in implementing the thermodynamic properties of molten salts and heat transfer correlations, advanced numerical features, and potential capability to model FHRs. In addition, the code validation results also provide code-to-code comparisons of RELAP5 and SAM. The code validation study using surrogate fluid data mainly focuses on the natural circulation flow regime, since AHTR fully relies on natural circulation/convection flows in DRACS to passively remove decay heat during accident scenarios.

4.1 Purdue University Natural Circulation Loop

The experiment of a single-phase natural circulation loop at Purdue University was performed in 1986, using water as the coolant (Hallinan et al., 1986). Two tube bundles were placed in two different vertical legs to serve as the heat source (right leg) and heat sink (left leg) of the natural circulation loop, the schematic of the facility is shown in Figure 4-1. For the heat source, the mixture of steam and cold water was fed into the source tube side of the tube bundle. In contrast, the cold water flowing in the sink tube side of the tube bundle. To allow the flow arrangement of both countercurrent-flow and parallel-flow (with respect to the flows on the shell side) in each of the tube bundles, the flow direction of the tube side to each of the tube bundles could be interchanged. The experimental data of the single-phase natural circulation loop is selected as the first code validation exercise.

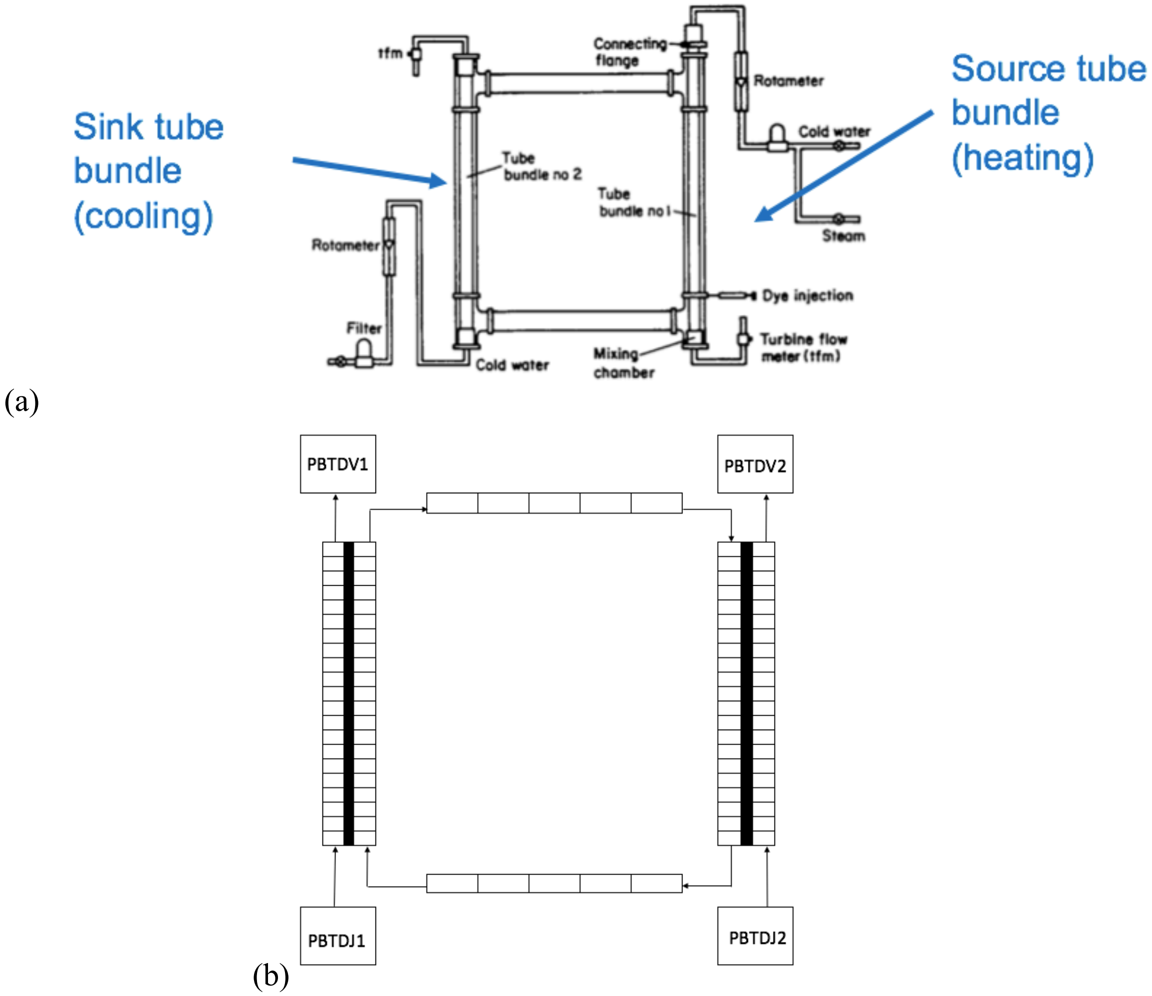

Figure 4-1. (a) Schematic and (b) nodalization of the Purdue University experimental natural circulation loop (Hallinan et al., 1986)

For code validation, two startup transients are selected, including countercurrent-flow and parallel-flow with respect to the flows on the shell side of the source tube. The flow arrangements in the sink tube for both test cases are under countercurrent flow. The boundary conditions of both startup transients are summarized in Table 4-1. For the initial condition, the water in the natural circulation loop is assumed at a constant temperature of 293 K. During the initiation of the loop startup, the hot water begins to flow into the source tubes whereas the cold-water flows through the sink tubes. In the natural circulation loop model, the heat transfer correlations developed by Hallinan et al. and Gruszczynski et al. (Hallinan et al., 1986 and Gruszczynski et al., 1983), i.e., Equations 4.1 to 4.3, are used to simulate for the source and sink tubes, where Re and Pr are Reynolds number and Prandtl number, respectively.

Table 4-1. Boundary conditions of the parallel flow and the countercurrent flow in the source tube (Hallinan et al., 1986)

Flow pattern	Source tube bundle: parallel Sink tube bundle: counter-current	Source tube bundle: counter-current Sink tube bundle: counter-current
Source tube mass flow rate	0.168 kg/s	0.07 kg/s
Sink tube mass flow rate	0.055 kg/s	0.054 kg/s
Source tube inlet temperature	322.1 K	322.1 K
Sink tube inlet temperature	287 K	287 K

Source tube bundle
Counter-current flow

$$Nu = 0.067Re^{0.8}Pr^{0.43} \tag{4.1}$$

Source tube bundle
Parallel flow

$$Nu = 0.051Re^{0.8}Pr^{0.43} \tag{4.2}$$

Sink tube bundle
Counter-current flow

$$Nu = 0.026Re^{0.93}Pr^{0.43} \tag{4.3}$$

The comparison results of the water temperatures at the source tube (shell-side) for startup scenarios in two different flow arrangements are demonstrated. Simulation results of RELAP5 and SAM also provide the function of the code-to-code comparison. The overall trends of the SAM and RELAP5 simulations of the water temperatures in the source tube under the parallel flow configuration agree well with the experimental data as shown in Figure 4-2. However, the temperature differences between the inlet and outlet in both SAM and RELAP5 simulation results are larger than experimental data during the transient of the counter-current flow case. The contribution of the larger temperature differences may due to the uncertainty of the heat transfer correlation modeling the source bundle mainly in the shell side (Figure 4-3).

The simulation results of the mass flow rates in the natural circulation loop for both the parallel and counter-current flow in the source tube bundle are provided in Figure 4-4 and Figure 4-5. However, there are no experimental data on the mass flow rates of the natural circulation loop. For both startup transients, SAM and RELAP5 simulation results show the initial peaks of the mass flow rates. The peaks in RELAP5 are damped faster than those in the SAM simulation results. The primary cause of this discrepancy is due to the different numerical schemes utilized in the two codes. The semi-implicit difference method in RELAP5 tends to have highly diffusive results, which is a typical response of lower-order methods.

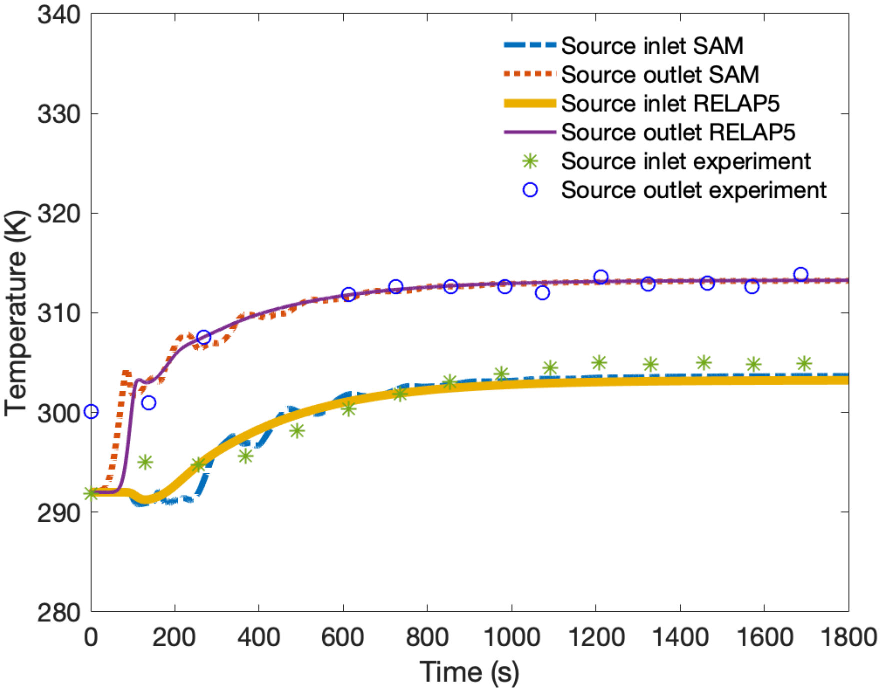

Figure 4-2. Comparisons of the source tube inlet and outlet temperatures in the loop during startup scenario (parallel flow in the source tube bundle)

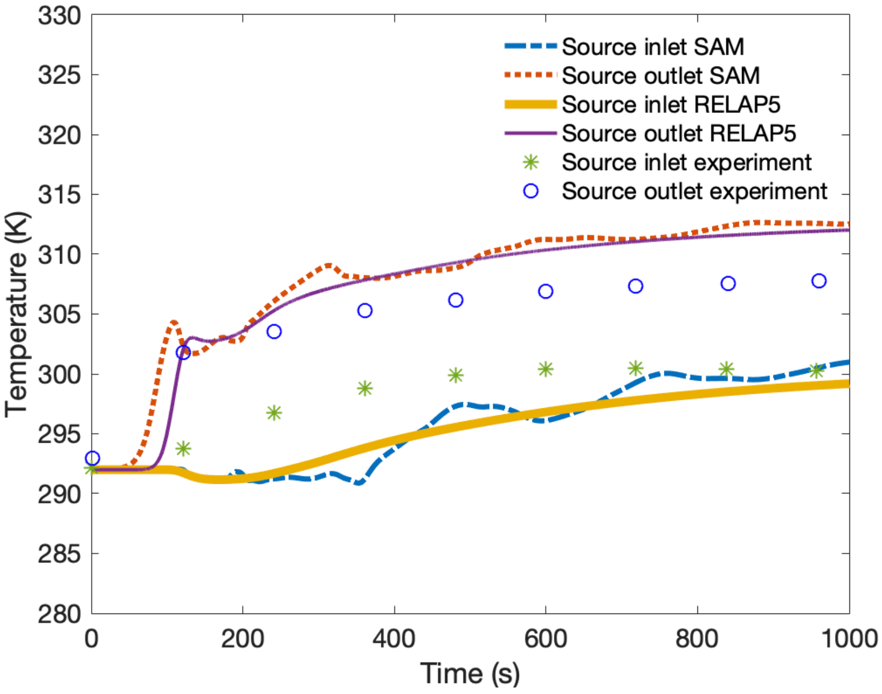

Figure 4-3. Comparisons of the source tube inlet and outlet temperatures in the loop during startup scenario (counter-current flow in the source tube bundle)

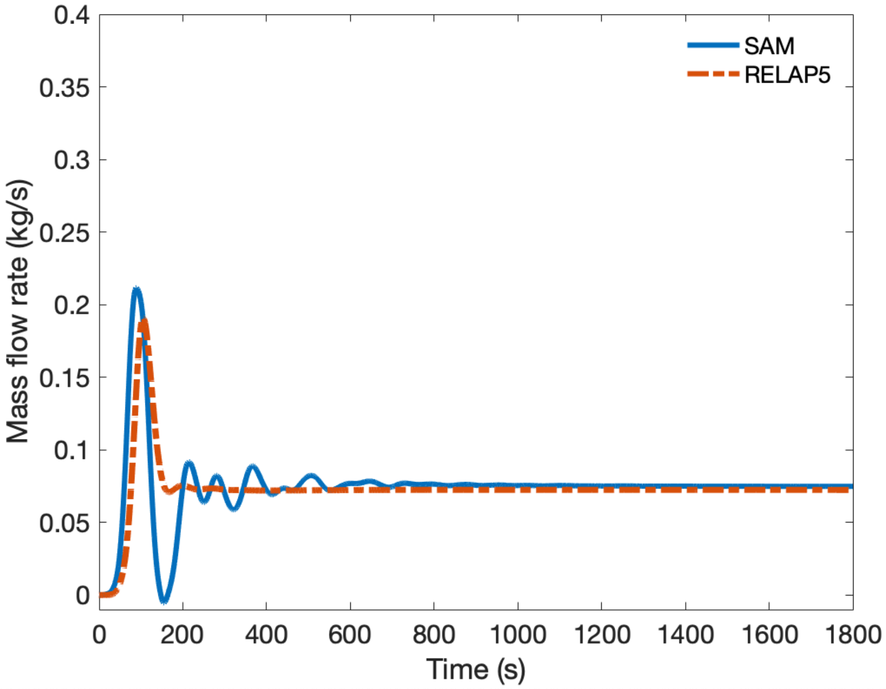

Figure 4-4. Simulation results of the mass flow rate in the natural circulation loop during the startup scenario (parallel flow in the source tube bundle)

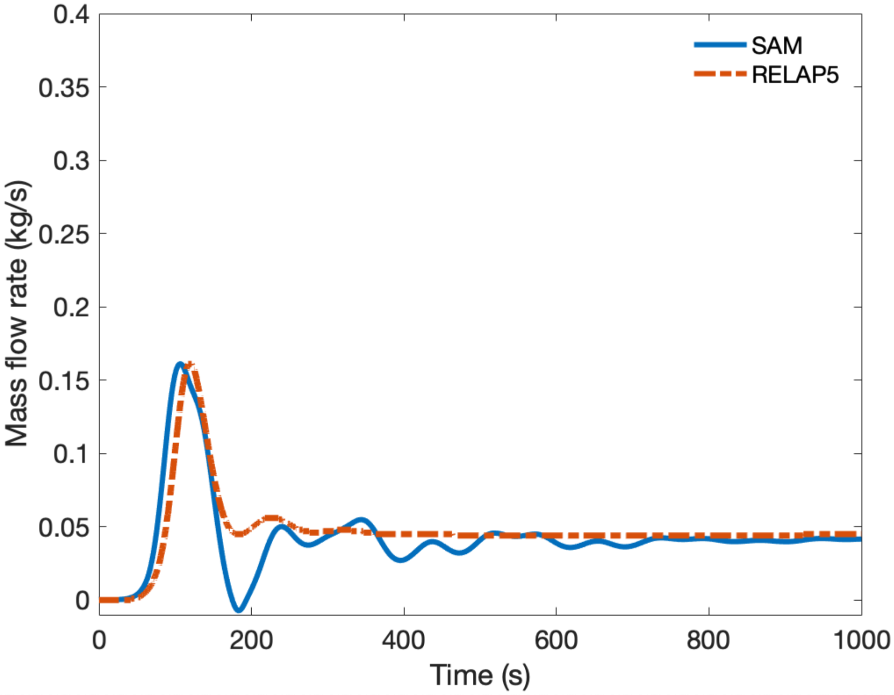

Figure 4-5. Simulation results of the mass flow rate in the natural circulation loop during startup scenario (counter-current flow in the source tube bundle)

4.2 LTDF

To investigate thermal performance of DRACS for decay heat removal by natural circulation/convection, the LTDF was therefore designed and built at the Ohio State University (Lv et al., 2015; Lv et al., 2016a and Lv et al., 2016b) as shown in Figure 4-6. Distilled water was used as a surrogate for the FLiBe in the primary loop and KF-ZrF$_4$ in the DRACS loop (i.e., the "secondary" loop in the LTDF). The primary loop was pressurized to 1 MPa to prevent potential water boiling while the DRACS loop remained near the atmospheric pressure. In the primary loop, the simulated core consists of three electric cartridge heaters, each rated nominally at 2000 W. Each heater rods have a stainless steel 304 (SS304) sheath with a 1-m heated length and were arranged in a triangular pattern. A primary pump located in the primary loop's pump branch is used to drive the water flow to both the simulated core and the DHX branch (see Figure 4-6). In the DHX branch, two ball valves provided two significantly different flow resistances in the two opposite flow directions to serve as a fluid diode simulator. A very large flow resistance in the upward flow direction while a smaller flow resistance in the downward direction. Two heat exchangers in the LTDF, namely, the DHX and NDHX, transferred heat from the simulated core to the ambient air (the ultimate heat sink in the LTDF). The heat exchanger design information is provided in Table 4-2 and Table 4-3. Equation 4.4 to Equation 4.8 are the heat transfer correlations utilized to model the heat transfer on the DHX shell side and NDHX air side. These correlations have been implemented into the RELAP5/SCDAPSIM/MOD 4.0 code and also used in the SAM model.

Table 4-2. Design parameters of the DHX in the LTDF

DHX	
Heat exchanger type	Shell-and-tube Shell side: primary loop; Tube side: DRACS loop
Tube outer diameter/thickness /length (mm)	9.525/ 1.118/ 355.6
Number of tubes	80
Pitch to diameter ratio	1.208
Shell inner diameter (m)	0.127
Baffles number and baffle cut	4 and 25.8%

Table 4-3. Design parameters of the NDHX in the LTDF

NDHX	
Heat exchanger type	Finned tube bundle Tube side: DRACS loop; Finned side: Air loop
Tube outer diameter (mm)	15.875
Tube thickness (mm)	0.889
Number of tubes	52 (in 2 rows with 26 per row)
Pitch to diameter ratio	2.4
Tube length (m)	0.9906
Fin height/ thickness/spacing (mm)	12.065/0.254/2.54
Material	Copper tube + Aluminum fin

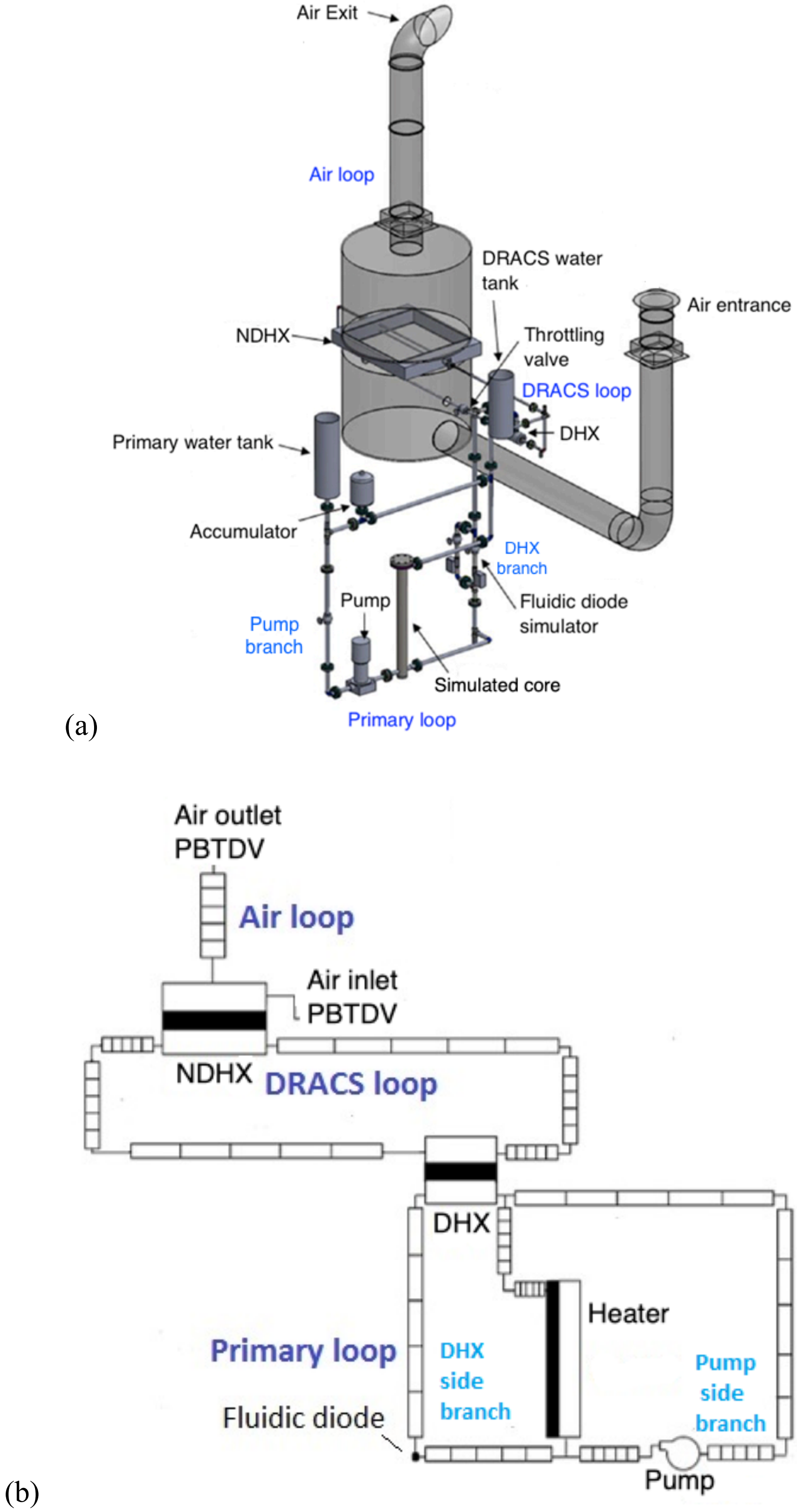

Figure 4-6. (a) Schematic and (b) nodalization of the LTDF (Lv et al., 2016a)

DHX shell side (Zkauskas, 1987):

$$Nu = 1.04Re^{0.4}Pr^{0.36}(Pr/Pr_w)^{0.25} \qquad 1 \le Re < 500 \tag{4.4}$$

$$Nu = 0.71Re^{0.5}Pr^{0.36}(Pr/Pr_w)^{0.25} \qquad 500 \le Re < 1{,}000 \tag{4.5}$$

$$Nu = 0.35Re^{0.6}Pr^{0.36}\left(\frac{X_t^*}{X_l^*}\right)^{0.2}(Pr/Pr_w)^{0.25} \qquad 1{,}000 \le Re < 2 \times 10^5 \tag{4.6}$$

$$Nu = 0.031Re^{0.8}Pr^{0.36}\left(\frac{X_t^*}{X_l^*}\right)^{0.2}(Pr/Pr_w)^{0.25} \qquad Re \ge 2 \times 10^5 \tag{4.7}$$

NDHX finned tube (air) side (Briggs and Young, 1963):

$$Nu = 0.134\left(\frac{\rho v_{max} d_o}{\mu}\right)^{0.68} Pr^{0.33}\left(\frac{e_f}{S}\right)^{0.18}\left(\frac{Y}{S}\right)^{-0.14} \qquad 1 \le Re < 10^6 \tag{4.8}$$

X_t^*: relative transverse tube spacing;

X_l^*: relative longitudinal tube spacing;

S: fin spacing;

e_f: fin height;

Y: fin thickness;

d_o: tube outer diameter;

v_{max}: maximum air velocity across the finned tubes;

Re: Reynolds number;

Pr: Prandtl number based on the fluid properties specified at the fluid average temperature;

Pr_w: Prandtl number based on the fluid properties specified at the wall temperature

In the RELAP5 LTDF model, the volume numbers for the simulated core, DHX, and NDHX and piping are 25, 50, 50 and 4 respectively. The mesh independence results can be found in (Lin, 2016). The mesh independence study for SAM model is listed in Table 4-4. In the SAM LTDF model, the volume numbers for the simulated core, DHX, and NDHX and piping are 10, 20, 20 and 4 respectively. For code validation analysis on the small-scale and high-temperature test facility, the heat loss should be considered. The heat loss model calculates the heat deposit in the structure wall and transfers to the room environment. The model contains pipe walls, structure walls, flanges and insulation material which is shown in Figure 4-7. The structure materials in LTDF are SS304 wrapped with 2-inch-thick fiberglass and a constant temperature is given at room temperature 25 °C. Equation 4.9 (Churchill and Chu.,1975) which is usually used for natural convection over vertical plates are utilized to model the heat transfer from the insulation outer surface to the environment. Based on the heat balance analysis on the experimental data, the large measurement uncertainties in the flow meters make the heat balance results hard to quantify (Lv et al. 2015). From the simulation results, the total heat loss in the LTDF is about 7% based on a total power of 2 kW provided in the core when the system reaches a steady state.

Table 4-4. Grid independence study for SAM LTDF model

Item	Volume number	Core inlet temperature (°C)
LTDF Core	5	335.6
	10	335.6
	20	335.6
LTDF DHX	Volume number	DHX tube side outlet temperature (°C)
	5	327.9
	10	324.4
	20	324.4
	40	324.4
LTDF NDHX	Volume number	DHX tube side inlet temperature (°C)
	5	306.1
	10	305.8
	20	305.8
	40	305.8

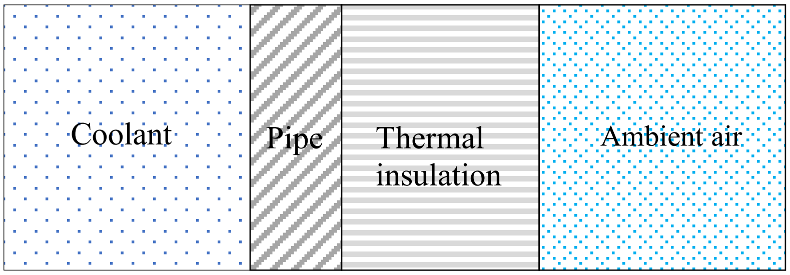

Figure 4-7. Wall structure and thermal insulation in the heat loss model.

Natural convection (Churchill and Chu.,1975):

$$\mathrm{Nu} = \left\{0.825 + \frac{0.387\mathrm{Ra}^{1/6}}{[1 + (0.492/\mathrm{Pr})^{9/16}]^{8/27}}\right\}^2 \tag{4.9}$$

Ra: Rayleigh number

In the LTDF, T-type thermocouples, ultrasonic flow meters, and a thermal mass flow meter are used to measure the fluid temperatures, water flow rates (for both the primary and DRACS loops), and air flow rate, respectively. The measurement uncertainties (including both the systematic uncertainties associated with the instruments and the random uncertainties associated with the measured data) of the fluid temperatures, primary water, DRACS water, and air mass flow rates are estimated as ±0.5 ºC, ±0.0089 kg/s, ± 0.0033 kg/s, and ± 0.01 kg/s respectively, with a 95% confidence level (Lv et al., 2016a and 2016b).

The simulation results compared to the experiments for three transient scenarios, including reactor coolant pump trip with a constant simulated reactor power, reactor coolant pump trip at decay power and DRACS startup scenarios from the unheated state, as shown in Figure 4-8 to Figure 4-24.

4.2.1 LTDF Pump Trip with Constant Power

The pump trip scenario in LTDF is chosen for the validation benchmarks, in which the DRACS performance under loss of forced circulation (LOFC) can be demonstrated through this transient. Prior to initiation of the pump trip, the LTDF was heated at 2,000 W power from heaters in the simulated core and about 700 W pump heat to the system and the facility reached a steady state to simulate the DRACS conditions under reactor normal operation. From the experimental data, 21.46 ^{o}C the air inlet temperature to the NDHX air side is used as one of the boundary conditions as measured in the experiment. The primary pump provided a total mass flow rate of 1.73 kg/s to the primary loop.

The primary pump was tripped to initiate the transient while the heating power in the simulated core still remained at 2,000 W. The simulation results of both RELAP5 and SAM are provided for code-to-code comparison. Figure 4-8 and Figure 4-14 show the primary flow losing the driving force from the primary coolant pump and establishing natural circulation flow after the pump trip. The primary flow reverses in the DHX branch due to (a) large flow resistance of upward flow in the simulated fluidic diode while smaller flow resistance in the downward flow direction and (b) buoyancy force starts to drive the primary flow with the simulated core as the heat source and DHX as the heat sink. In Figure 4-8, the DHX shell side changes from unheated water to heated water by the core temperature, therefore, the temperatures increase when flow reverses. The temperature increase in the DHX shell side also results in temperature peaks in Figure 4-10 and Figure 4-12. In Figure 4-9, both RELAP5 and SAM underestimates the temperature peaks for 2 to 3 ^{o}C in the DHX shell-side. The abrupt temperature decreases due to flow reversal in Figure 4-9 is clearly captured by SAM. However, simulation results in RELAP5 show a smoother peak compared to experimental data. A similar effect can also be observed in Figure 4-11 that SAM gives good agreement in the temperature decrease with experimental data during initiation of pump tripping. In 25,000 s, the computed water temperature differences between the inlet and outlet on the DHX tube-side (DRACS loop) is about 4 °C smaller than those in the experimental data (See Figure 4-10). The uncertainties in the heat transfer correlations used in the DHX and NDHX and discrepancy of the mass of heat structures and flow resistance can also contribute to the difference between the simulation results and experimental data.

The overall simulation results of both codes agree well with each other, moreover, both simulation results show reasonably good agreement between the experimental data. Both the experimental and simulation results indicate that although the temperature responses of the entire DRACS system can be affected by the daily variation of the ambient air temperature, the overall DRACS thermal performance can still be clearly observed and its functionality be confirmed. Figure 4-13 and Figure 4-14 show the good agreement of mass flow rates in LTDF between experiments and simulation results. However, in Figure 4-13, the air mass flow rate remains unstable throughout the duration. This is primarily because the air inlet chimney points to a fix direction and thus is heavily affected by the natural wind (direction and wind speed). Overall, both experiment and simulation results demonstrate that the DRACS can still remove the heat from the simulated core after losing the driving force from the primary coolant pump.

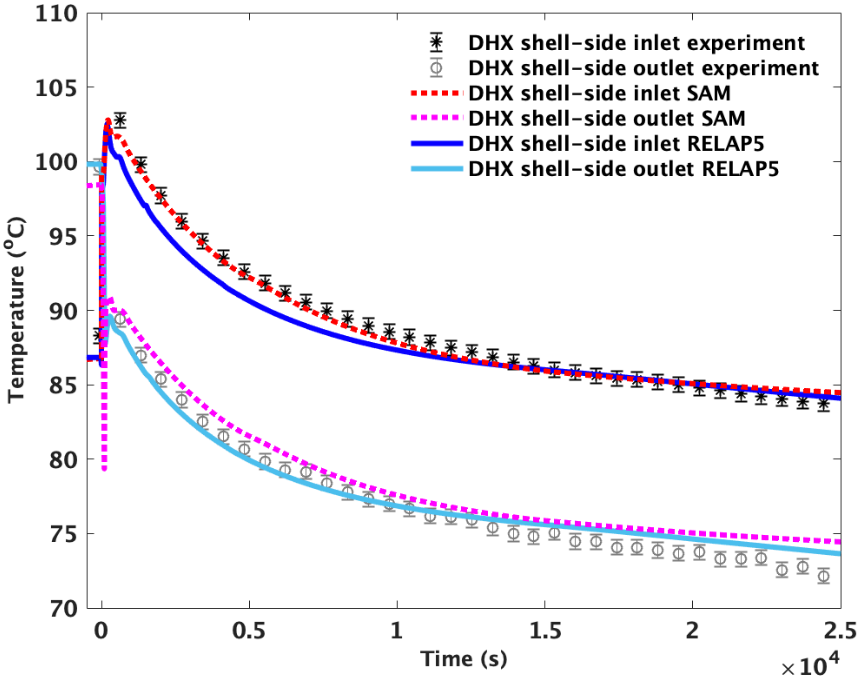

Figure 4-8. RELAP5 and SAM simulation results compared with experiments of DHX shell side temperatures during reactor coolant pump trip scenario (constant power)

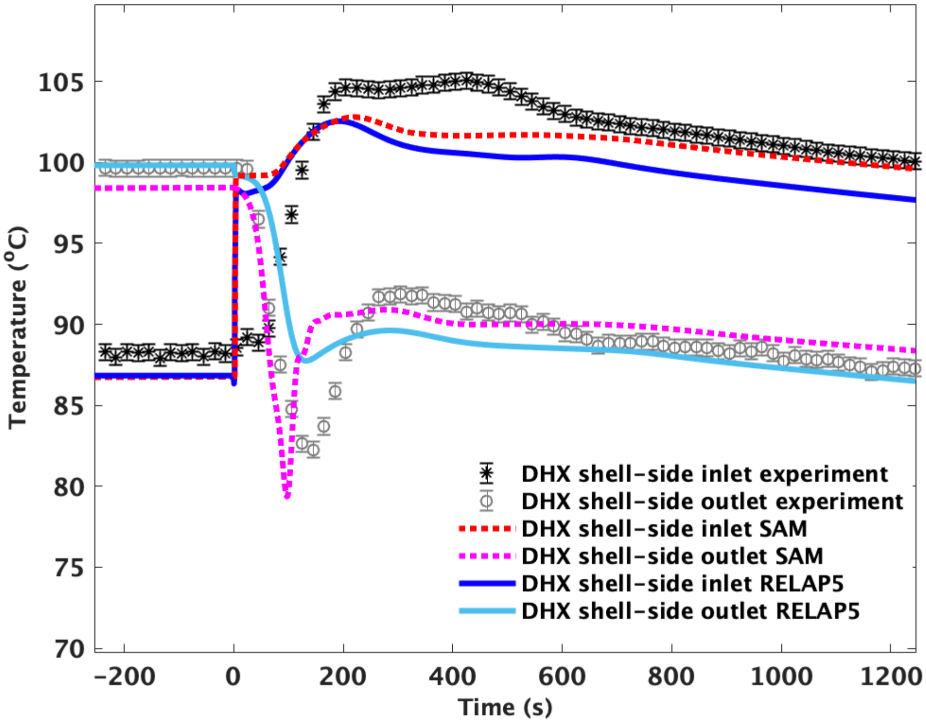

Figure 4-9. The smaller time frame of Figure 4-8

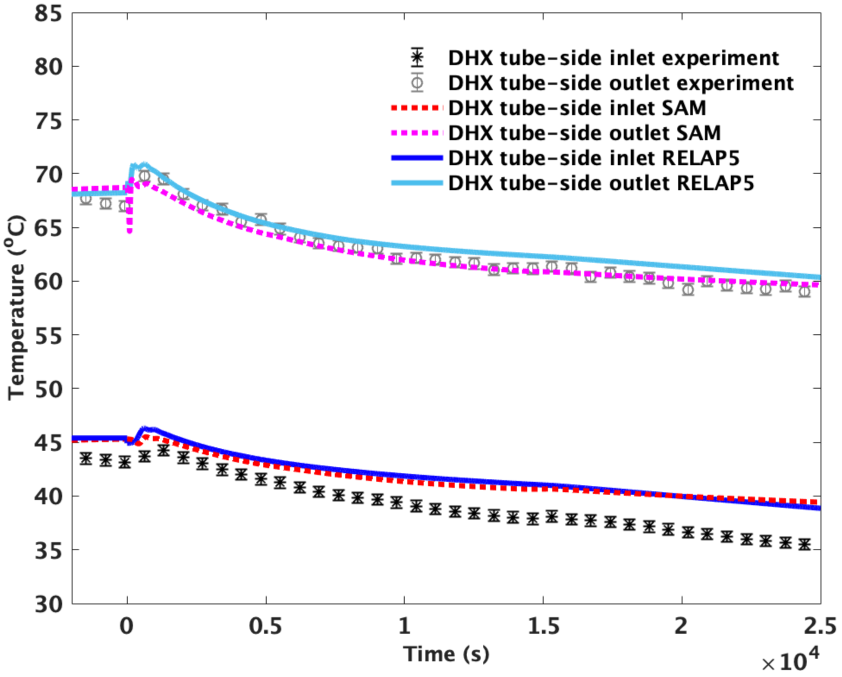

Figure 4-10. RELAP5 and SAM simulation results compared with experiments of DHX tube side temperatures during reactor coolant pump trip scenario (constant power)

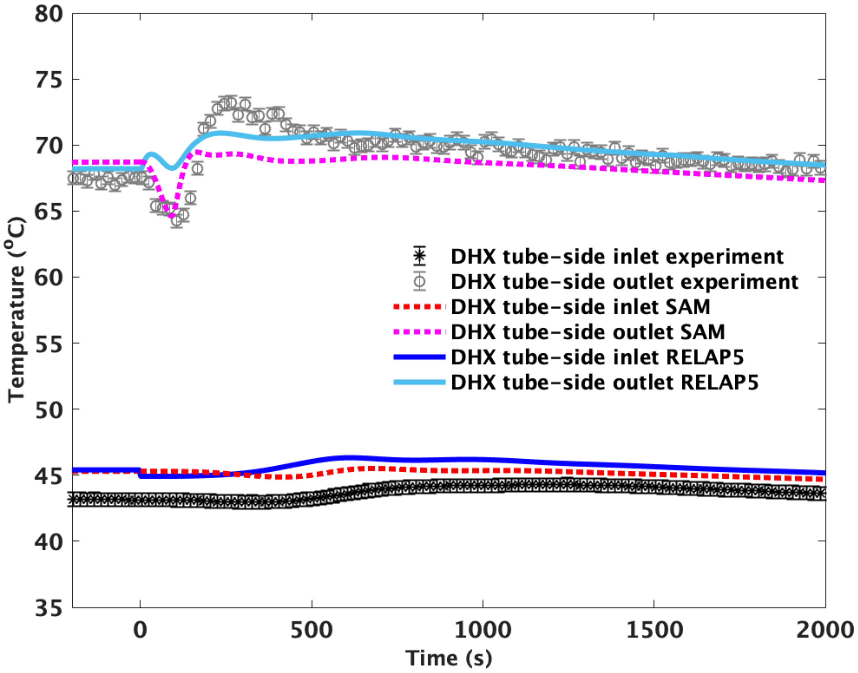

Figure 4-11. The smaller time frame of Figure 4-10

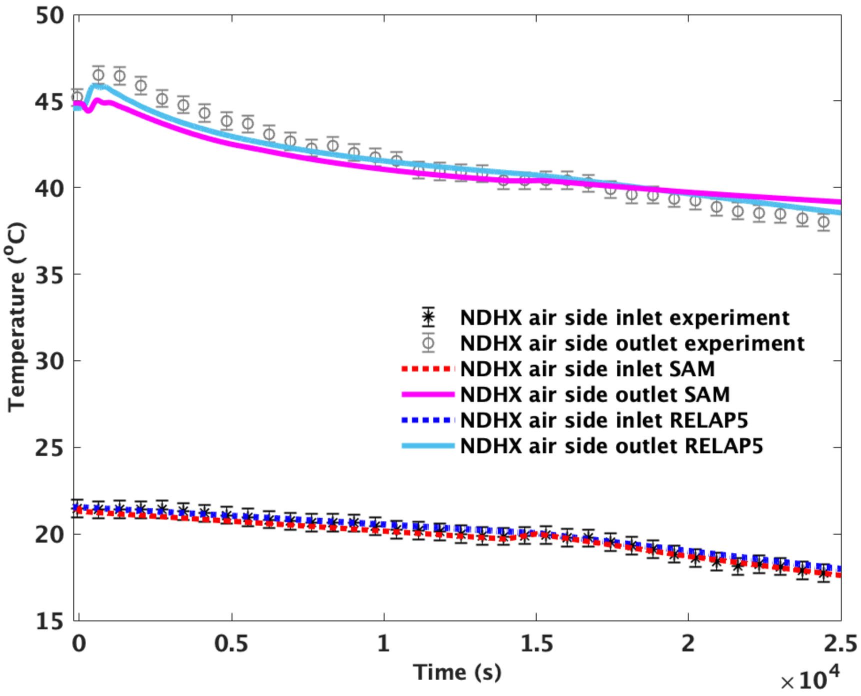

Figure 4-12. RELAP5 and SAM simulation results compared with experiments of NDHX air side temperatures during reactor coolant pump trip scenario (constant power)

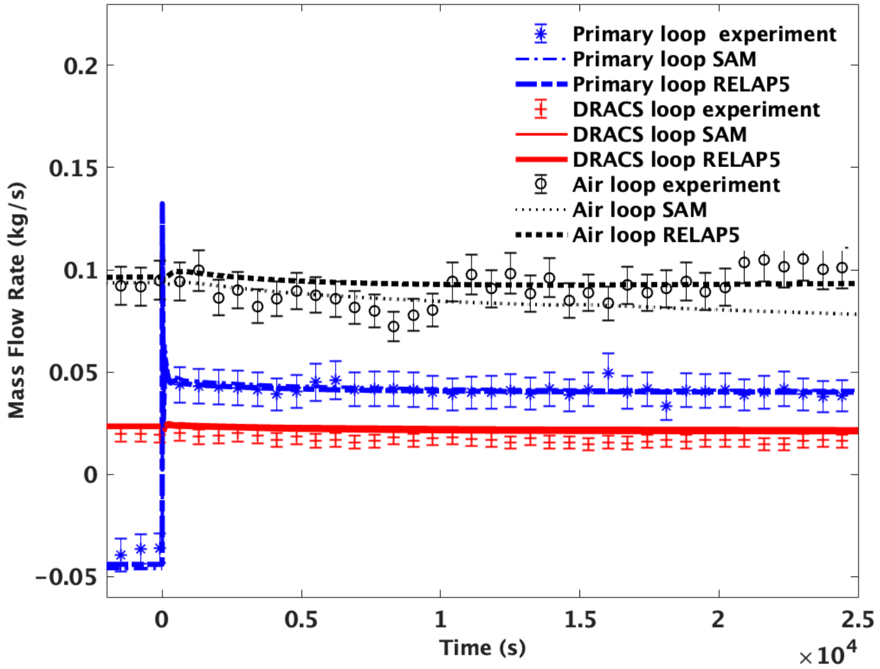

Figure 4-13. RELAP5 and SAM simulation results compared with experiments of mass flow rates during reactor coolant pump trip scenario (constant power)

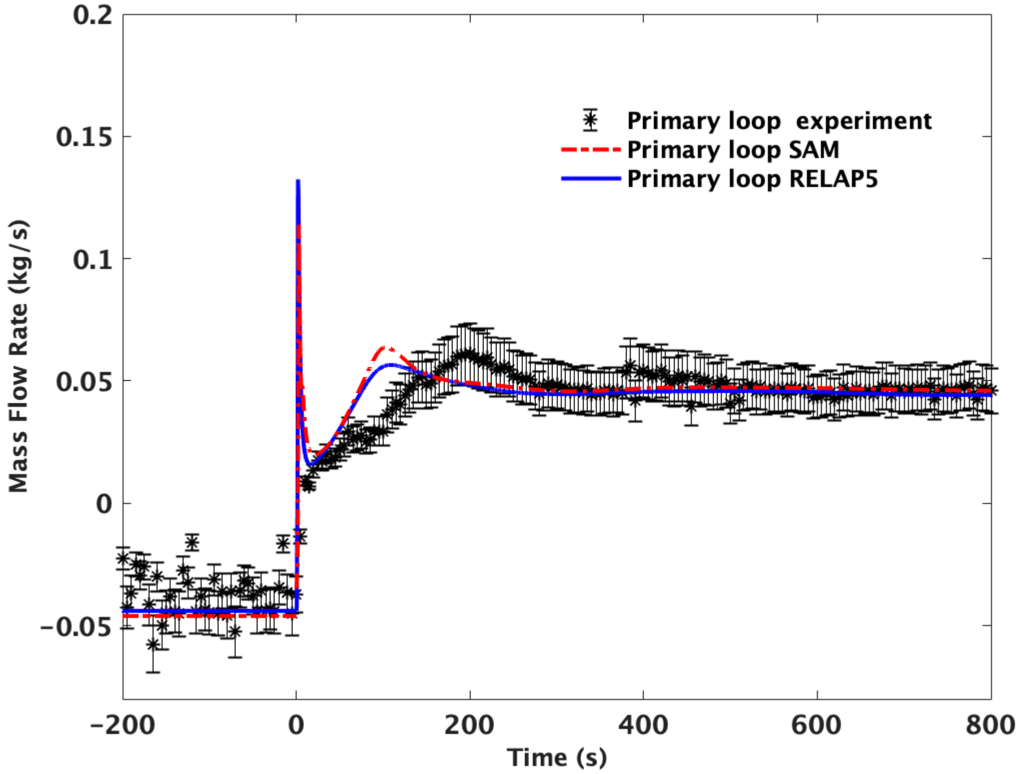

Figure 4-14. The smaller time frame of the primary mass flow rate in Figure 4-13

4.2.2 LTDF Pump Trip with Decay Power

Code validation of the second pump trip in LTDF with a decay power curve applied as a function of the reactor cooling time is performed. In Figure 4-15, the decay power curve is adopted from LWRs' decay curve (El-Wakil, 1971). However, because of the maximum power limitation of the three electric heaters in the LTDF, a constant heating power of approximately 4,983 W is therefore provided before 1,564 s. The total amount of decay energy deposited in the DRACS primary loop following the modified decay curve is the same as the original LWR decay curve from 0 to 1,564s. The decay power applied by the heaters in the LTDF matches the LWR decay curve after 1,564 s.

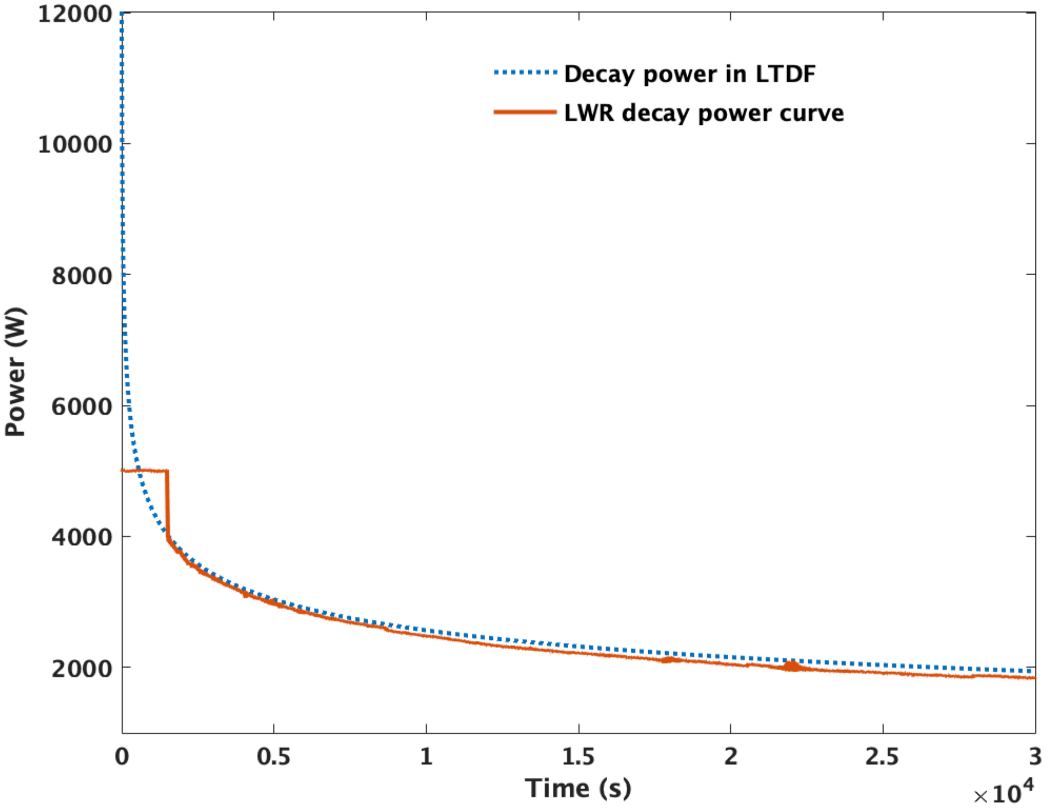

Figure 4-15. Adopted decay power curve in the LTDF for the second pump trip scenario

The water temperatures of the DHX shell side and mass flow rates of pump branch and DHX branch in the primary loop are shown in Figure 4-16 and Figure 4-17 in a smaller time frame. In Figure 4-16, the reverse flow in the DHX branch can also be captured by the water temperature that DHX shell side inlet temperature (close to the core outlet) switch from lower to a higher temperature. In Figure 4-17, the RELAP5 simulation also gives satisfactory agreement with the experimental data that demonstrated the flow reversal in the mass flow rate of the DHX branch. The simulation results of the second pump trip scenario from Figure 4-18 to Figure 4-20 has strengthened the RELAP5 code can provide sufficient modeling capability on heat transfer modeling and forced flow and natural circulation flow.

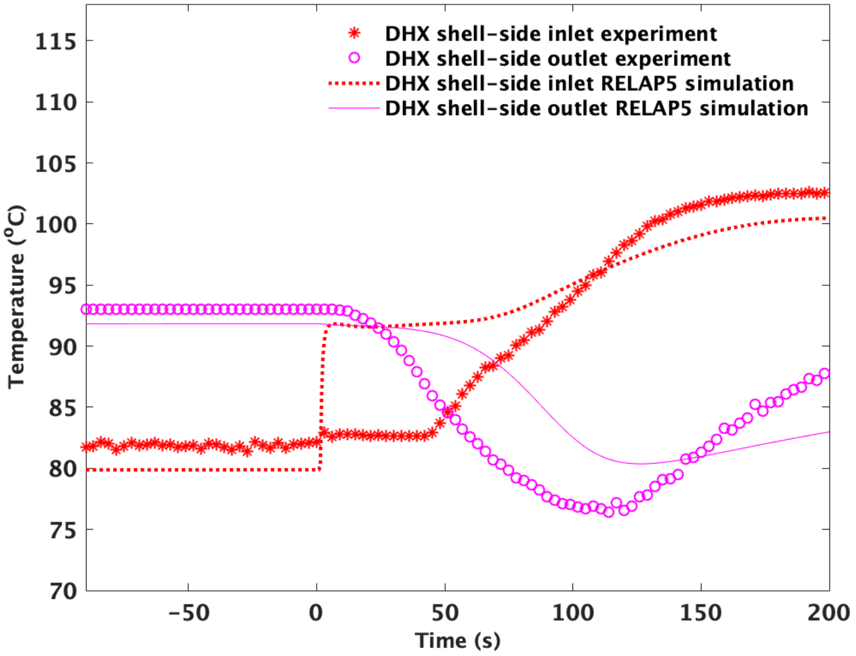

Figure 4-16. RELAP5 simulation results compared with the experiments of DHX shell side temperatures during LTDF pump trip scenario (reactor at decay power)

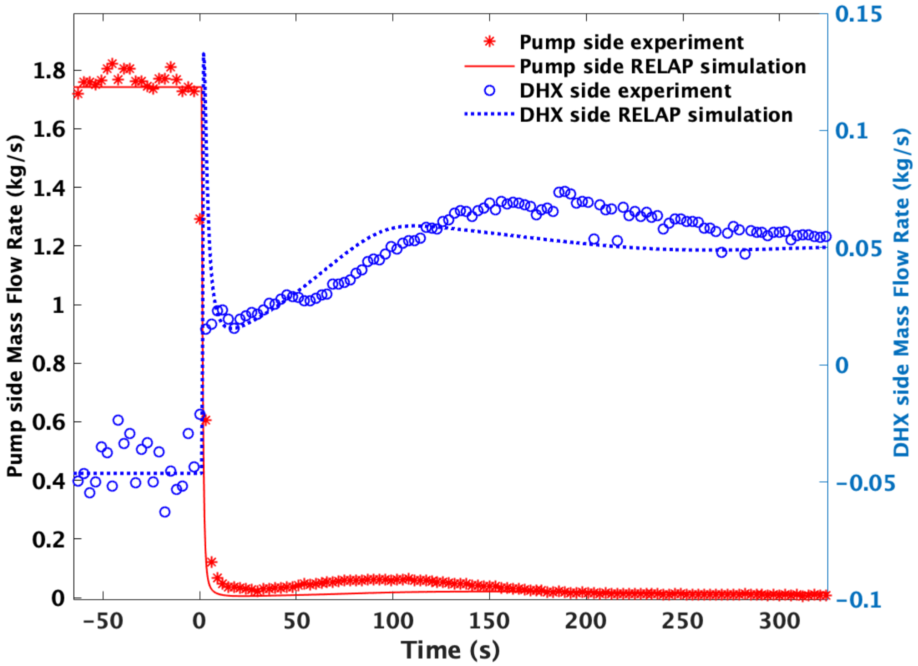

Figure 4-17. RELAP5 simulation results compared with the experiments of mass flow rates during LTDF pump trip scenario (reactor at decay power)

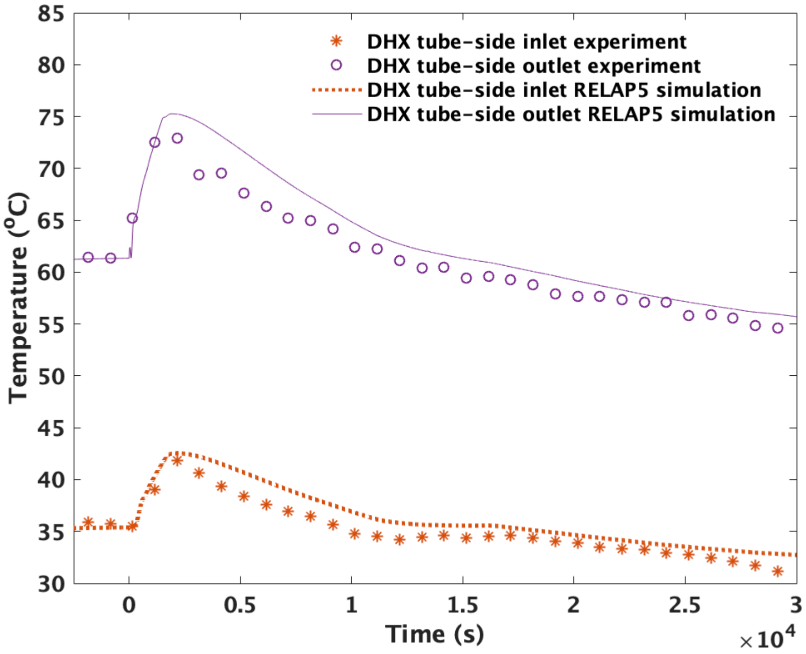

Figure 4-18. RELAP5 simulation results compared with the experiments of DHX tube side temperatures during LTDF pump trip scenario (reactor at decay power)

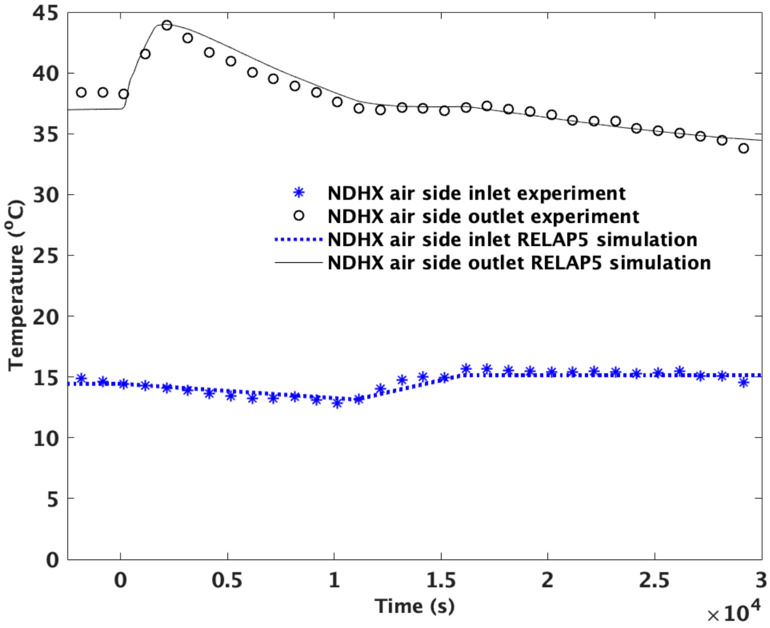

Figure 4-19. RELAP5 simulation results compared with the experiments of NDHX air side temperatures during LTDF pump trip scenario (reactor at decay power)

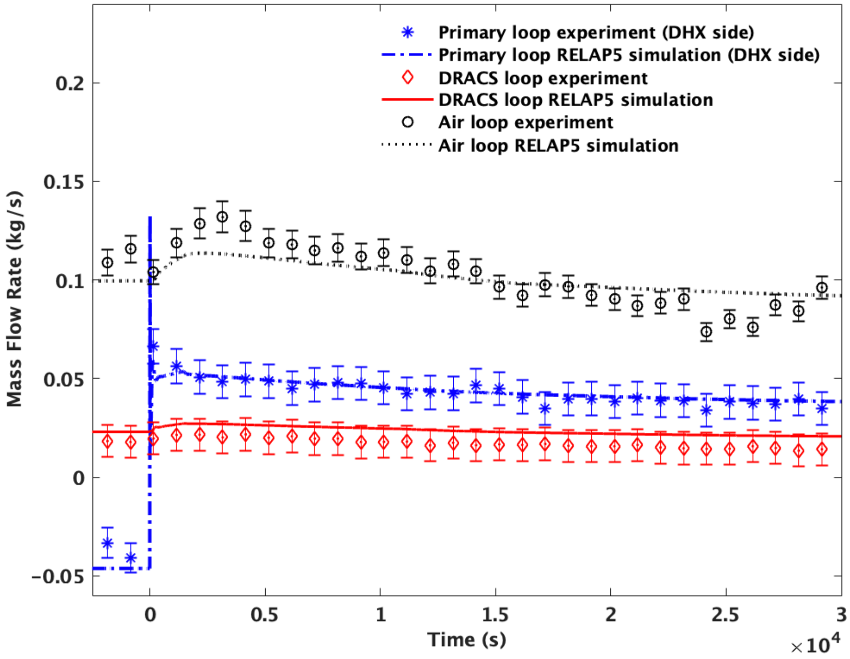

Figure 4-20. RELAP5 simulation results compared with the experiments of three mass flow rates during LTDF pump trip scenario (reactor at decay power)

4.2.3 LTDF Startup Scenario

The objective of the startup scenario in the LTDF is to investigate the establishment of natural circulation/convection after the system heats up. For the initial condition, the three loops are all stagnant and are at room temperature initially. When the DRACS startup scenario is initiated, a constant heating power of 2000 W is provided to the system by the simulated core. Figure 4-21 demonstrates natural circulation flow in the three loops are gradually established during the transient. The temperature transient responses from both the experiment and simulation indicate that the system reaches a quasi-steady state at approximately 16,000 s from the event initiation when the temperature difference between the inlet and outlet of DHX and NDHX are close to a constant. At 30,000 s, the water inlet and outlet temperature differences on the DHX shell side obtained from the RELAP5 simulation are approximately 2 °C smaller than those in the experimental data. Compared to the experimental results, the RELAP5 simulation over-predicts the DHX tube-side inlet temperatures during water heat up with maximum temperature 3 °C at 9,000s. Overall, the fluid temperature responses in the three loops from the RELAP5 simulation results exhibit reasonably good agreement with the experimental data during the DRACS startup transient.

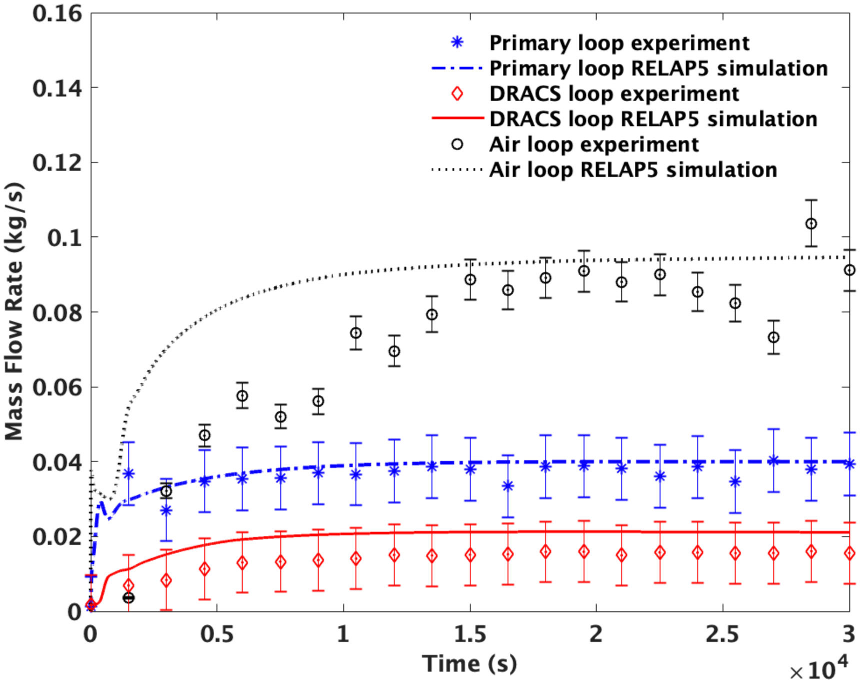

Figure 4-21. RELAP5 simulation results compared with experiments of three mass flow rates during DRACS startup scenario

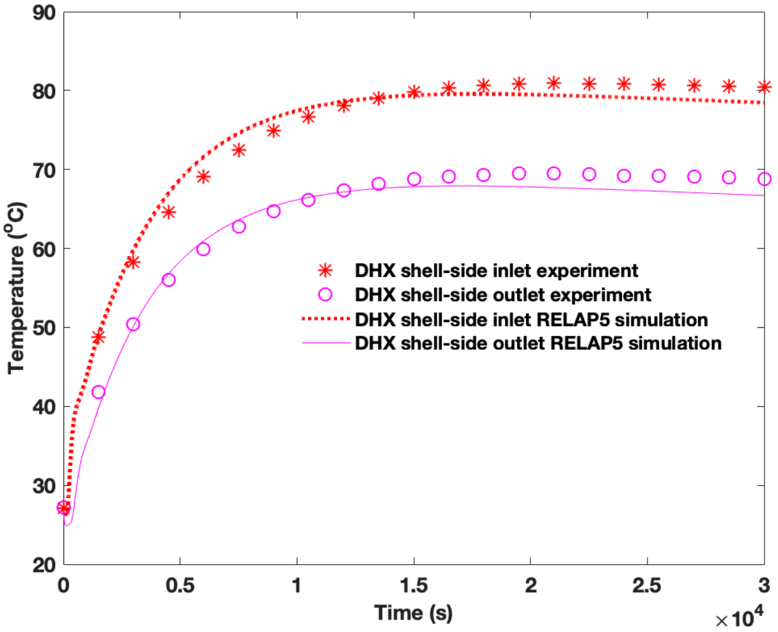

Figure 4-22. RELAP5 simulation results compared with experiments of DHX shell side temperatures during DRACS startup scenario

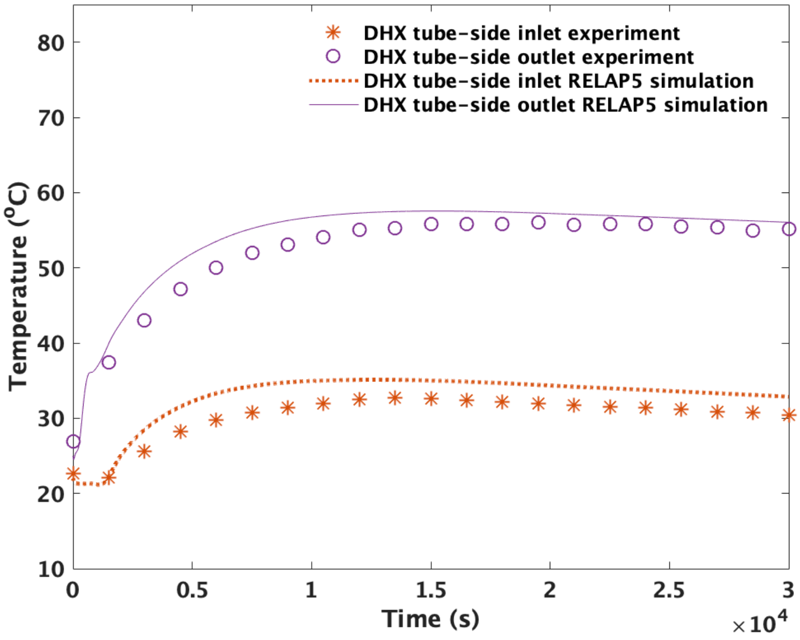

Figure 4-23. RELAP5 simulation results compared with experiments of DHX tube side temperatures during DRACS startup scenario

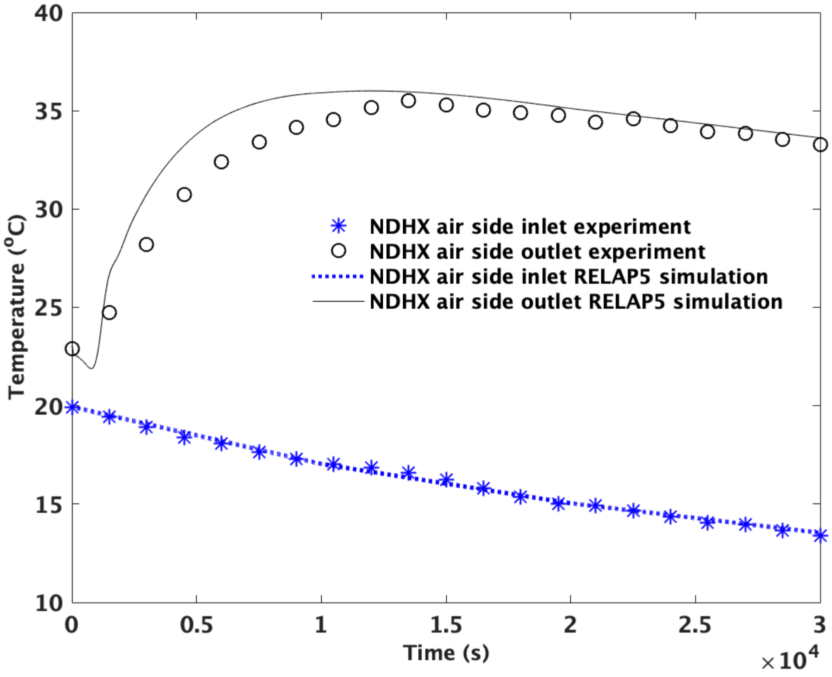

Figure 4-24. RELAP5 simulation results compared with experiments of NDHX air side temperatures during DRACS startup scenario

Chapter 5 Code Validation using Molten Salt Experimental Data

5.1 FLiBe Natural Circulation Loop Test Facility

In FLiBe natural circulation loop, there are four heaters (two heaters locate in the bottom pipe and two heaters are in the riser pipe) and an air cooler located in the top pipe, as shown in Figure 5-1(a). The bottom and the top pipe are designed with 20° and 10° inclined angles, respectively, to improve the natural circulation flow. The piping of the FLiBe salt loop is made of 316 L (25.4 mm outer diameter and 3 mm tube thickness). Two air cooling pipes (6 cm inner diameter) located in the top pipe and the downcomer, respectively, with an air blower to control the air flow rate. In current tests of the FLiBe natural circulation loop, the air flow in the downcomer is blocked hence the stagnant air is served as an insulation layer to the downcomer salt pipe. Ten tests with different heating powers and cooling rates are performed to investigate their steady states of the FLiBe natural circulation loop.

5.2 SAM FLiBe Natural Circulation Loop Model

A FLiBe natural circulation loop is built for SAM code validation, as shown in Figure 5-1(b). The locations of thermal couples (TCs) are provided. For the nodalization of the SAM FLiBe natural circulation loop model, there are 40 volumes in each heater and the top air cooler and 4 volumes in each piping. Time depend volumes (PBTDV) can be used to model the inlet and outlet of air. Table 5-1 summarizes the air inlet temperatures and air inlet velocities measured in the experimental data, which are applied as the boundary conditions. For code validation on the high temperature test facility, the heat loss model is also included in the FLiBe natural circulation loop analysis to calculate heat transfer from molten salt through pipes and insulation to the ambient air. In addition to thermal convection, thermal radiation is also considered in the heat loss model. For convection, the heat transfer coefficients are calculated from Equation 4.9. A 3-cm-thick of insulation is used to wrap every piping and components. The insulation surface emissivity is 0.7 in the SAM model. The ambient temperature for both convection and thermal radiation is set at 18 °C (291 K). The code validation study using UW FLiBe natural circulation loop data involves uncertainty analysis. Therefore, only SAM is used for this code validation due to the flexibility in changing coolant properties in the input file.

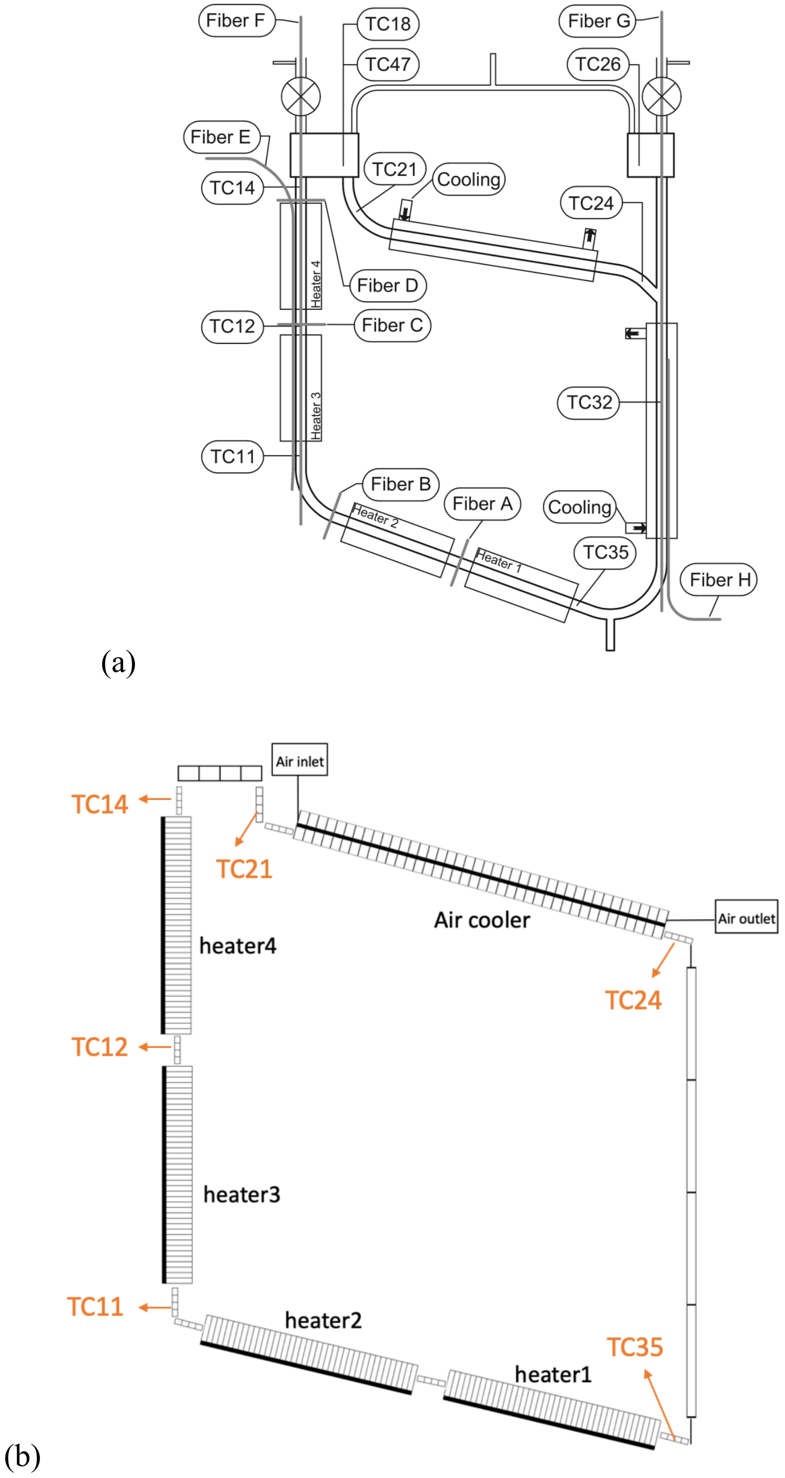

Figure 5-1. (a) Schematic and (b) nadolization of FLiBe natural circulation loop

Table 5-1. Boundary conditions for six tests (Britsch et al., 2019)

	Power (W)	Air inlet velocity (m/s)	Air inlet temperature (°C)	Air outlet temperature (°C)
Test 4	5,192	6.49 ± 0.08	26.7 ± 3.1	193.5 ± 3.2
Test 6	5,884	6.49 ± 0.14	27 ± 3.1	226.2 ± 3.6
Test 7	5,884	9.19 ± 0.11	29.4 ± 3.1	158.0 ± 3.3
Test 8	6,576	6.52 ± 0.08	27.3 ± 3.1	240.5 ± 3.4
Test 9	6,576	9.17 ± 0.08	29.3 ± 3.1	183.9 ± 3.2
Test 10	6,576	12.8 ± 0.08	33.7 ± 3.1	144.1 ± 3.2

For the code validation, the experimental data of Tests 4, 6, 7, 8, 9 and 10 from are selected with the different heating powers and different air cooling rates, their boundary conditions are listed in Table 5-1. The friction coefficient (f) in the developing region is applied in the FLiBe natural circulation loop model (Langharr et al., 1942). For temperature measurement, two fiber-optic sensors (Fiber F and Fiber G in Figure 5-1(a)) are located in the center along two vertical pipes in the axial direction. Thermocouples and additional fiber-optic sensors are inserted in the pipe in a radial direction.

The form loss coefficients of fiber-optic sensors and thermocouples are obtained by STAR-CCM+ modeling. Thermocouples with outer diameter 1.6 mm (1/16 inch) are inserted in a radial direction to measure the salt temperature at pipe (25.4 mm inner diameter) center, the insertion length of each thermocouple is half of the pipe diameter. The pipe model with a thermocouple is built in STAR-CCM+ as shown in Figure 5-2, the length of the pipe in the model is 10 cm. Based on the mesh independence study in Table 5-2 with pressure drops across the pipes, mesh 3 is selected as the final model and the mesh layout of mesh 3 is shown in Figure 5-3. Similarly, the flow obstructions of optic-fiber sensors are also investigated using STAR-CCM+. For optic-fiber sensors (outer diameter 800 μm) inserted in a radial direction, the insertion length is one pipe diameter as shown in Figure 5-4. The pipe length of the model is also 10 cm. Figure 5-6 shows the optic-fiber sensor arranged in the axial direction, with 1.4 m pipe length. To simplify the model, the pipe is placed horizontally so gravity is not considered. The mesh independence study optic-fiber sensor in two directions are listed in Table 5-3 and Table 5-4, respectively. Mesh 2 in both models are selected based on the mesh independence study. With the calculated pressure drop across the pipe, the form loss coefficients (K) can be found in Equation 5.1. The inlet boundary conditions of the three models in STAR-CCM+ are the same, in which the density and viscosity of FLiBe are 1938 kg/m^3 and 0.0055 Pa-s at 700 °C and the inlet velocity is 5.4 cm. The form loss coefficients of these instrument obstructions and flow direction changes used in the model are listed in Table 5-5.

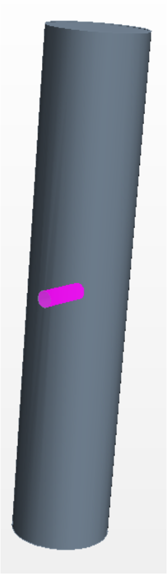

Figure 5-2. Geometry of pipe with a thermocouple

Table 5-2. Mesh independence study of pressure drop across pipe with a thermocouple

Mesh	Base size (cm)	Cell number	Pressure drop between pipe inlet and outlet (Pa)	Mesher: Polyhedral mesher, prism layer mesher, surface remesher Prism layer: 4 Prism layer stretching: 1.5 Prism layer thickness: 33 %
1	0.1	72,530	5.1	
2	0.08	125,521	5.0	
3	0.05	394,296	4.8	
4	0.04	604,142	4.8	

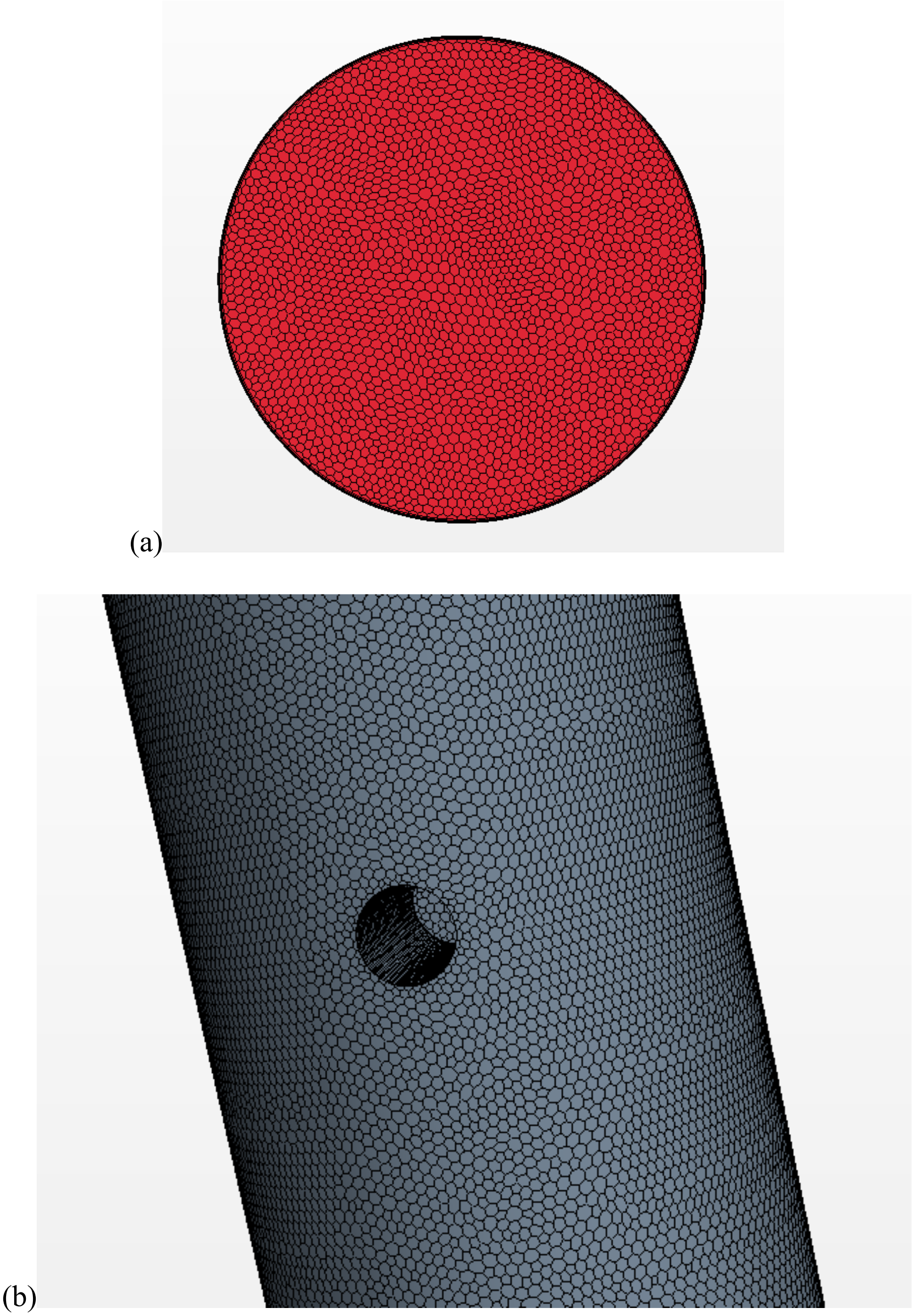

Figure 5-3. Mesh of pipe with a thermocouple model (a) cross-section and (b) side view

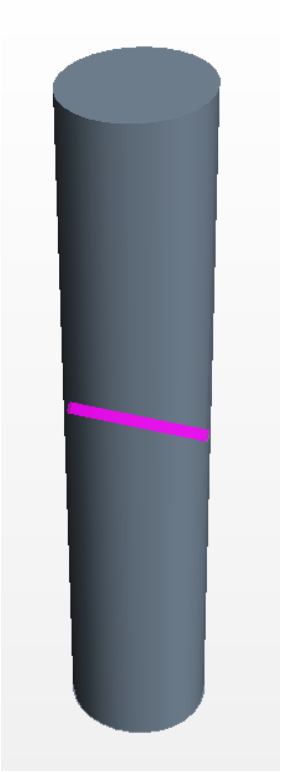

Figure 5-4. Geometry of pipe with an optic-fiber sensor (radial direction)

Table 5-3. Mesh independence study of pressure drop across the pipe with an optic-fiber sensor (radial direction)

Mesh	Base size (cm)	Cell number	Pressure drop between pipe inlet and outlet (Pa)	Mesher: Polyhedral mesher, prism layer mesher, surface remesher Prism layer: 4 Prism layer stretching: 1.5 Prism layer thickness: 33 %
1	0.1	69,562	5.5	
2	0.05	474,273	5.2	
3	0.03	741,808	5.2	

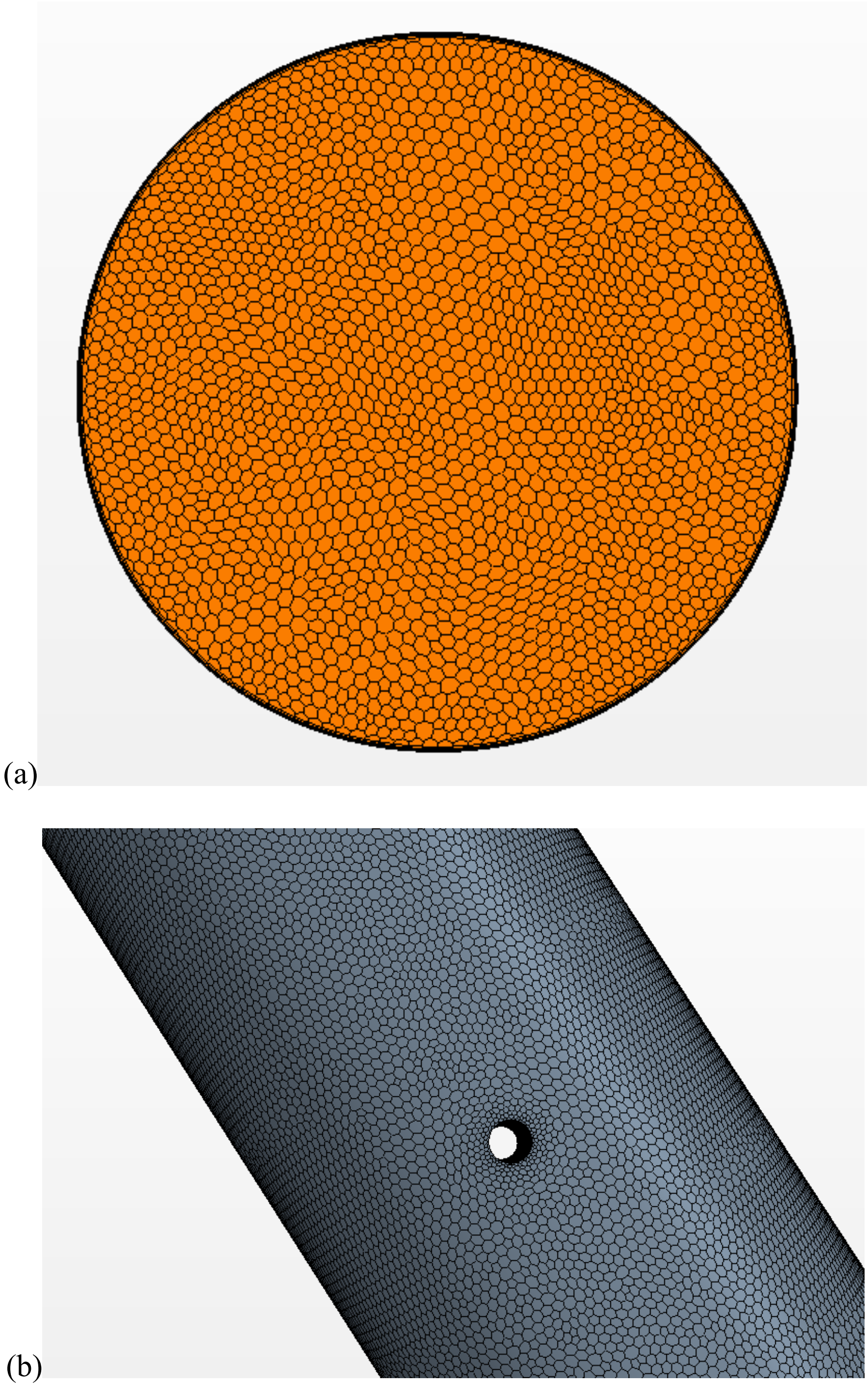

Figure 5-5. Mesh of pipe with an optic-fiber sensor (radial direction) model (a) cross-section and (b) side view

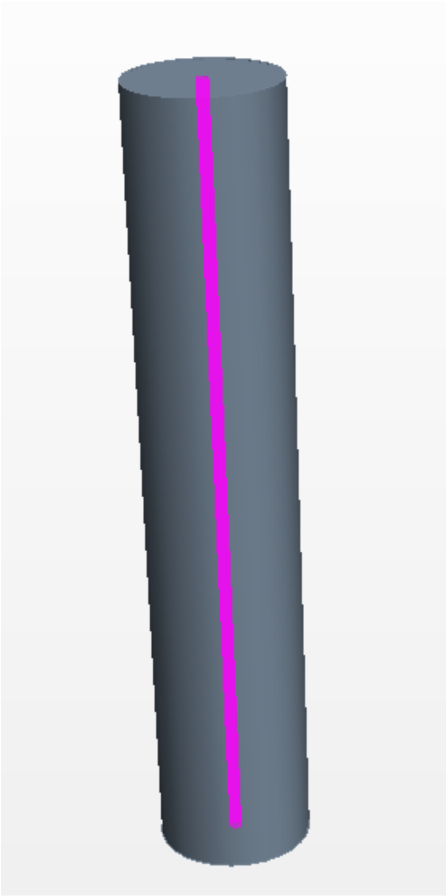

Figure 5-6. Geometry of pipe with an optic-fiber sensor (axial direction)

Table 5-4. Mesh independence study of pressure drop across the pipe with an optic-fiber sensor (axial direction)

<table>
<tr><td>Mesh</td><td>Base size (cm)</td><td>Cell number</td><td>Pressure drop between pipe inlet and outlet (Pa)</td><td rowspan="4">Mesher:
Polyhedral mesher, prism layer mesher, surface remesher, extruder
Prism layer: 4
Prism layer stretching: 1.5
Prism layer thickness: 33%</td></tr>
<tr><td>1</td><td>0.1</td><td>165,738</td><td>58.8</td></tr>
<tr><td>2</td><td>0.07</td><td>462,926</td><td>59.1</td></tr>
<tr><td>3</td><td>0.05</td><td>1,113,534</td><td>59.1</td></tr>
</table>

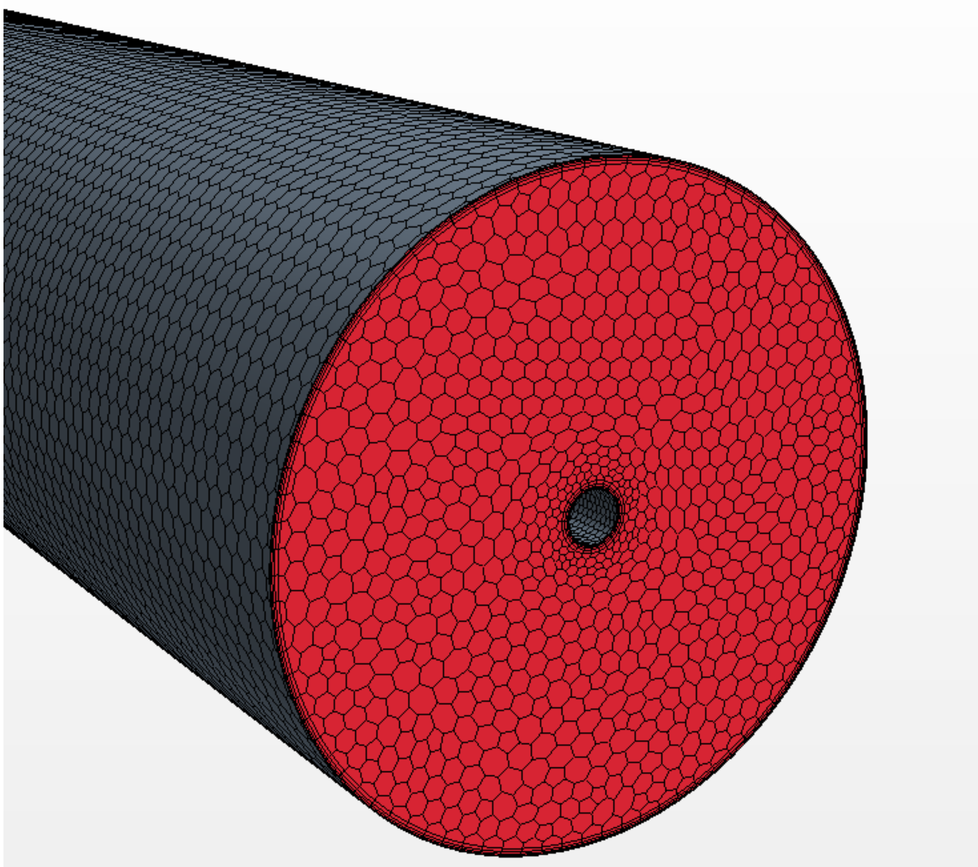

Figure 5-7. Mesh of pipe with an optic-fiber sensor (axial direction) model

$$P = f\frac{L}{D}\frac{\rho v^2}{2} + K\frac{\rho v^2}{2} \tag{5.1}$$

Table 5-5. Minor loss coefficients of SAM FLiBe natural circulation loop model

	Component numbers	Form loss coefficient (Each component)
Bend (Todreas et al., 2011)	6	0.5
Thermocouple*	7	0.81
Fiber-optics (along flow cross section)*	4	0.95
Fiber-optics (along vertical pipe)*	2	8.4

Note: * form loss coefficient is calculated from CFD

5.3 Salt Bulk Mean Temperature

In the experiment set up, the temperatures of thermocouples correspond to the salt temperatures in the center of the pipe. However, since the heating source uses radiant-mode clamshell heaters that the heat comes from outside of the pipe, large temperature gradients along heating sections are observed in the experimental data. There are four fiber-optic sensors (Fiber A to Fiber D in Figure 5-1(a)) to measure the salt temperature profiles in the radial direction in heater sections. With temperature profiles obtained from fiber-optic sensors, the measured values from thermal couples are converted to bulk mean temperatures. It is more physical to compare the one-dimensional simulation results with the bulk mean temperatures than the center temperatures (Equation 5.1). In each calculated bulk mean temperature, the flow velocity profiles are assumed as fully developed laminar flows, as shown in Equation 5.2. As shown in Figure 5-8, only TC11, TC12 and TC14 are converted to bulk mean temperatures since they are in the heating sections. The bulk mean temperatures in TC11, TC12 and TC14 are higher than the center due to external heat sources that result in lower temperatures in the center compared to salt temperatures in the pipe wall. For the salt temperature profiles in the air cooler, TC24 was expected to have a large temperature gradient due to the large temperature difference between molten salt and air. However, there is no fiber sensor in this location, so the temperature profile of TC24 is not available. In addition, the measured value of TC24 is close to downstream temperature TC35 and TC24, which the temperature profile may already flatten. Also, the location of TC24 is not exactly the outlet of air cooler so the fluid temperatures may already be well-mixed. Based on the observation, TC24 measured values can be treated as the bulk mean temperatures. For other TC locations, there is no heating and cooling in TC21, TC32 and TC35 other than heat losses, consequently, the bulk mean temperatures should be similar to the data measured by these thermocouples.

$$T_m = \frac{\int_{\dot{m}} c_p T(r)\delta\dot{m}}{\dot{m}c_p} = \frac{\int_{A_c} c_p T(r)\rho u(r) 2\pi r dr}{\rho v_{avg}\pi R^2 c_p} = \frac{2}{v_{avg}R^2}\int_0^R T(r)u(r)rdr \qquad (5.1)$$

$$v(r) = v_{max}\left[1 - \frac{r^2}{R^2}\right] = 2v_{avg}\left[1 - \frac{r^2}{R^2}\right] \qquad (5.2)$$

T_m: bulk mean temperature;

R: inner radius of a pipe;

r: radial position from the center ;

$\dot{m}$: mass flow rate;

v_{avg}: average flow velocity, the measured values in the experiment are used;

v_{max}: maximum flow velocity in the pipe center

5.4 Code Validation Results

The simulation results of the three steady state tests, test 4, 6 and 7, are shown in Figure 5-8 and Table 5-6. In this SAM model, the friction correlation $f = 64/Re$ is used to model the laminar flow in the developed flow region. The friction coefficient (f) in the developing region is also applied in the FLiBe natural circulation loop model (Langharr et al., 1942). However, the simulation results from SAM show higher natural circulation velocities and smaller temperature gradients along the FLiBe natural circulation loop. A possible explanation of the discrepancies is the flow resistances in the loop are under-estimated, including the form losses coefficients and friction coefficients. For natural circulation flow, both salt natural circulation flow velocity and salt temperature difference across the cooler mainly depend on the buoyancy force and flow resistance in the loop. With the same heat removal rates in the steady state, the larger flow velocities can cause smaller temperature differences across the cooling section (TC21 and TC24).

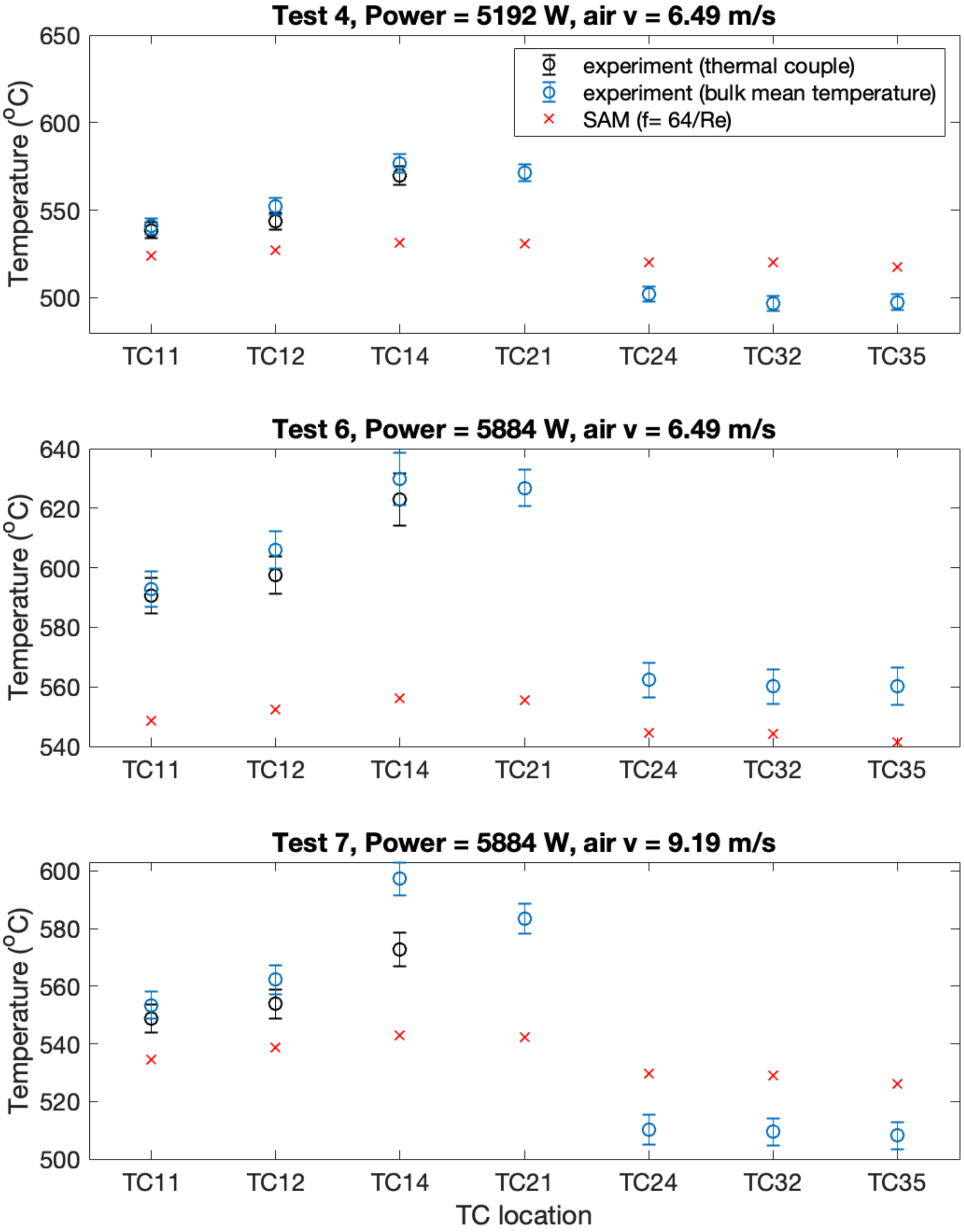

Figure 5-8. Simulation results and experimental data of FLiBe natural circulation loop (f = 64/Re in developed flow region)

Table 5-6. Comparison of salt natural circulation velocities and temperature differences across the air cooler (f = 64/Re in developed flow region)

	v (cm/s) (Experiment)	v (cm/s) (SAM simulation)	TC21-TC24 (°C) (Experiment)	TC21-TC24 (°C) (SAM simulation)
Test 4	5.43 ± 1.8	9.6	68.8 ± 7.7	10.36
Test 6	4.31 ± 0.81	9.9	75.8 ± 7.0	10.79
Test 7	4.75 ± 0.27	9.7	90.6 ± 6.8	12.69

As stated in the challenges for modeling the molten salt loop, there are high uncertainties in the molten salt thermophysical properties correlations. To further investigate this phenomenon, an uncertainty analysis of FLiBe thermophysical properties is performed. The thermophysical properties of FLiBe and their uncertainties are listed in Table 5-7. More detail information on the sampling method is discussed in Chapter 6, in this uncertainty analysis, LHS is used for the sampling to generate 125 samples for each FLiBe thermophysical property, including viscosity, thermal conductivity, heat capacity, and density.

Table 5-7. Thermophysical properties and uncertainties of FLiBe (Williams et al., 2006)

FLiBe	Correlation and value	Uncertainty
Viscosity (Pa·s)	$1.16\times10^{-5}\exp\left(\frac{3755}{T}\right)$	20%
Thermal conductivity (W/m·K)	1.1	10%
Heat capacity (J/kg·K)	2386	3%
Density (kg/m^3)	$2413 - 0.488T$	2%
Freezing point (° C)	459	-
Boiling point (° C)	1430	-

The aim of this analysis to investigate how the FLiBe uncertainties affect the quantities of interest (QoIs), including salt temperatures and velocities. Using test 4 as the main test case, the uncertainty analysis results are demonstrated in Figure 5-9, Figure 5-10 and Table 5-8. In Figure 5-9, the gray color represents the temperature range from uncertainty analysis based on the uncertainties of the FLiBe thermophysical properties. Though the gray color covers a large temperature range, the temperature variation along the loop is still not as large as the experimental data. In Table 5-8, the uncertainty analysis indicates that the uncertainties of the FLiBe thermophysical properties have little effect on the natural circulation velocity and the temperature difference across the air cooler compared to experimental data. Therefore, we can conclude the uncertainties of FLiBe thermophysical properties are not the main contribution to the large discrepancies between simulations and the experiment. However, it is demonstrated that the average salt temperature in the system is significantly affected by the FLiBe thermophysical properties. In addition, the distribution of QoIs with the four input variables is shown in Figure 5-10. The friction factor $f = \frac{64}{Re} = 64/(\frac{\rho v D}{\mu})$ is used in this model since it is in laminar flow region. Based on the friction factor, a higher viscosity results in a higher friction factor. Consequently, in Figure 5-10, the larger viscosity corresponds to a smaller natural circulation velocity in the loop can be observed. In addition, the salt temperature range of the system is strongly affected by viscosity and thermal conductivity of FLiBe, while natural circulation velocity and temperature difference across cooler are more correlated with viscosity.

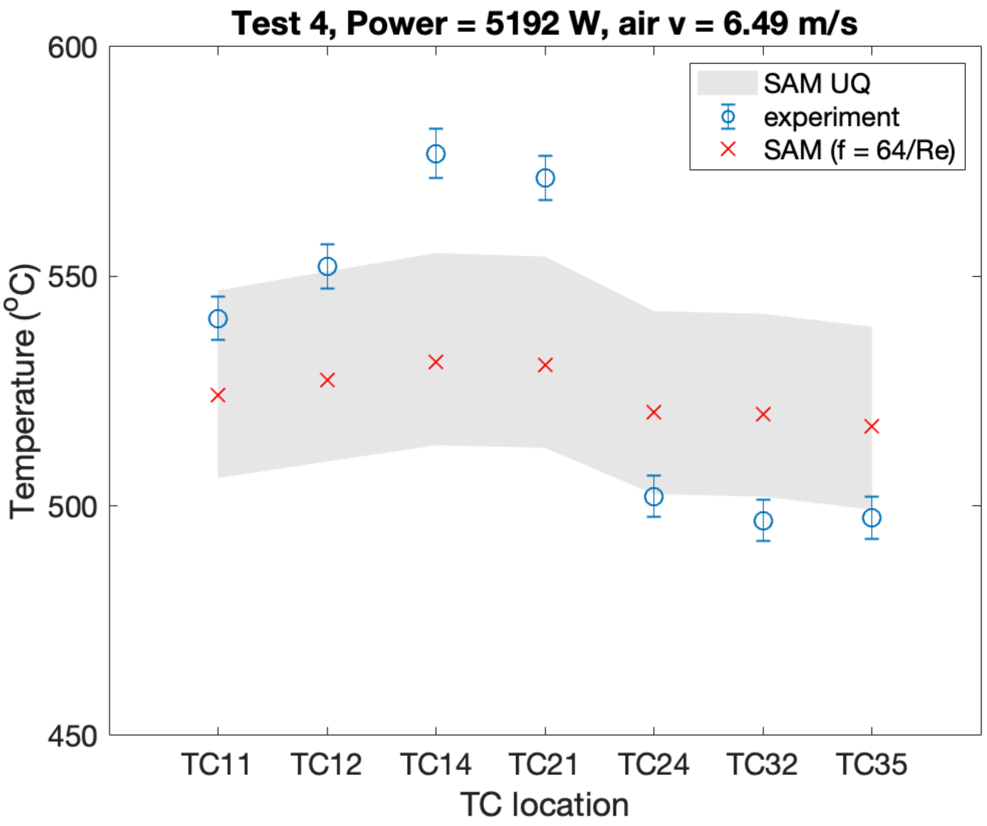

Figure 5-9 Simulation results, uncertainties of salt temperature and experimental data of test 4 (f = 64/Re in developed flow region)

Table 5-8. Uncertainties of QoIs of test 4 (f = 64/Re in developed flow region)

Test 4 SAM uncertainty analysis	Maximum	Mean	Minimum	Standard deviation	Experiment
Salt temperature (TC11)(°C)	546.9	525.1	506.1	9.58	538.6 ± 7.7
Velocity (cm/s)	10.18	9.53	8.87	0.35	5.43 ± 1.8
Salt temperature difference across cooler (°C)	12.6	10.9	9.6	0.6	68.8 ± 7.7

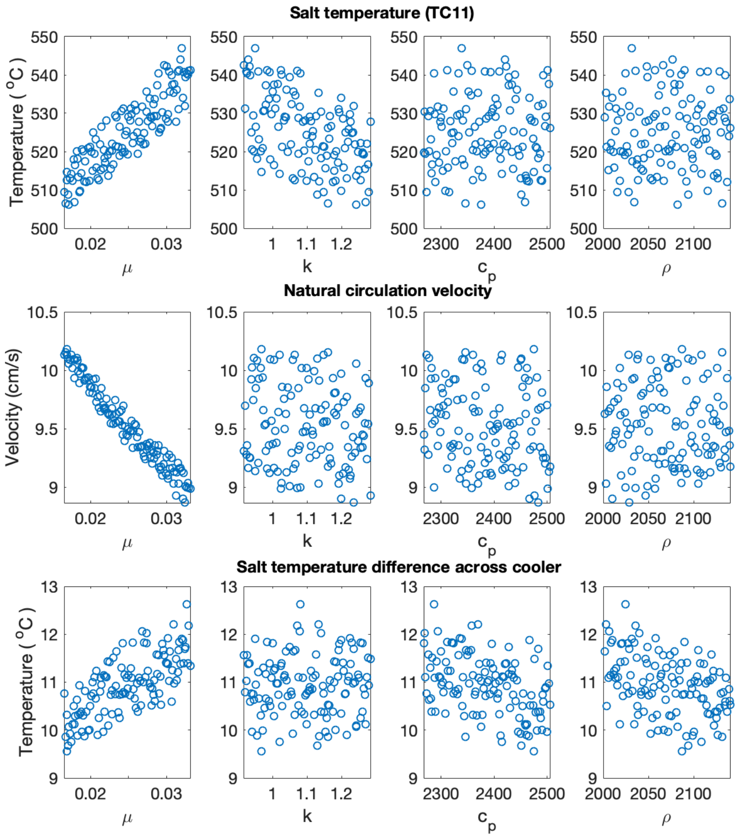

Figure 5-10. Uncertainty analysis results with four input variables

To further investigate the discrepancies between SAM modeling and experimental data, it is found that the new SAM model with a friction multiplier of 14 (f'=14*f) applied along the whole loop can help decrease the temperature discrepancies between simulation and experimental data. The results with the larger friction coefficients applied are shown in Figure 5-11 to Figure 5-13 with 6 test cases compared. With friction multiplier of 14 applied in the modeling, the salt temperature differences between cooler inlet and outlet become 5.72 to 6.44 times larger and natural circulation velocities decrease to the ratio of 0.17.

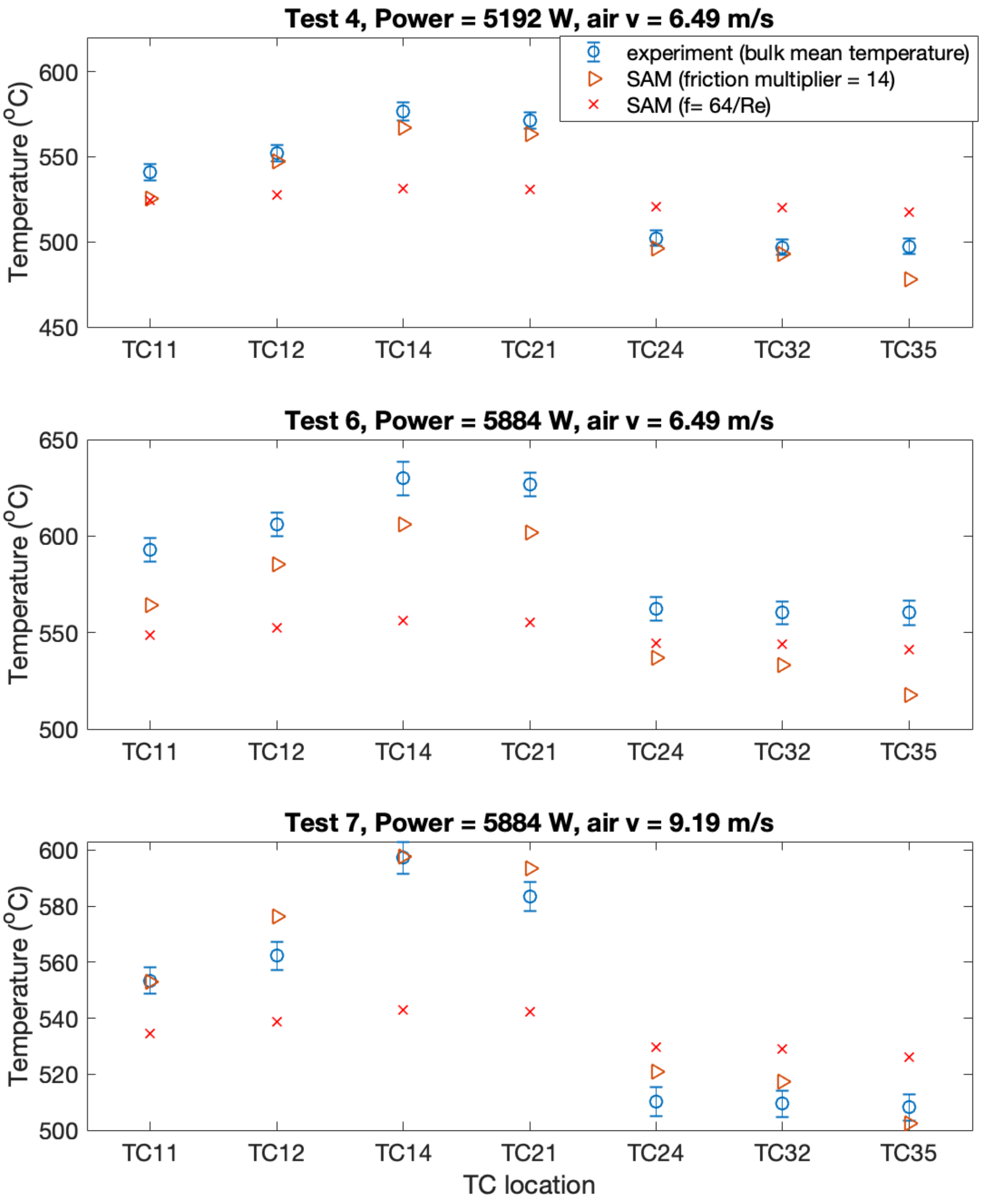

Figure 5-11. Simulation results and experimental data of test 4, 6 and 7 (friction multiplier = 14)

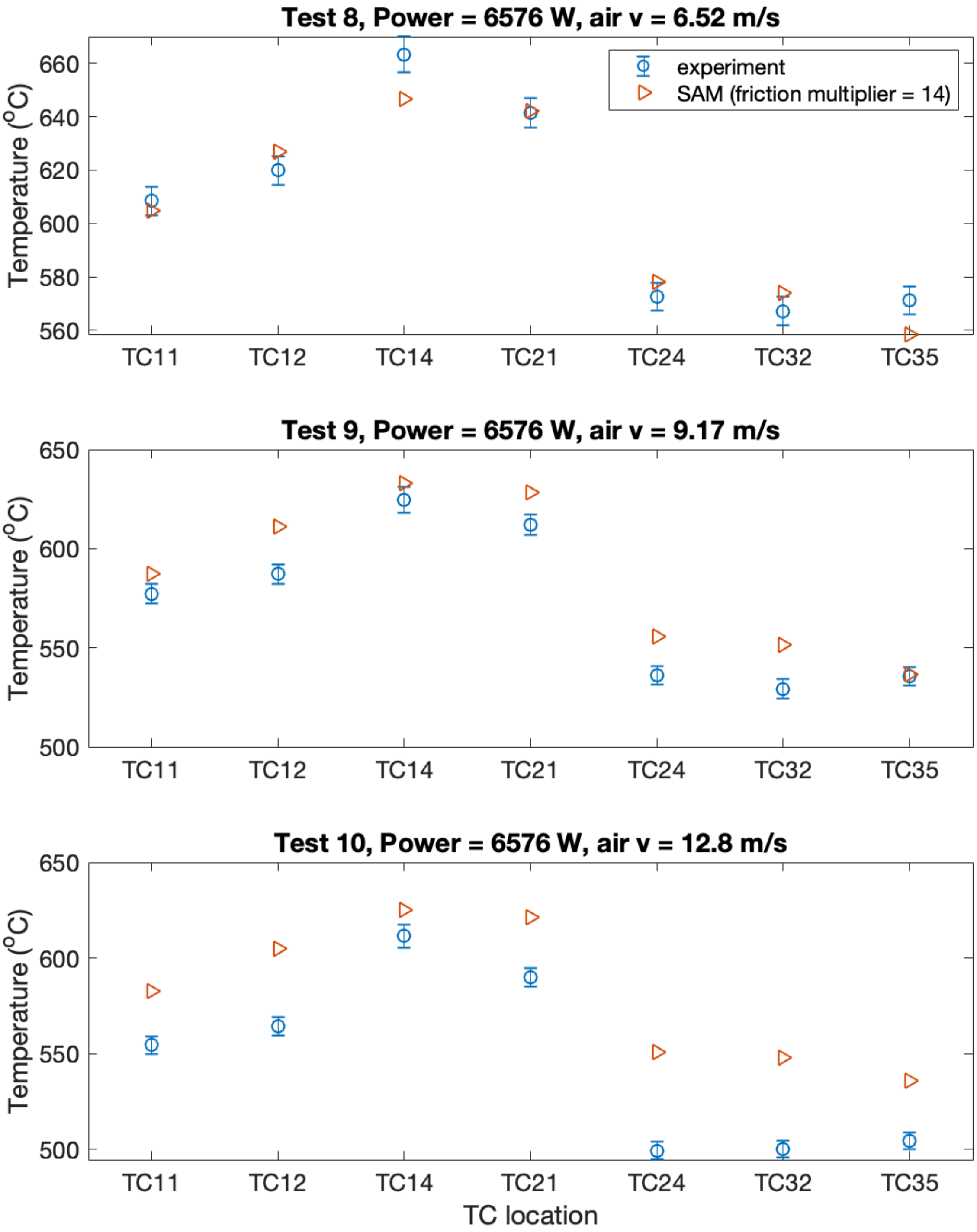
Test 8, Power = 6576 W, air v = 6.52 m/s

Test 9, Power = 6576 W, air v = 9.17 m/s

Test 10, Power = 6576 W, air v = 12.8 m/s

Figure 5-12. Simulation results and experimental data of test 8, 9 and 10 (friction multiplier = 14)

The comparison between experimental data and the simulation results of air and salt temperature differences across air cooler and salt natural circulation velocities are summarized in Figure 5-13. The heat addition into the system is from the four heaters, the heat is balanced by the air cooler and heat loss to the environment. The air inlet temperatures and air velocities are boundary conditions based on the measured data, therefore, the modeling results of the air temperature differences across air cooler can be used to indicate the cooling capability in the air cooler. In Figure 5-13 (a), the simulation results of air temperature increase with higher friction factors applied to the model show reasonable agreement. The differences between simulation and experiment of the air temperature increases across air cooler in test 4, 6 and 8 are within 4%. The simulation results overpredict the air temperature increases across cooler of test 7, 9 and 10 are within 32% compared to the experimental data.

For salt temperature decreases across the air cooler (See Figure 5-13(b)), the simulation results are close to the error bar of the experimental data except test 7 which is 27% higher than the experiment. For the natural circulation velocities (Figure 5-13c), the simulation results are smaller compared to the experimental data. Based on the heat balance, with the same heat input into the system (boundary condition) and the same air cooling capability (verified by the air outlet temperature), the natural circulation velocities have to be small to reach the heat balance and to have large temperature variations along the loop. It is plausible that several limitations could have influenced the results obtained in the experiment, such as flow measurement. From the experiment (Britsch et al., 2019), the salt velocity is hard to measure by equipment nowadays due to the very small flow velocity of the natural circulation flow and very high temperature in the system. In the experiment, the thermal pulse method is used to measure the flow velocity which can cause large measurement uncertainties though not reported in the experiment. Compared to measured velocities, the measured temperatures from thermocouples should be more helpful for the code validation study.

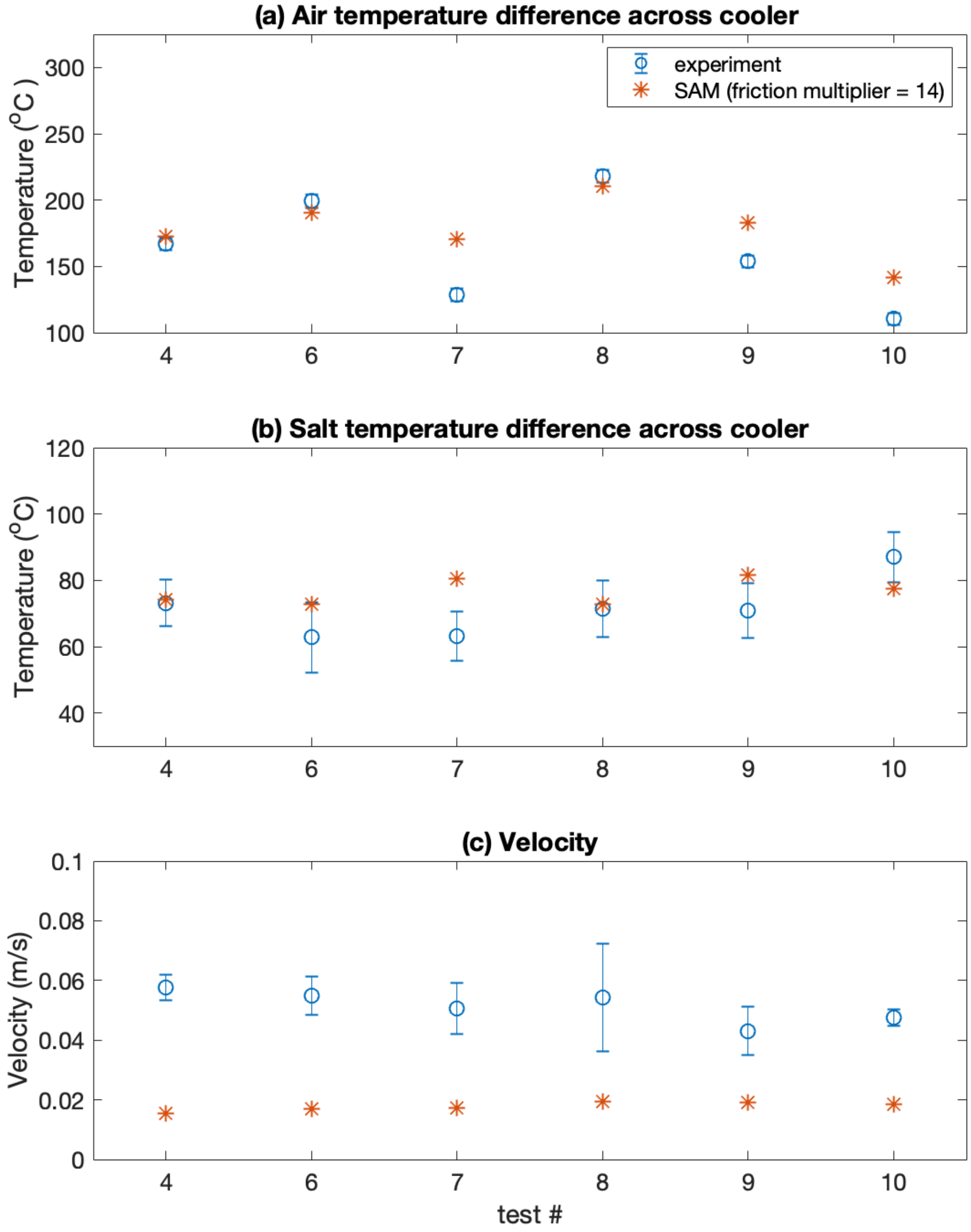

Figure 5-13. Simulation results and experimental data of test 4, 6, 7, 8, 9 and 10 (friction multiplier = 14)

Another uncertainty analysis of the FLiBe loop SAM model with larger flow resistance is also performed. Figure 5-14 and Table 5-9 show the uncertainty range of salt temperatures along the loop based on the uncertainty analysis of FLiBe thermophysical properties.

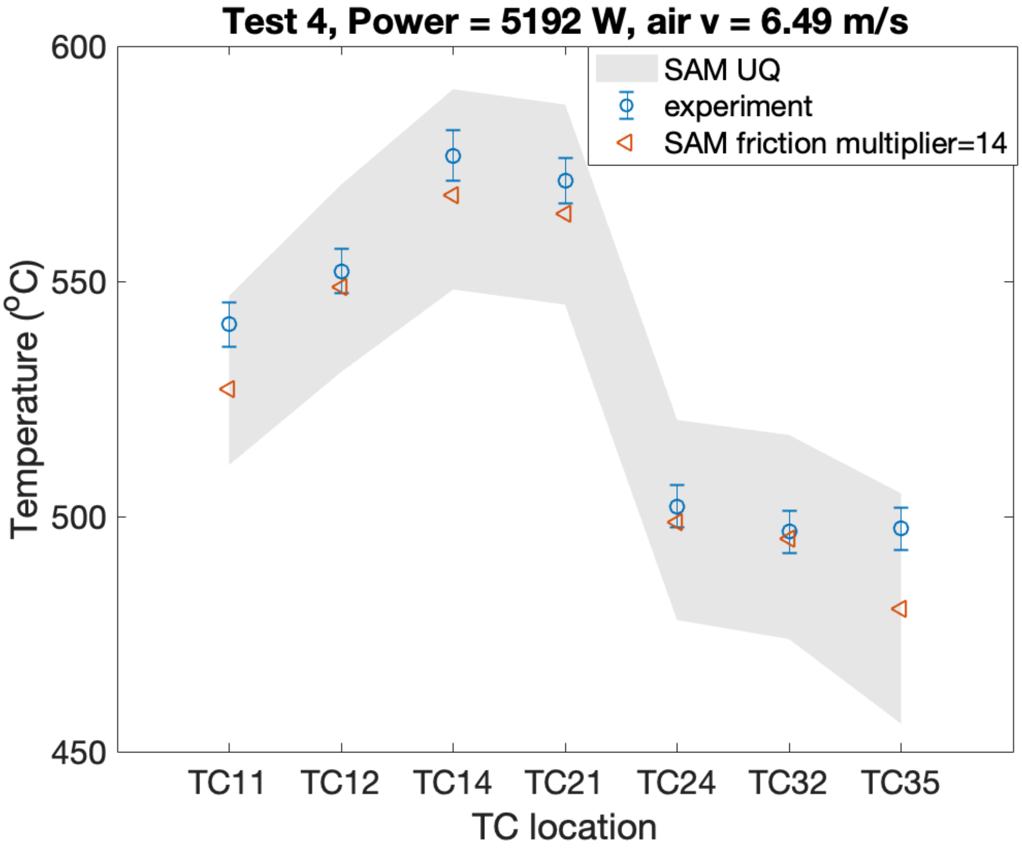

Figure 5-14. Simulation results, the uncertainty of salt temperature and experimental data of test 4 (friction multiplier = 14)

Table 5-9. Uncertainty of QoIs of test 4 (friction multiplier = 14)

Test 4 SAM simulation (friction multiplier = 14)	Maximum	Mean	Minimum	Standard deviation	Experiment
Salt temperature (TC11) (°C)	549.0	532.6	516.6	10.1	538.6 ± 7.7
Velocity (cm/s)	2.44	1.93	1.48	0.24	5.43 ± 1.8
Salt temperature difference across cooler (°C)	72.7	56.9	42.9	6.8	68.8 ± 7.7

From the simulation results compared to the experiment of the six tests, it is observed that the flow resistances are under-predicted in the SAM model. The possible explanation for the large flow resistance in the loop can be the potential freezing film the loop, especially near the heat exchanger outlet. When the salt is overcooled, the freezing film along the pipe wall narrows the flow areas and increase the flow resistances. To further examine the salt freezing phenomenon, CFD simulation on the air cooler is performed in the STAR-CCM+ model, as shown in Figure 5-15. The fluid in the center region is FLiBe and the outer annular region is the cooling air. FLiBe flow in the SS316 pipe with 3mm thickness and 19.4 mm inner diameter. The inner diameter of the annulus outer pipe is 60 mm. Due to lower heat loss in the air cooler compared to the whole FLiBe natural circulation loop, the adiabatic boundary is chosen in the outer pipe of air cooler in the STAR-CCM+ model. For the boundary conditions of the air cooler, inlet velocities and inlet temperatures of air and FLiBe and pressure outlets are assigned in the air cooler. Based on the flow regime, the model of laminar flow is chosen in the salt region while k-ε is used in modeling the air region. The results of the mesh independence study are summarized in Table 5-10. Four meshes are tested based on the base size (See Figure 5-16). The salt temperatures in the pipe are chosen as the reference values for the mesh independence study. When the base size is smaller than 0.15 cm the salt center temperature reaches the stable value, hence the mesh 3 (base size =0.15 cm) is chosen for this study. An additional figure of the mesh layout (mesh 3) of the air cooler is shown in Figure 5-17.

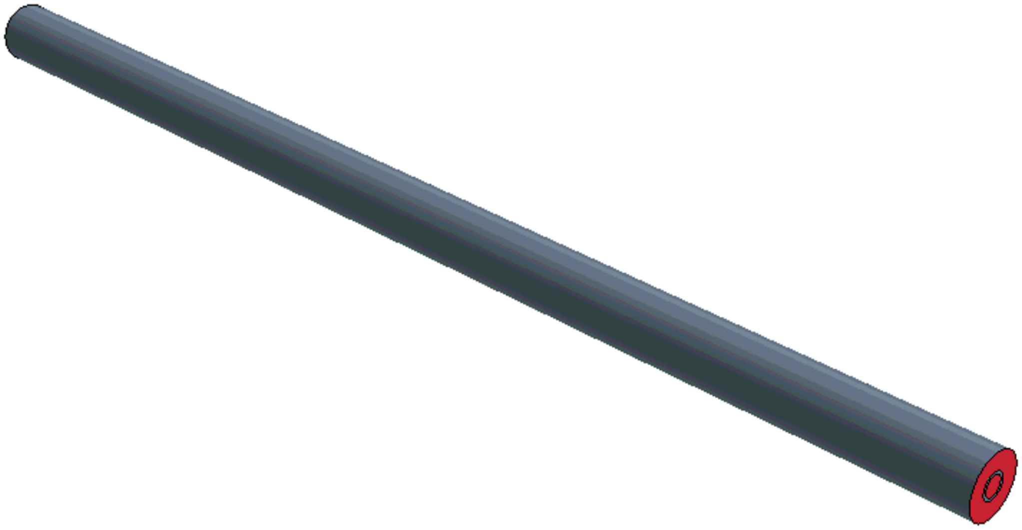

Figure 5-15. Geometry of the air cooler in STAR-CCM+

Table 5-10. Mesh independence study of air cooler model

Mesh	Base size (cm)	Cell number	Salt outlet temperature at pipe center (°C)	Mesher: Polyhedral mesher, prism layer mesher, surface remesher, extruder Prism layer: 3 Prism layer stretching: 1.5 Prism layer thickness: 33 %
1	0.3	118,330	543.59	
2	0.2	163,245	544.02	
3	0.15	263,366	545.87	
4	0.12	418,588	545.87	

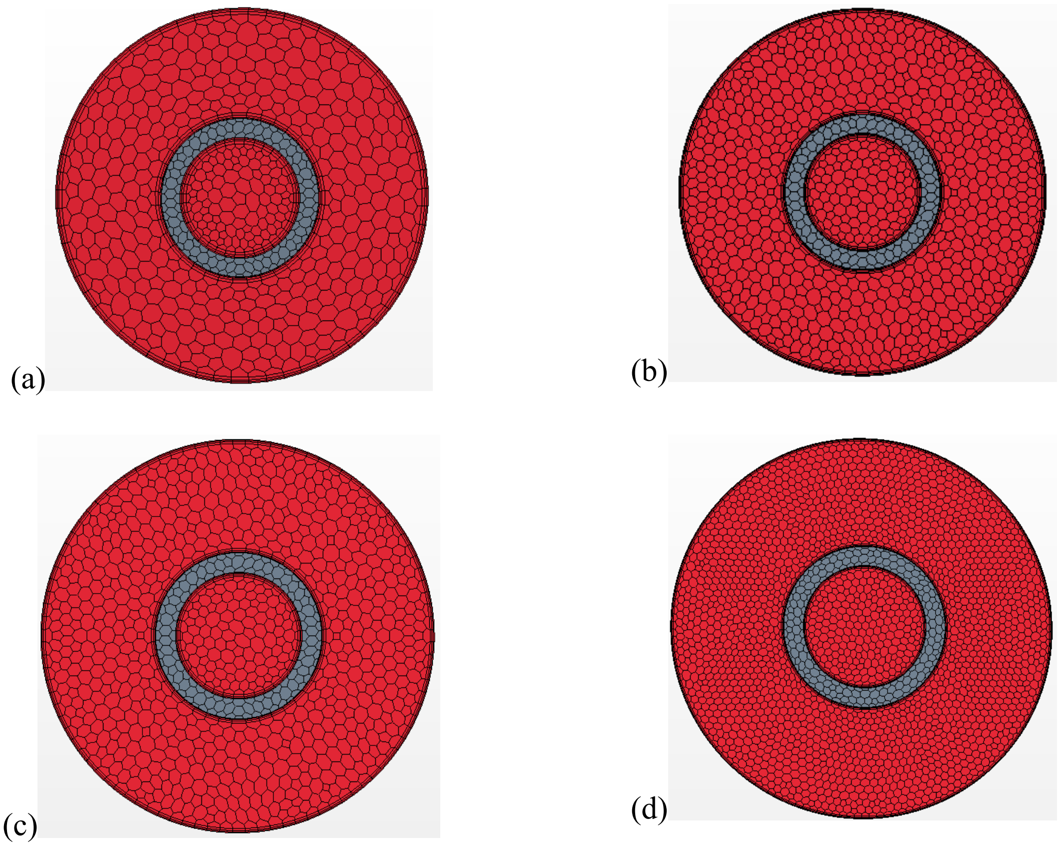

Figure 5-16. Crossection view of (a) mesh 1 (b) mesh 2 (c) mesh 3 and (d) mesh 4

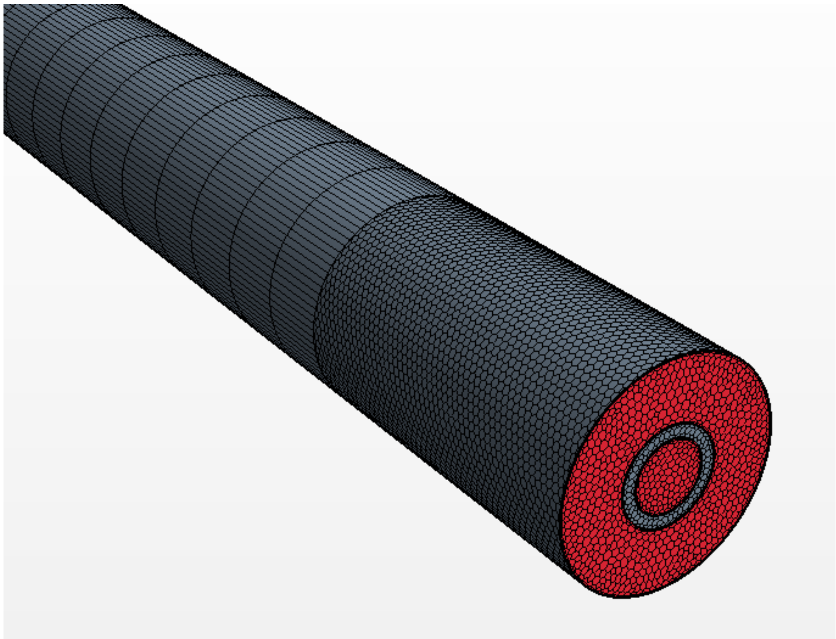

Figure 5-17. Meshes layout of mesh 3

The temperature distributions of salt and air in the air cooler of test 4 are shown in Figure 5-18. In addition, Figure 5-19 shows the salt temperature profiles along the radial direction at the cooler outlet. Though the salt temperatures close to the pipe wall in test 10 and test 6 are about 80 °C higher than the freezing point, there are high probabilities that freezing film could exist in the other four tests based on the CFD analysis. In the cooler outlets of the six tests, the salt temperature differences between the pipe center and wall ranged from 40 to 57.7 °C. However, this phenomenon cannot be validated in the current stage. Further investigation, such as measuring the temperature in the inner pipe wall or obtaining the temperature profile from fiber-optic sensors, are needed to help identify the freezing film in the pipe. Also, the function of modeling the freezing phenomenon is not available in SAM.

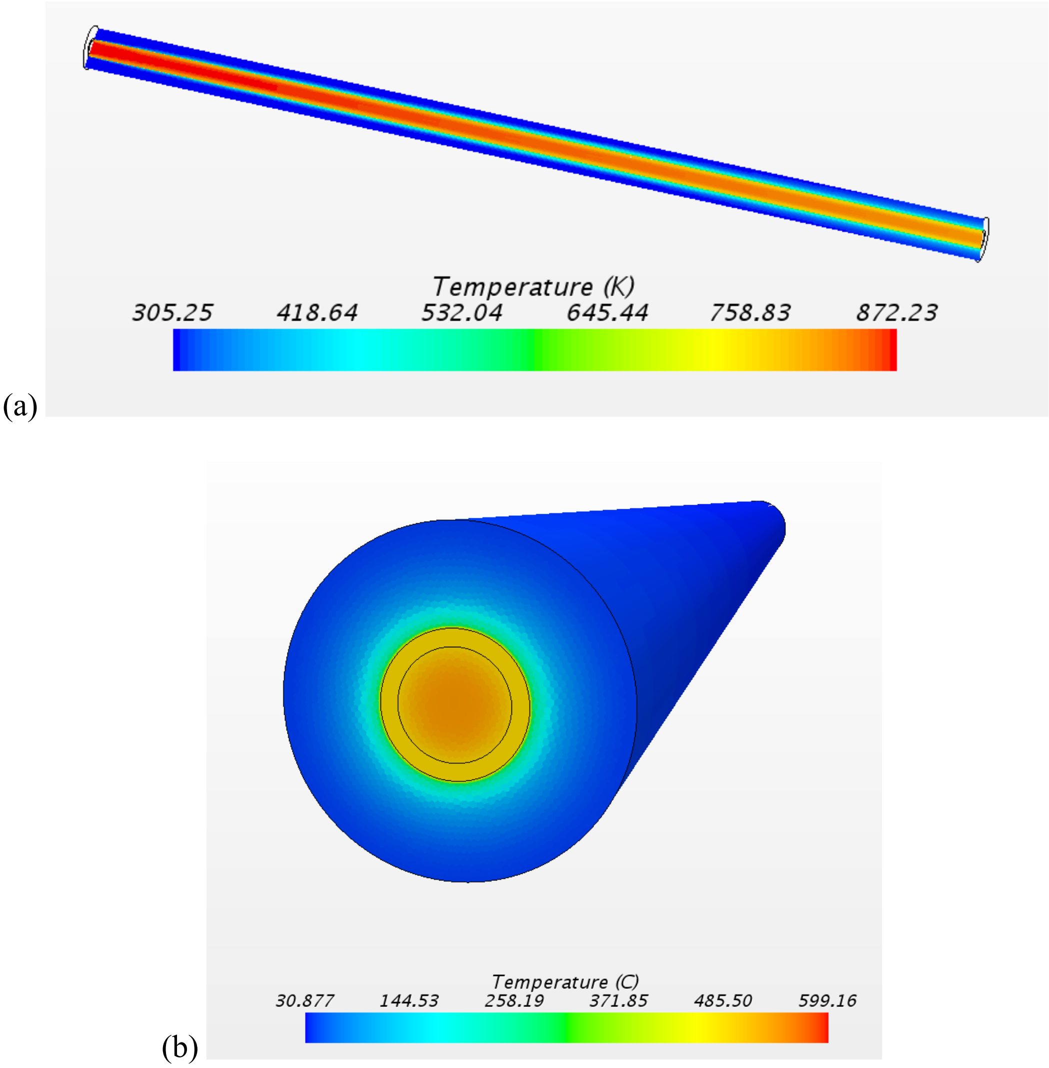

Figure 5-18. Salt temperature distribution (a) along axial direction (b) cooler outlet of test 4 from CFD analysis

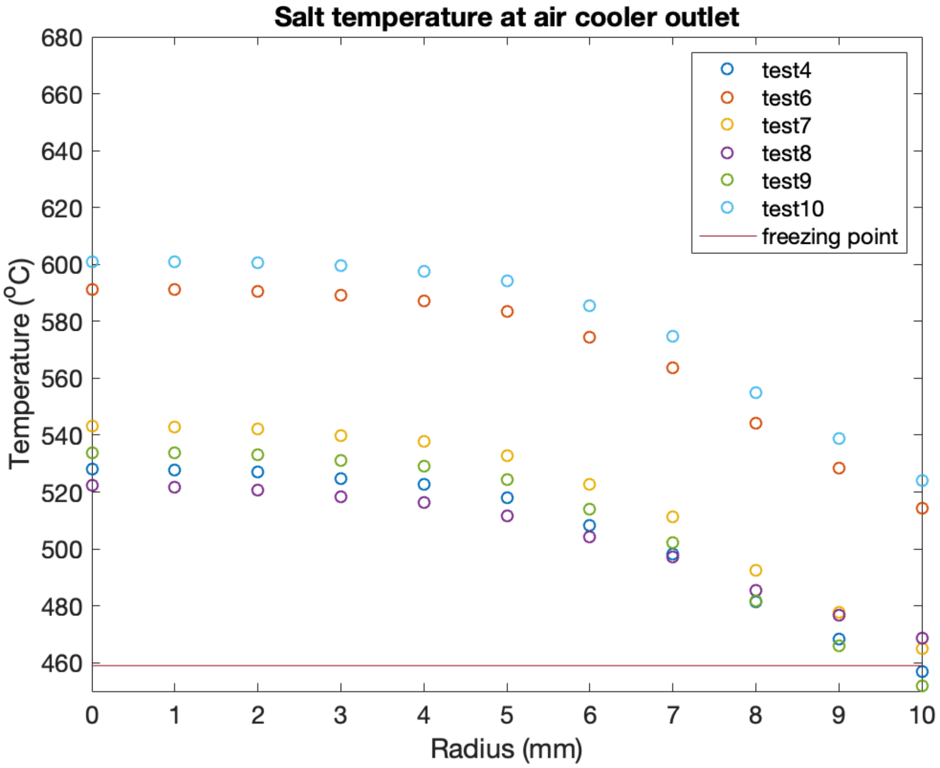

Figure 5-19. Salt temperature profiles of test 4, 6, 7, 8, 9 and 10 from CFD analysis

The effect of form loss coefficients due to salt freezing is also simulated. An orifice in the salt pipe is used to simulate the flow blockage at the air cooler outlet due to salt freezing, as shown in Figure 5-20. The form loss with respect to reduced flow area and pipe diameter can be calculated in Equations 5.3 and 5.4 (International Organization of Standards, 1998). The form loss coefficient calculated from Equation 5.3 with diameter ratios of orifice and pipe is shown in Figure 5-21. From SAM simulation, it is found that with a form loss coefficient (K) at about 2,300 applied in the pipe at the air cooler outlet can match the results of friction a multiplier of 14. However, K = 2,300 corresponds to the flow area diameter reduced to 0.2, which is much larger compared to the freezing film thicknesses in CFD simulation. Therefore, the freezing phenomenon is not the only factor contribute to the large flow resistance in the system.

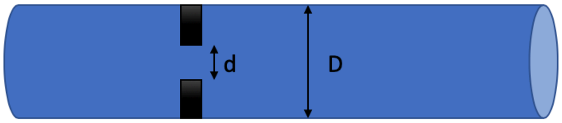

Figure 5-20. Orifice in a pipe

$$K = \left(\frac{\sqrt{1-\beta^4} - C\beta^2}{\sqrt{1-\beta^4} + C\beta^2}\right)\left(\frac{1-\beta^4}{C^2\beta^4}\right) \tag{5.3}$$

$$\beta = \frac{d}{D} \tag{5.4}$$

C: orifice discharge coefficient, 0.6 is selected as a standard case

d: reduced flow diameter ;

D: the pipe diameter

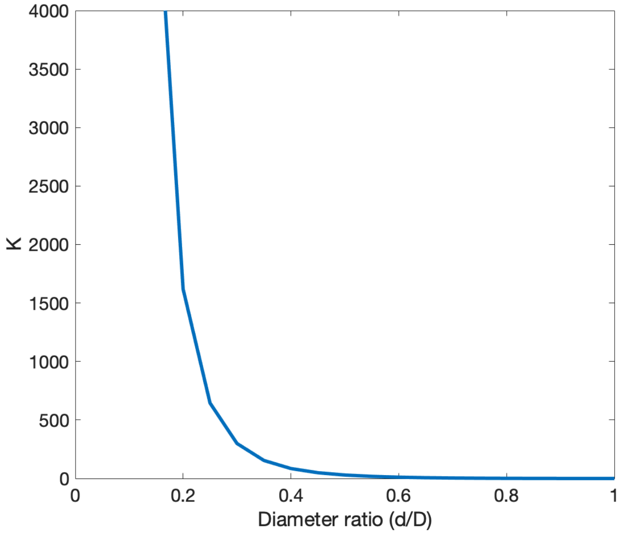

Figure 5-21. Form loss coefficient with diameter ratio of orifice and pipe

The other possible factor for the large flow resistance is the corrosion of the pipe made of SS316L. Though SS316 L is treated as stable in the FLiBe environment, the experimental data indicates some tests performed in the later time had significantly lower Nusselt number (Nu) in the heater section. The decreased Nu may, due to pipe corrosion, reduce the heat transfer capability and affect the flow conditions in the system. The corrosion can also change the salt properties due to dissolved elements in the FLiBe, or result in compounds deposited on the pipe inner surface. However, the effect of pipe corrosion on the heat transfer and flow pattern is not well-understood, and further research is needed to understand this phenomenon.

Several challenges can be observed both in the experiment and simulation from the results of code validation on the molten salt loop.

- A large amount of heat loss

  As the molten salt loop is a high temperature system, heat loss is also a factor that majorly affects the heat balance in the system. It is better to measure the structural temperature and insulation surface temperature to validate the heat loss model. Since the heater of the system used radiant-mode clamshell heaters, some heat loss from the heaters to the ambient air is expected.

- Lage temperature gradient in the radial direction

  Based on the temperature profiles measured by fiber-sensors, the temperature gradients in the radial direction are very large in the heating section, which can also be observed in the cooling section from the CFD analysis results. Accurately controlling the location of thermal couples or obtaining the temperature profiles in the cross-section could greatly benefit code validation.

- Potential salt freezing issue

For the salt loop, it is better to investigate the freezing phenomenon in the experiment and simulation since it can happen when salt is over-cooled that freezing layers start to clog the flow channel.

- Pipe corrosion

  The experimental data indicates potential corrosion phenomena caused by a significantly decreased Nusselt number in the heater section. Any entrained oxygen and moisture can increase the speed of salt corrosion to the pipe material. A well-controlled system is needed for the molten salt loop, which makes operation more challenging.

This study has enhanced our understanding of the challenges in molten salt modeling and experimental facilities. Further investigation through simulation and experiments is needed to verify the potential issues such as heat loss, salt freezing, and pipe corrosion.

Chapter 6 Uncertainty Analysis of HT-FSTF

A high-temperature fluoride salt test facility (HT-FSTF) is designed for testing lab-scale heat exchangers, key components and instrumentation under molten salt environments and passive decay heat removal capability (Zhang et al., 2019). Figure 6-1 and Figure 6-2 show the three-dimensional layout and photo of HT-FSTF, respectively. The design concept of the test facility is similar to DRACS, there are three loops in HT-FSTF, namely, the primary loop (red loop), the DRACS loop (yellow loop) and the air loop (grey loop) illustrated in Figure 6-1. In HT-FSTF, the main components include a reservoir tank for salt storage, a simulated core for heating, a primary molten salt pump, high-temperature valves, a secondary molten salt pump, DHX, and NDHX. Compared to other candidate molten salts such as FLiBe and KF-ZrF$_4$, FLiNaK is selected as the coolant salt in the primary and DRACS loop in HT-FSTF since it is easier to process and produce in the lab. This is a high temperature system that the design of HT-FSTF can reach up to 700 °C in the primary loop. Stainless steel 316 (SS 316) is used as the piping material in HT-FSTF. The air-to-water heat exchanger in the closed air loop, chilled water in the tube side of the serves as the ultimate heat sink for HT-FSTF.

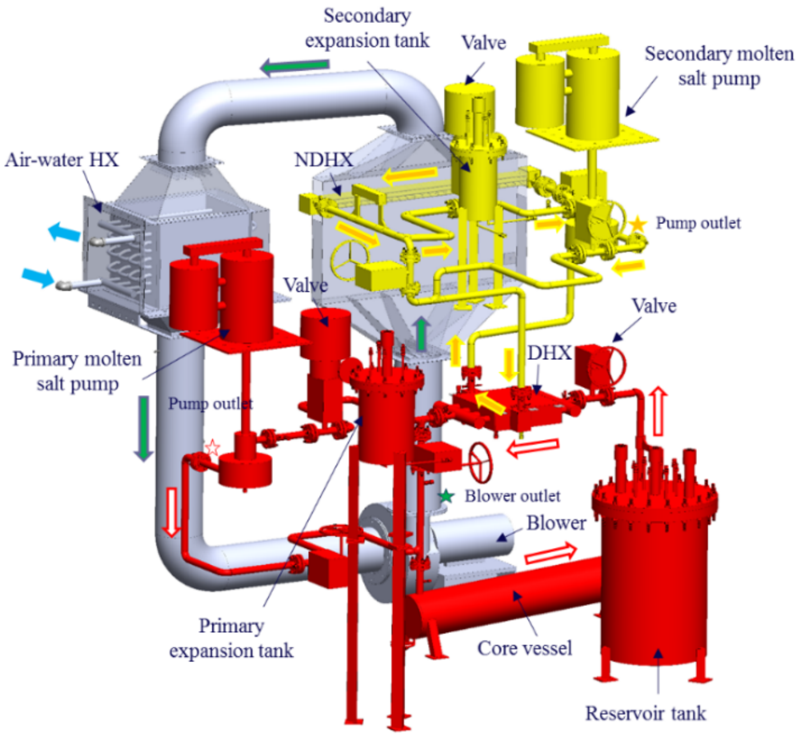

Figure 6-1. Three-dimensional layout of HT-FSTF (Zhang et al., 2019).

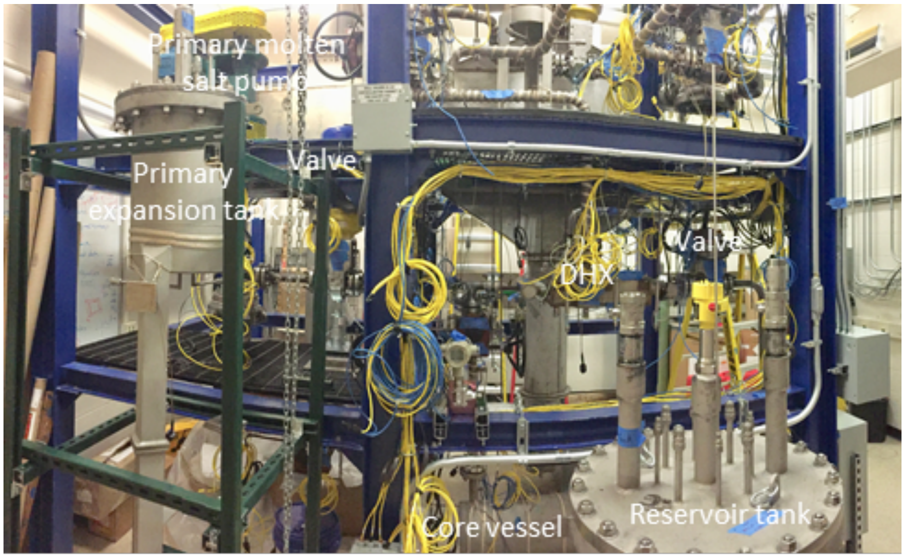

Figure 6-2. Photo of HT-FSTF (Zhang et al., 2019).

Fluted tubes have enhanced heat transfer capability with increased heat transfer area and more turbulent flow compared to plain tube. In addition, a fluted tube heat exchanger has a lower pressure drop compared to a compact heat exchanger. Therefore, the fluted tube heat exchanger design is adopted in DHX and NDHX in HT-FSTF. The design parameters of DHX and NDHX are listed in Table 6-1 (Zhang et al., 2019). Both DHX and NDHX use the same fluted tube geometry but different tube lengths, the detail information is summarized in Table 6-2 and Figure 6-3.

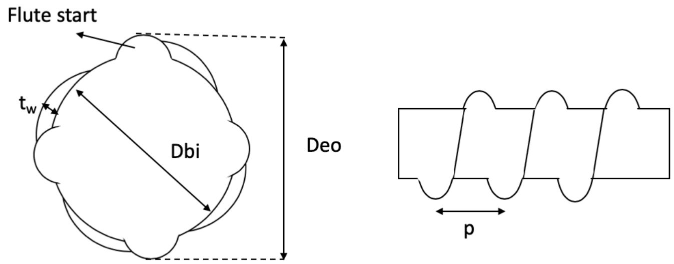

Figure 6-3. Geometry of fluted tube

Table 6-1. Design parameters of DHX and NDHX in HT-FSTF (Zhang et al., 2019)

NDHX	
Shell/fluted tube-side	Air/ DRACS side
Tube number	11
Tube length (m)	1.3208
Shell side thickness (mm)	6.3
Shell side inner width (m)	0.0996
Shell side inner height (m)	0.6350
Heat transfer area (m^2)	0.21
DHX	
Shell/fluted tube-side	Primary/ DRACS side
Tube number	12
Tube length (m)	0.4572
Shell side thickness (mm)	3.2
Shell side inner width (m)	0.1118
Shell side inner height (m)	0.4445
Heat transfer area (m^2)	0.661

Table 6-2. Fluted tube design in DHX and NDHX in HT-FSTF (Zhang et al., 2019)

Fluted tube	
Number of flute start (Ns)	3
Inner bore diameter (D_{bi}) (mm)	10.7
Flute distance (p) (mm)	10.2
Tube side thickness (t_w) (mm)	0.711

The heat transfer correlations in fluted tubes are used in the SAM model. In these correlations, the Nusselt number is a function of the Reynolds number, Prandtl number, and fluted tube geometry. Equations 6.1 and 6.2 are heat transfer correlations for the fluted tube with a certain range of the Reynolds number (Srinivasan., 1993).

$$Nu = 0.014Re^{0.842}Pr^{0.4}e^{*-0.067}p^{*-0.293}\theta^{*-0.705} \quad \text{for } Re \leq 5{,}000 \tag{6.1}$$

$$Nu = 0.064Re^{0.773}Pr^{0.4}e^{*-0.242}p^{*-0.108}\theta^{*0.599} \quad \text{for } 5{,}000 \leq Re \leq 82{,}000 \tag{6.2}$$

where the three dimensionless parameters, p^*, e^* and θ^*, in the fluted tube heat transfer correlations represent:

p^* = nondimensional flute pitch (p/D_v)

p = flute pitch (mm)

D_v = volume-based fluted tube diameter (mm)

e^* = nondimensional flute depth (e/D_v)

e = flute depth (mm)

θ^* = nondimensional flute helix angle ($\theta/90$)

θ = flute helix angle ($tan^{-1}(\pi D_v/N_s)$) (deg)

N_s = number of flute starts

6.1 SAM HT-FSTF Model of the DRACS Loop

Similar to Chapter 5, because of the flexibility in changing coolant properties in the input file SAM is chosen for this uncertainty analysis. The SAM HT-FSTF model of the DRACS loop and natural circulation flow direction is shown in Figure 6-4. Both DHX and NDHX has 40 volume numbers. The PBTDV is used in the model to manage the boundary conditions of primary and air loop inlet and outlet, including coolant inlet temperature and inlet velocity. The piping and both heat exchangers are designed with a 3-inch-thick of high temperature insulation. Similar to previous cases, the heat transfer coefficient from the insulation surface to ambient air is calculated by Churchill and Chu (Churchill and Chu.,1975). The ambient air is assumed at a constant temperature of 27 °C.

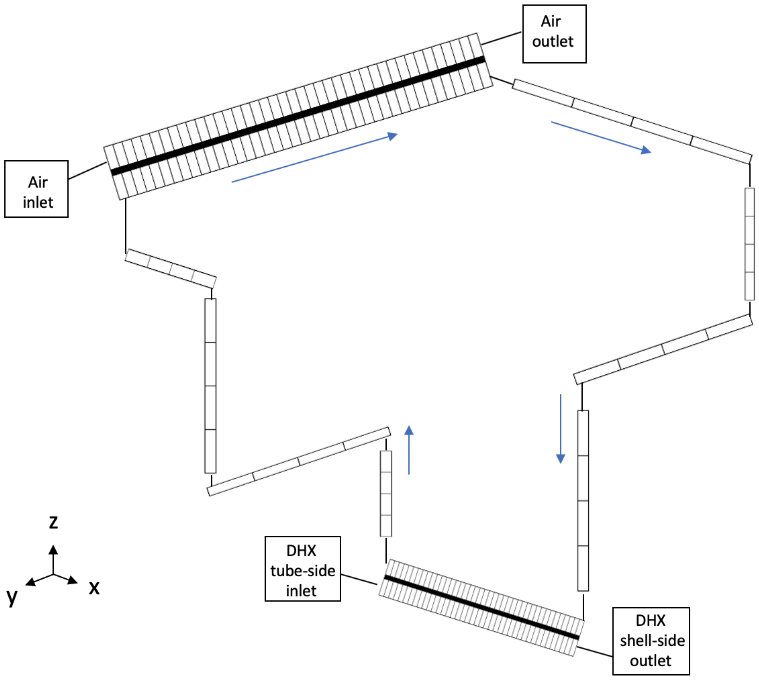

Figure 6-4. Nodalization of SAM HT-FSTF model

HT-FSTF uses FLiNaK as the coolant in DRACS and the primary loop. Molten salt thermophysical properties are reported in the literature to contain relatively large measurement uncertainties, especially for the viscosity and thermal conductivity (William, 2005). The main objective of this task is to study the effect of molten salt thermophysical property uncertainties on the uncertainties of the predicted quantities of interest (QoIs), such as the salt natural circulation velocity and temperature by the SAM code. Multiple calculations are carried out based on probabilistic distributions of the thermophysical properties and the output ranges of QoIs can be obtained. Two transients are performed including overpower (OP) transient and overcooling (OC) transient to investigate the thermal responses of the DRACS loop.

In the uncertainty analysis, 175 samples are generated using the Latin hypercube sampling (LHS) (McKay et al., 1979) method based on four input variables of FLiNaK thermal properties, including viscosity, thermal conductivity, heat capacity, and density. For sampling size quantification, the upper bound value can be estimated with a certain confidence level from Wilks' formula (Wilks 1941 and 1942), for example, estimated the response of the 95th percentile at a 95% confidence level. Based on Wilks' formula, 59 sample number is needed for the first maximum response value within the upper 5% range at least a 95% confidence level. To reach the 95/95 tolerance limit, the minimum sample numbers of 93 and 124 for the second and third largest responses are required. Therefore, 175 samples can guarantee at least the third order maximum response can reach 95/95 value in this study.

LHS is a statistical method that widely used for a near-random sample generation from different input variables. Hypercube refers to a cube with more than three dimensions, so the sampling can be formed based on multiple dimensions/variable inputs. For each input variable, it is divided into N intervals with the same probability in the cumulative density functions (CDF) first. The divided interval variable will be chosen only once in each sampling. The input variables need to be independent of other input variables. The example LHS from two variables, x, and y, is shown in Figure 6-5 with one sample in each row and each column. LHS tends to have more evenly distributed sample points without generating distorted or biased samples. The uncertainties of FLiNaK's thermal properties are listed in Table 6-3.

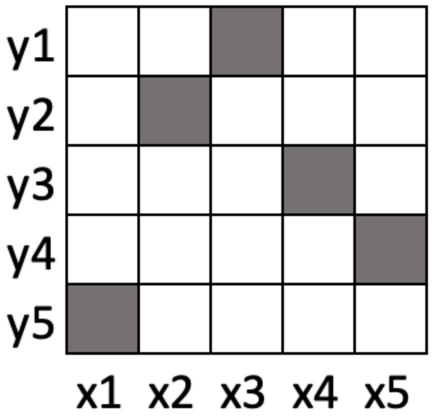

Figure 6-5. Latin hypercube sampling points demonstration

Table 6-3. Thermophysical properties and uncertainties of FLiNaK (Romatoski et al.,2019)

FLiNaK	Correlation and value	Uncertainty
Viscosity (Pa·s)	$4{\times}10^{-5}\exp\,(\frac{4170}{T})$	10%
Thermal conductivity (W/m·K)	$0.36 + 0.00056T$	10%
Heat capacity (J/kg·K)	1884	10%
Density (kg/m^3)	$2579 - 0.624T$	2%
Freezing point (° C)	642	-
Boiling point (° C)	1570	-

6.2 Overpower (OP) Transient

A step increase of the primary inlet temperature is to simulate sudden power increase or temperature increase due to primary flow reversal. The step change of primary inlet temperature is called overpower transient to simulate sudden power change in the scenario though there is no heater or power history involved in the simulation. OP transient analysis is carried out to evaluate the transient responses in the DRACS loop when the primary temperature increases.

Before the OP transient, a steady state is reached with the primary inlet velocity of 2 cm/s and primary inlet temperature 650 °C and air inlet velocity of 10 cm/s and air inlet temperature 27 °C. During the transient initiation, the primary loop salt inlet temperature increases from 650 °C to 700 °C. The simulation results of OP of 175 samples are plotted in Figure 6-6 and Figure 6-7 where the red thick line is the base case. Due to the primary temperature increase, the DRACS salt temperature increase as well. The salt natural circulation velocities also increase resulted from the primary temperature increase which leads to a higher buoyancy force. Both DRACS salt temperature and salt natural circulation velocity reach to new steady state at about 4,000 s. The DHX outlet temperature is chosen as QoI for the temperature since it is the peak temperature of the DRACS salt in OP transient.

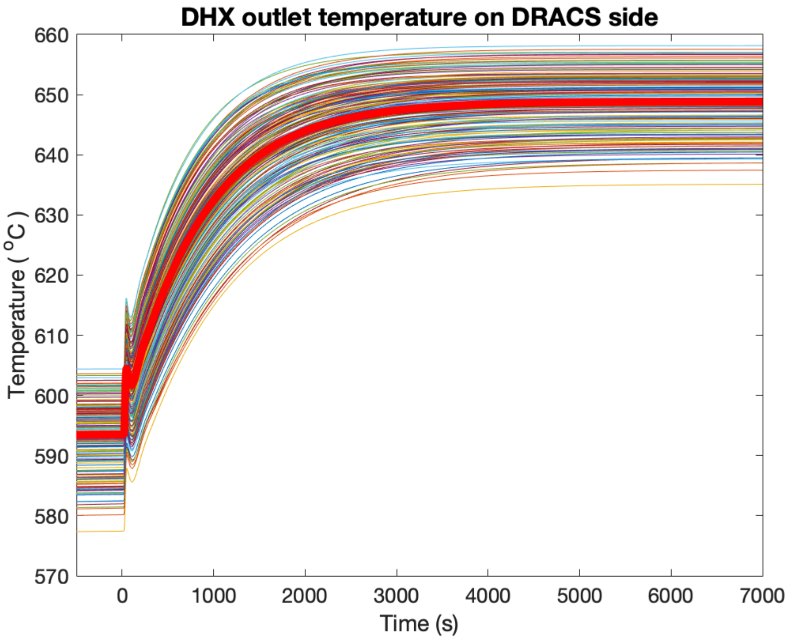

Figure 6-6. DHX outlet temperature on the DRACS side during overpower transient

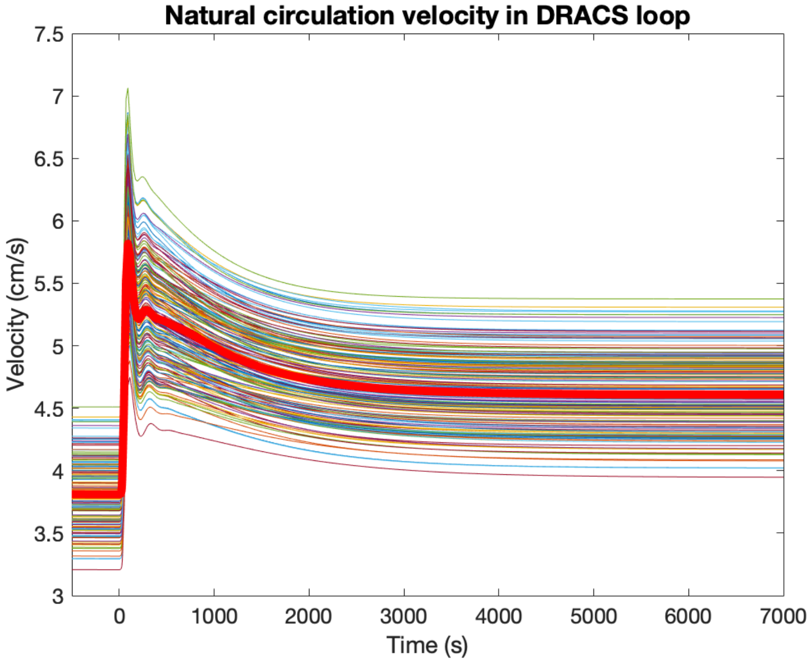

Figure 6-7. Natural circulation velocity in the DRACS loop during overpower transient

To further analyze the distribution of the QoIs, the salt temperature and the natural circulation velocity in the final steady state (7,000 s) of the transient is plotted with the four FLiNaK thermophysical properties in Figure 6-8, Figure 6-9 and Table 6-4. The trends of output value (QoIs) correspond to the value of input variables (FLiNaK thermal properties) are demonstrated in Figure 6-8 and Figure 6-9. Viscosity and thermal conductivity are more correlated to the temperature while heat capacity and density are more scattered. For natural circulation, clear trends are shown with viscosity and heat capacity while thermal conductivity and density are less correlated. In Table 6-4, the standard deviation for the salt temperature and natural circulation velocity in the DRACS loop are 4.8 °C and 0.31 cm/s, respectively.

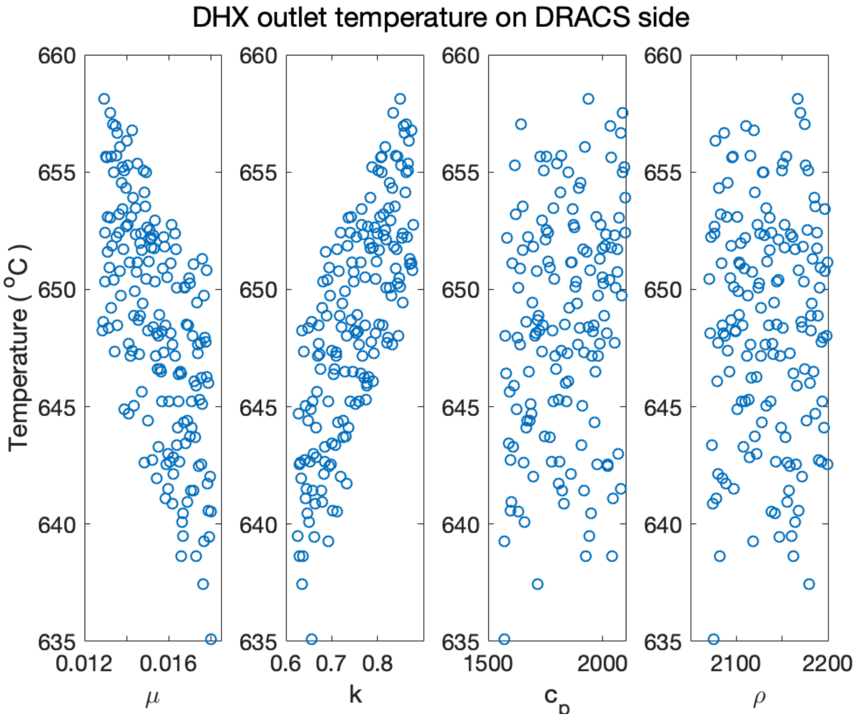

Figure 6-8. Overpower transient steady state results of DHX outlet temperature on the DRACS side

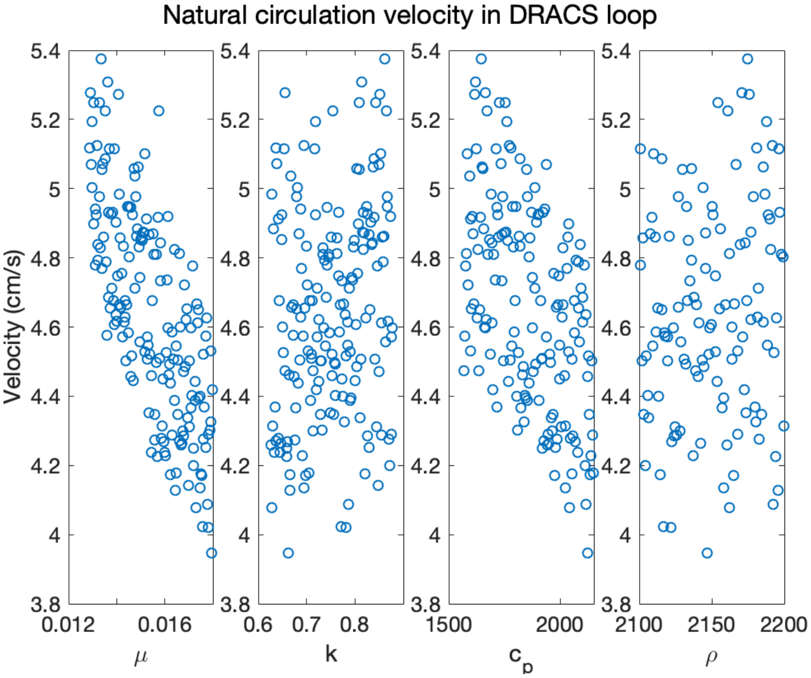

Figure 6-9. Overpower transient steady state results of natural circulation velocity in the DRACS loop

Table 6-4. Overpower transient steady state results

OP transient	Maximum	Mean	Minimum	Standard deviation
DHX inlet temperature on the DRACS side (°C)	658.1	648.5	635.1	4.8
Velocity in the DRACS loop (cm/s)	5.38	4.64	3.95	0.31

6.3 Overcooling (OC) Transient

Before the OC transient starts, the initial conditions of the system are also the same with the OP transient (primary inlet velocity of 2 cm/s, primary inlet temperature 650 °C, air inlet velocity of 10 cm/s and air inlet temperature 27 °C). When OC occurs, the air inlet velocity increases from 10 cm/s to 50 cm/s. The air velocity increase can simulate the air chimney open in FHRs when accidents occur. The DHX inlet temperature is chosen as QoI for the temperature because it is the lowest temperature in the DRACS loop (cooled by air and heat loss along the DRACS cold leg) in OC transient.

Figure 6-10 and Figure 6-11 show the DRACS salt temperature and natural circulation velocity during the transient. The DRACS salt temperature decrease since the cooling performance of NDHX elevated in the air loop. Due to cooling from the air loop enhanced, it increases buoyancy force in the DRACS loop and accordingly the salt natural circulation velocity. Similar to OP transient, the salt temperature and the natural circulation velocity in the final steady state (7,000 s) of OC transient are plotted with the four FLiNaK thermophysical properties in Figure 6-12, Figure

6-13 and Table 6-5. As expected, the trends of FLiNaK salt temperature and velocity with input variables in OC transient are similar to OP transient. The standard deviation for the final steady state of FLiNaK salt temperature and velocity are 10.8 °C and 0.4 cm/s, respectively.

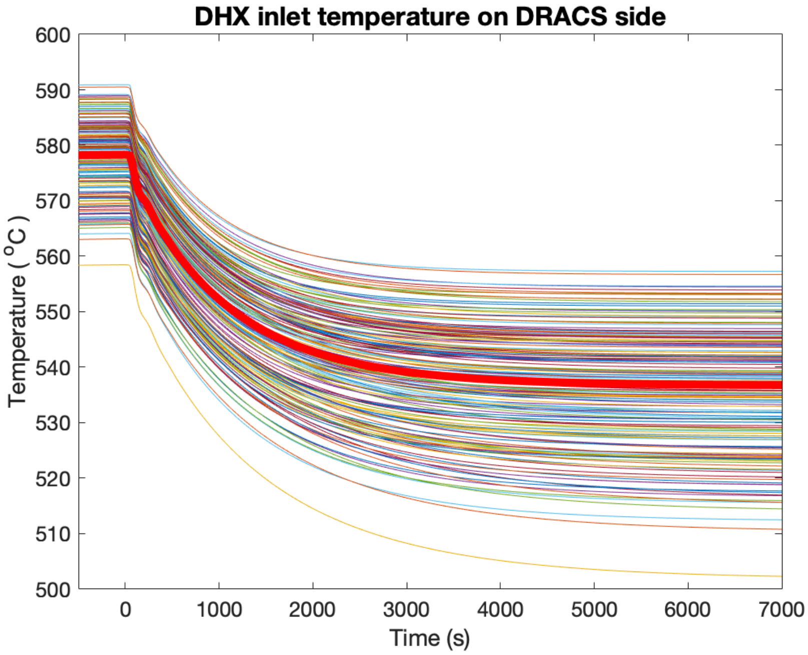

Figure 6-10. DHX inlet temperature on the DRACS side during over cooling transient

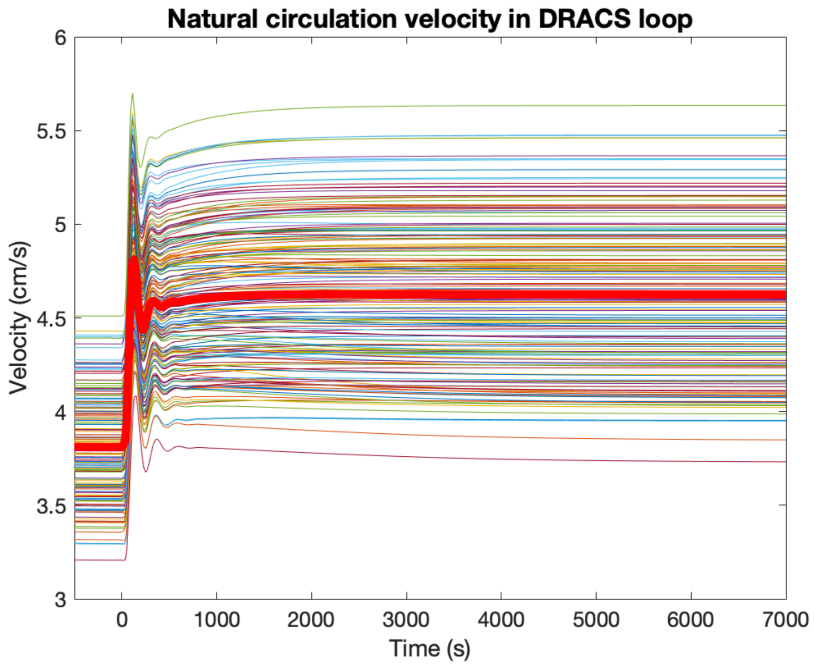

Figure 6-11. Natural circulation velocity in the DRACS loop during over cooling transient

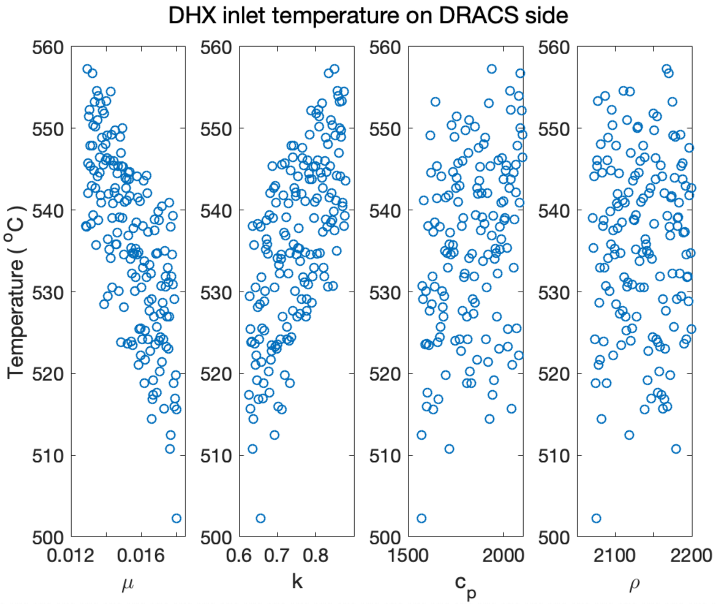

Figure 6-12. Over cooling transient steady state results of DHX inlet temperature on the DRACS side

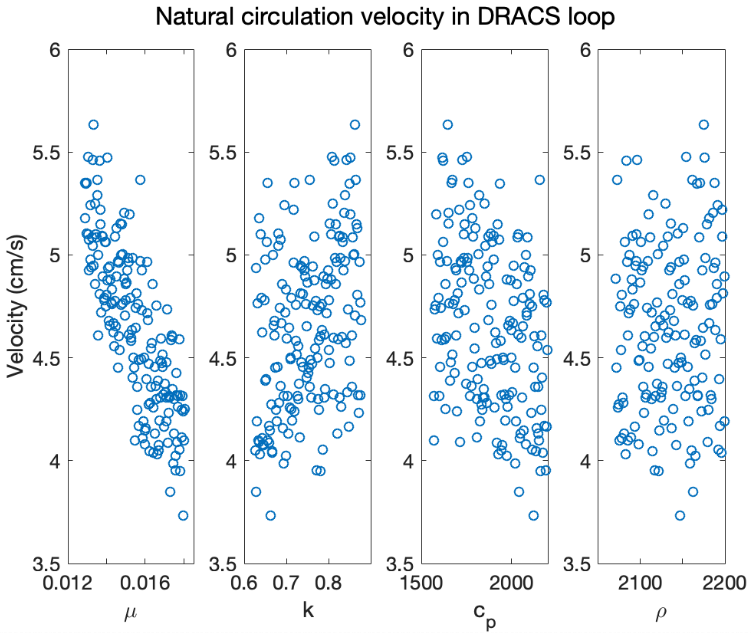

Figure 6-13. Over cooling transient steady state results of natural circulation velocity in the DRACS loop

Table 6-5. Over cooling transient steady state results

OC transient	Maximum	Mean	Minimum	Standard deviation
DHX inlet temperature on DRACS side (°C)	557.3	535.9	502.3	10.8
Velocity in DRACS loop (cm/s)	5.63	4.65	3.73	0.40

6.4 Sensitivity Analysis

The UQ Lab package (Marelli et al., 2014) is used for the surrogate model construction and sensitivity analysis. Multiple statistical methods such as polynomial and Gaussian process that can be utilized for the surrogate model. The Gaussian process (Adler., 1990) is chosen for the surrogate model since it is widely used in data-driven modeling and optimization. Fitrgp function is used in MATLAB to fit a gaussian process regression model. Matern kernel with parameter 5/2 (matern52) is used in the kernel function or covariance function in this model. Due to the observation number is smaller than 2000, so exact Gaussian process regression is chosen in the fitting method. The exact Gaussian process is also used to make predictions from the Gaussian process model based on the prediction number. The surrogate model is built to fit the 175 samples results and then expand to 10^5 samples based on the best-fitted correlation. Sobol indices or the Sobol method (Sobol, 2001) is utilized to perform the sensitivity analysis based on the 10^5 results. This method decomposes the variance of QoIs to investigate the source of contribution to the variance. The index on the y-axis represents the relative contribution of each input variable groups (molten salt thermal properties) to the total variance. The indices can be treated as measures of sensitivity. The first-order Sobol indices represent the index with respect to one input variable alone. Higher-order Sobol indices contain the effect of the interaction of different input variables. The total Sobol indices represent the effect of all orders including interaction with different variables. The first-order sensitivity index is derived as follows:

The equation Y= f(X) shows the model where Y is the output and X_1 to $X_{p.}$ are the input parameters. The X_{-i} notation indicates the set of all variables except X_i. The function of V and E are variance and average, respectively.

$$Y = f(X_1, \dots, X_p) \tag{6.3}$$

$$V_{X_{-i}}(Y|X_i = x_i^*) \tag{6.4}$$

$$E_{X_i}(V_{X_{-i}}(Y|X_i = x_i^*)) \tag{6.5}$$

$$V(Y) = V_{X_i}\left(E_{X_{-i}}(Y|X_i)\right) + E_{X_i}\left(V_{X_{-i}}(Y|X_i)\right) \tag{6.6}$$

$$1 = \frac{V_{X_i}\left(E_{X_{-i}}(Y|X_i)\right)}{V(Y)} + \frac{E_{X_i}\left(V_{X_{-i}}(Y|X_i)\right)}{V(Y)} \tag{6.7}$$

$$S_i = \frac{V_{X_i}\left(E_{X_{-i}}(Y|X_i)\right)}{V(Y)} \tag{6.8}$$

Figure 6-14 shows results of total indices and first-order indices, both plots show very similar values for which demonstrates that the interactions between four input variables are minimal. The uncertainty analysis illustrates that viscosity and thermal conductivity have a dominant effect on the DRACS salt temperatures, while the natural circulation velocity can be impacted more by the viscosity and heat capacity. Also, salt density has less effect on the DRACS salt temperature and natural circulation velocity.

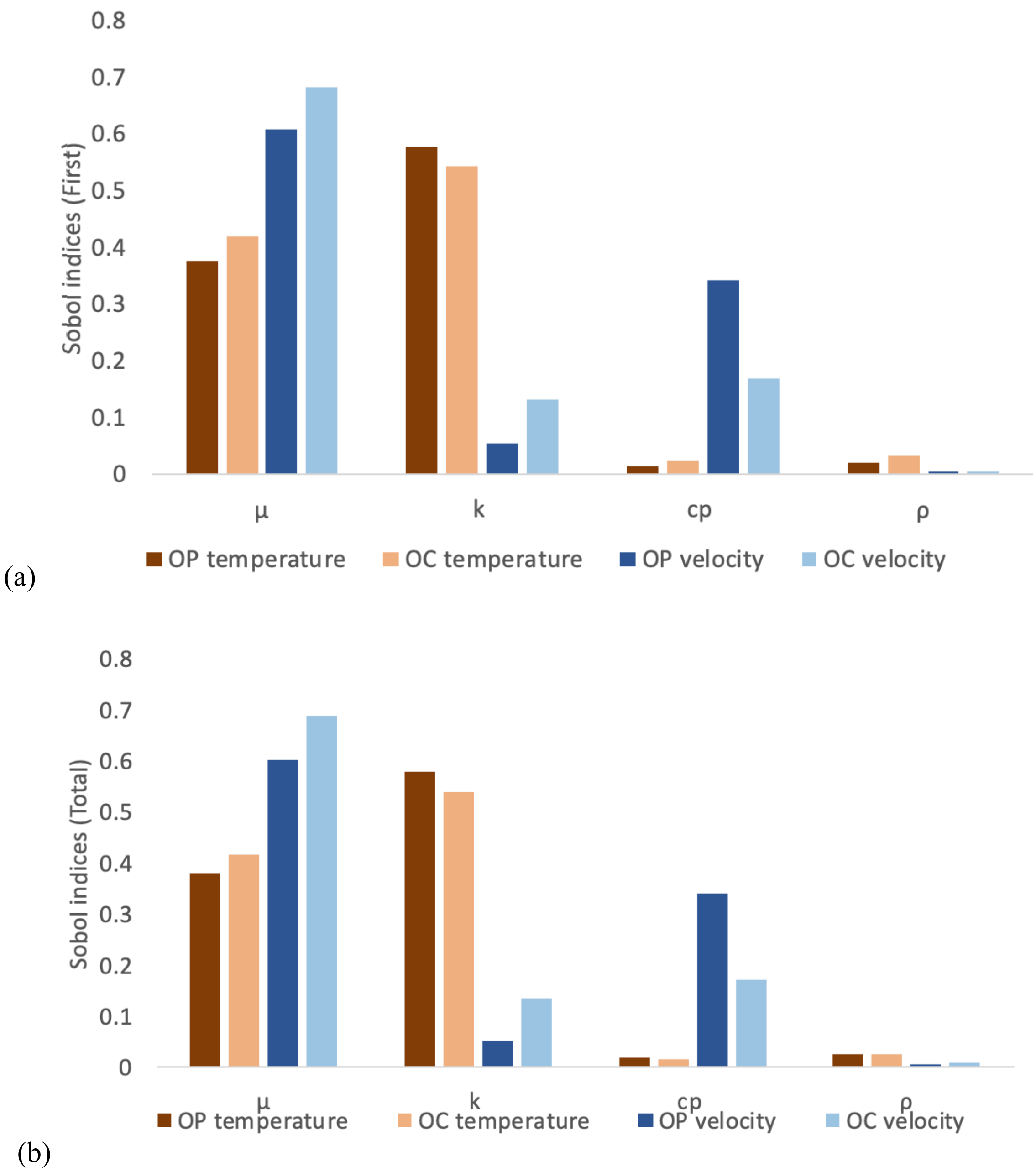

Figure 6-14. (a) First and (b) total Sobol indices for quantities of interests

6.5 Pump Trip Scenario in the HT-FSTF

A pump trip scenario is also analyzed in the HT-FSTF to test the transient response of natural circulation flow in the primary loop and the DRACS loop. The nodalization of the three loops in HT-FSTF is illustrated in Figure 6-15. The coolant of the primary loop is also FLiNaK. The DRACS loop model is the same as Figure 6-4 and the DRACS loop is under natural circulation. In the primary loop, there is a primary pump to provide a driving force of the primary flow and a simulated core to provide a heating source. The core is divided into 40 volumes in the SAM model.

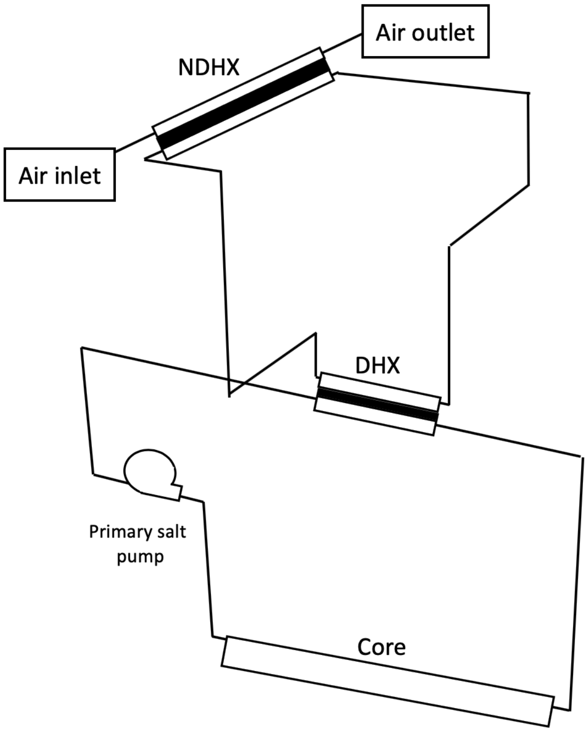

Figure 6-15. Nodalization of HT-FSTF SAM model

For the initial condition, a 1500 W of heating power is provided by the core and the primary pump provides 0.51 kg/s to the primary loop to simulate the steady state of the system under reactor normal operation. The boundary condition of the air loop is controlled with a 5 cm/s air inlet velocity and the air inlet temperature of 127 °C (400 K) as the heat sink of the system. The high air inlet temperature is used to prevent the DRACS loop to be overcooled to freezing during the pump trip transient in the HT-FSTF. The freezing temperature for the FLiNaK is 462 °C which is higher than the $KF\text{-}ZrF_4$ (freeze at 390 °C) in the AHTR design, therefore, it is one of the issues that need to take care with when using FLiNaK as coolants. The pump trip scenario simulation is performed in the HT-FSTF SAM model to predict the transient response of the system under the simulated LOFC event. When the pump trip initiated in the HT-FSTF, the primary pump head linearly decreased to zero in 50 s. Other operating conditions remain the same as the initial conditions.

The simulation results of the HT-FSTF including temperatures and mass flow rates with time are shown in Figure 6-16 to Figure 6-20. In Figure 6-16, the mass flow rate of the primary loop decreases due to the loss of forced flow. A natural circulation flow in the primary loop is formed with the core as a heat source and DHX as the heat sink. There is no flow reversal phenomenon in HT-FSTF based on the design. After the primary pump trip, the natural circulation flow is established within 1,000 s and reaches a stable value. For the DRACS loop, due to smaller primary flow after the pump trip initiation and therefore the heat transfer performance in the DHX shell side becomes lower, the decrease of the natural circulation flow in the DRACS loop can be observed. The mass flow rates of the three loops during the whole transient is are shown in Figure 6-17. For a better display, the air mass flow rate is multiplied by 10 in the figure.

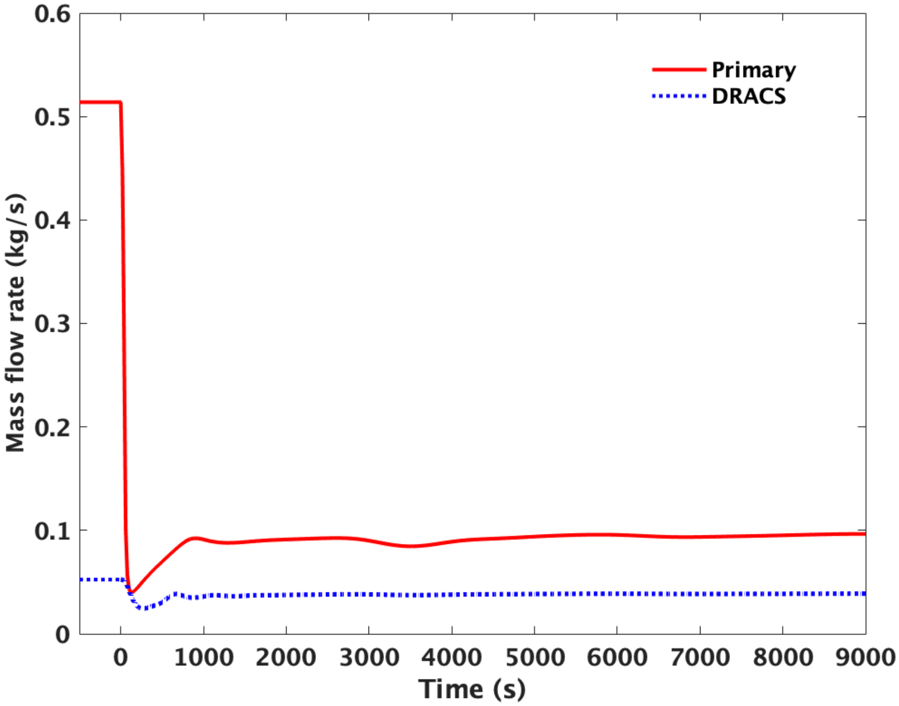

Figure 6-16. Mass flow rates of HT-FSTF during pump trip in a smaller time frame

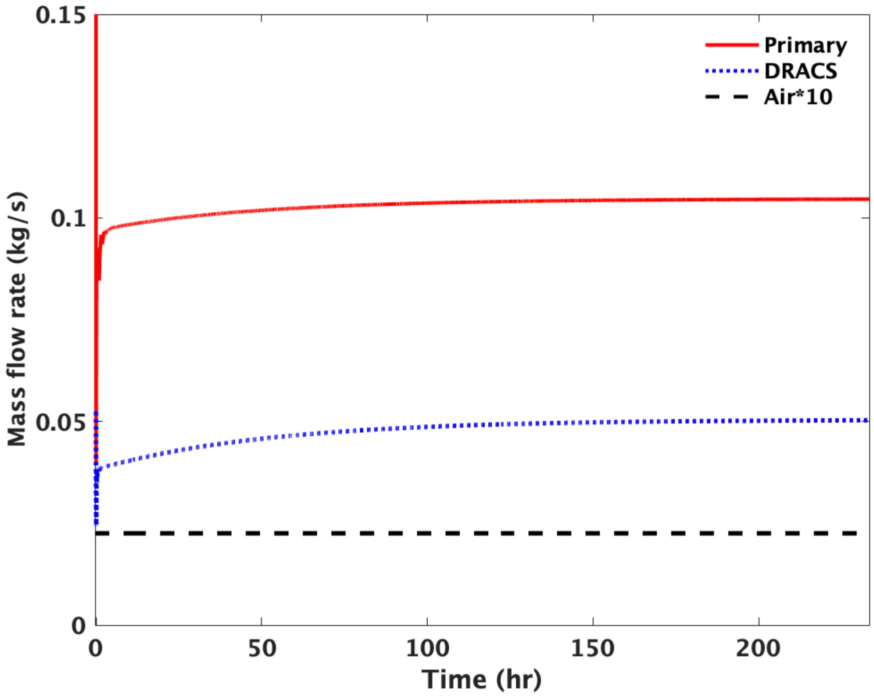

Figure 6-17. Mass flow rates of HT-FSTF during the whole pump trip transient

At the beginning of the pump trip, loss of force flow in the primary loop lower the heat transfer coefficient in the core and consequently generates a temperature drop in the cold leg of the primary loop. After that, the core inlet and outlet temperatures increase after the pump trip since a natural circulation flow is lower than the flow rate in the initial condition. The lower primary mass flow rate of the natural circulation flow decreases the heat transfer coefficient in the DHX shell-side which results in the primary salt temperatures rise with time until a new steady state is reached. Similarly, with the decreased heat transfer performance in the primary loop, while the air cooing condition remains the same, the condition causes the salt temperatures in the DRACS loop and air temperature decrease at the start of the pump trip. Around 4 hours, the coolant temperatures in the DRACS loop and air loop also increase with rising salt temperatures in the primary loop and reach a new steady state.

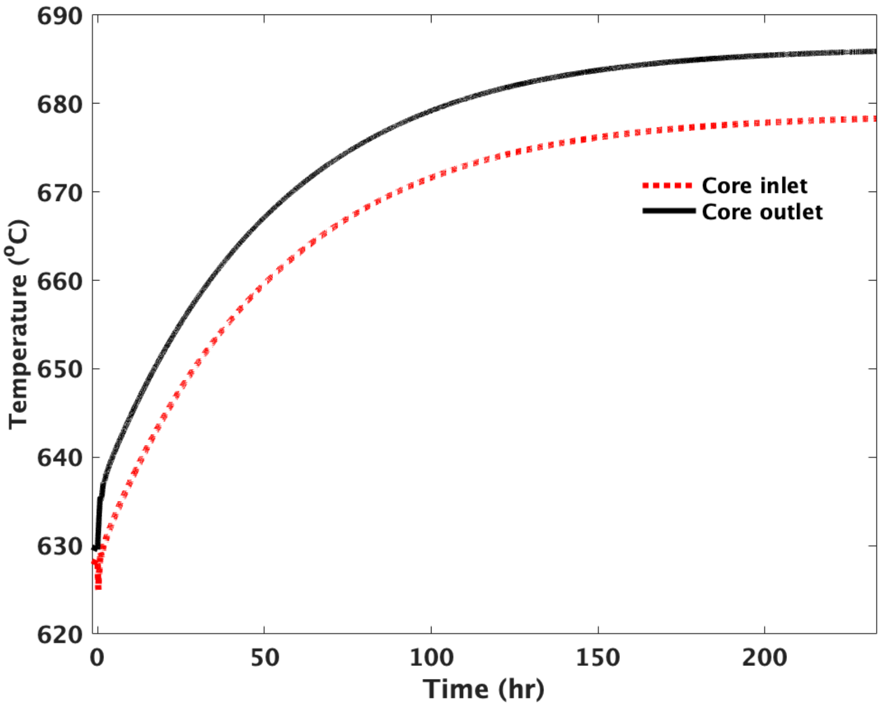

Figure 6-18. Core inlet and outlet temperature of HT-FSTF during pump trip transient

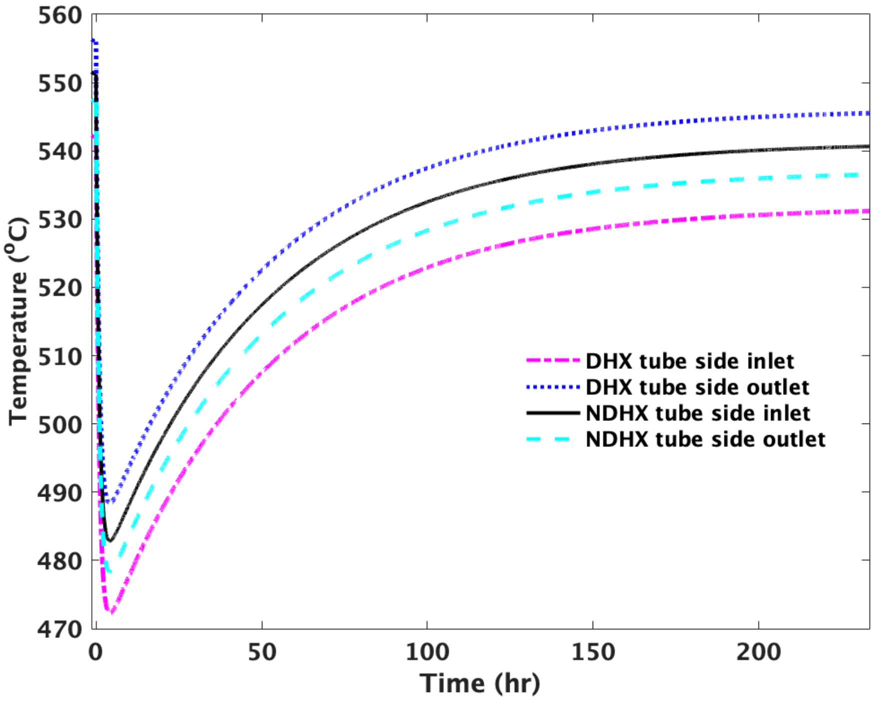

Figure 6-19. DRACS loop temperatures of HT-FSTF during pump trip transient

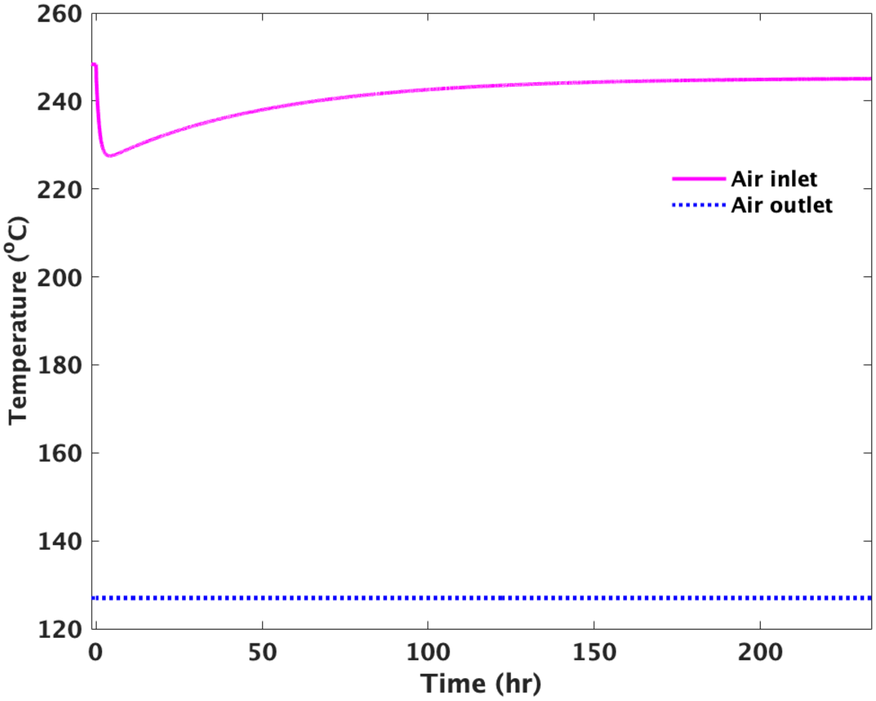

Figure 6-20. Air temperatures of HT-FSTF during pump trip transient

Chapter 7 AHTR Transient Analysis

The RELAP5 code is selected to perform AHTR thermal hydraulics transient analyses because the code validation study discussed in Chapter 4 shows good agreement between the RELAP5 code predictions and experimental data of LTDF. Therefore, molten salt thermodynamic properties and heat transfer correlations for a fluted tube that is proposed for the heat exchanger design in AHTR are implemented into the RELAP5 code. One of the aims of this study is to understand the AHTR response under different scenarios and evaluate the reactor design of AHTR. Consequently, an AHTR RELAP5 model is developed to perform system analysis for two selected transient scenarios, namely SBO and loss of multiple DRACS loops, and to investigate and demonstrate the passive heat removal capability of the proposed fluted-tube DHX and NDHX designs for AHTR.

7.1 RELAP5 AHTR Model

The objective of this chapter is to develop an AHTR model using system-level code that can be used for thermal hydraulics steady-state and transient simulation for evaluating the reactor design and investigate the capability of the passive heat removal system. Therefore, an AHTR model is built in RELAP5/SCDAPSIM/MOD 4.0. Based on the requirement for performing AHTR simulations, thermodynamic and transport properties of FLiBe, FLiNaK, and KF-ZrF4 are implemented into the RELAP5 code. Same with AHTR design, the model includes three primary loops, three intermediate loops, three DRACS loops. For the reactor vessel in the AHTR RELAP5 model, there are four rings to model the fuel assemblies, an upper plenum, and a lower plenum. FLiBe is utilized as the coolant in the primary loops and KF-ZrF4 is the coolant in the three intermediate loops and three DRACS loops. Figure 7-1 shows a schematic of the AHTR RELAP5 model with one primary loop and one DRACS loop displayed only.

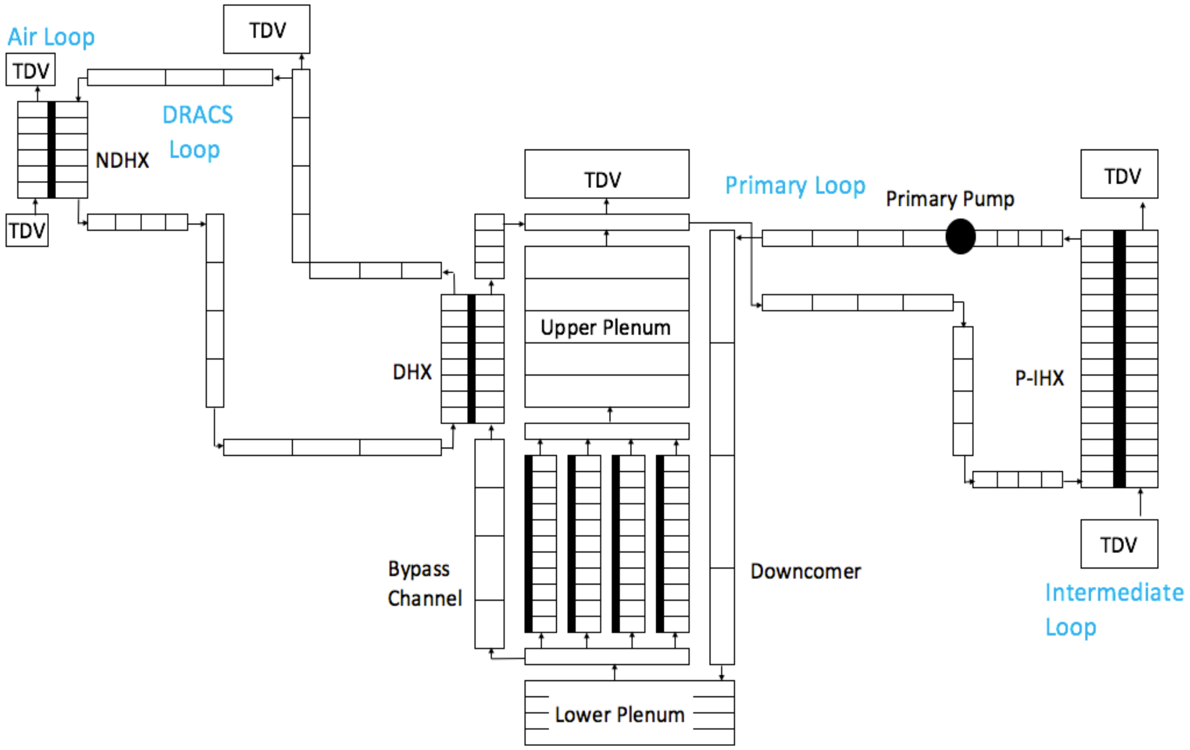

Figure 7-1. Schematic of the AHTR RELAP5 model

For the annular region between core barrel and reactor vessel in AHTR design, it is divided vertically into eight angular regions, three for primary loops, three for DHX primary side (bypass flow), one for maintenance cooling system, and another for the refueling lobe in the AHTR design. In the current AHTR RELAP5 model, the maintenance cooling system and the refueling lobe are not included in the model, only six regions are considered (three for the primary loops and three for the bypass flow).

For the flow direction during reactor normal operation, start from the lower plenum the core flow and three bypass flows merge at top of the upper plenum, and then the merged flow separates into three primary loops. The flow separation point corresponds to the branch in the AHTR RELAP5 model. Primary salt flow through P-IHXs and transfer heat to intermediate loops and then return to the downcomers and lower plenum. Each primary loop has a primary pump to provide a driving force. Three primary flows merged in the branch that connects to the lower plenum. In the AHTR design, the cover gas (argon) in the reactor vessel is utilized to prevent chemical reactions in the primary salt with the surrounding air. A time-dependent volume (TDV) is used to model the cover gas layer above the upper plenum with a constant pressure boundary of atmospheric pressure.

In this AHTR RELAP5 model, there are also three intermediate loops connecting to P-IHXs with KF-ZrF4 as a working fluid. The intermediate loops are simplified as open loops by using two TDVs in each loop to simulate the source and sink of the intermediate fluid. A time-dependent junction (TDJ) is used to control the mass flow rate in each intermediate flow coming from the source TDV.

Other than the primary flow, the other flow paths from the lower plenum to the upper plenum are the three bypass flow. DHX locates at each bypass channel to transfer heat to the DRACS loops. In addition, fluidic diode, a passive flow controller, locates below the DHX in each bypass channel. During reactor normal operation, the upward bypass flows are driven by the primary pumps. If the primary pumps are tripped, the bypass flows will start to reverse since the natural circulations are established with the core as a heat source and DHX as a heat sink. The fluidic diodes provide larger flow resistance for upward flows to decrease heat loss to DRACS loops during reactor normal operation. Also, the small amount of heat from the core to DRACS during normal operation can help to keep the DRACS salt from freezing. However, there is no design value of parasitic heat loss and diodicity of the fluidic diode in AHTR. Therefore, a disc-shaped vortex fluidic diode with a diameter of 304.8 mm is employed in the design. Based on the result of CFD analysis, the form loss coefficients for the upward and downward flow in the fluidic diode are 24.25 and 4.5, respectively.

As shown in Figure 7-1, there are DHX and NDHX in each DRACS loop to transfer heat from core to the ultimate heat sink (ambient air) for the passive heat removal system. In the AHTR design, KF-ZrF4 is used as the coolant in DRACS loops. There is no pump in the DRACS loop since it fully depends on natural circulation/convection to remove the decay heat from the core. For the air loops, two TDVs are used to simulate the source and the sink of the ambient air of the air chimney.

There are four sets of heat structures in the AHTR RELAP5 model, including the four core rings, three P-IHXs, three DHXs, and three NDHXs. In RELAP5, heat structures represent solid materials in the model, which are usually used as heat transfer components with calculations of heat conduction and heat convection. The design values and RELAP5 input data of the heat structures are provided as follows.

7.1.1 Core

An AHTR core consists of 252 fuel assemblies in the reactor core with thermal power 3400 MWth (Varma et al., 2012). In this AHTR RELAP5 model, 252 assemblies are separated into four concentric rings and uniform power distribution is assigned to the fuel assemblies in each ring. The flow area, power, and heat transfer area of the four rings in the AHTR RELAP5 model are summarized in Table 7-1. For the heat structure setting, the right boundary coordinate and left boundary coordinate are 0 and 1.275 cm, respectively. The heat transfer area is calculated based on the wetted surface of the fuel plates.

Table 7-1. Coolant flow areas and the power of four core rings

	Ring 1	**Ring 2**	**Ring 3**	**Ring 4**
Assembly number	18	42	88	104
Flow area (m^2)	0.87	2.02	4.25	5.01
Power (MW)	243	567	1187	1403
Heat transfer area (m^2)	1193.6	2785.1	5835.5	6896.5

7.1.2 P-IHX

A shell-and-tube heat exchanger design is adopted in the AHTR RELAP5 model. There are several design options for the P-IHX since the tube side and shell side can be either on the primary loop or intermediate loops. The other candidate salt, FLiNaK, in the intermediate loops can also be considered as working fluid. It is mentioned that the P-IHX designs are still in the preliminary stage, further study and investigation of the heat exchangers are required (Wang et al., 2015). The design of the primary coolant salt (FLiBe) as the shell side and the intermediate coolant salt (KF-ZrF_4) on the tube side in the P-IHX is chosen for our AHTR RELP5 model. Table 7-2 shows the RELAP5 input data for the P-IHX. Hastelloy N is used to modeling the structure material in the P-IHX, which is the same as the tubes in DHX and NDHX. The left boundary and right boundary in the table correspond to the radius of the tube inner wall and tube outer wall, respectively.

Table 7-2. P-IHX input data of AHTR RELAP5 model

Left boundary coordinate (m)	0.00987
Right boundary coordinate (m)	0.01111
Heat structure mesh number	5
Total Heat transfer area (m^2)	8000.0

7.1.3 DHX and NDHX

Compared to a plain tube, the fluted tube features an increased heat transfer area and increase turbulence flow in the tube. Also, a fluted tube has less pressure drop than the compact heat exchanger. Therefore, the fluted tube design is adopted for DHX and NDHX in this AHTR RELAP5 model. The Non-Dominated Sorting in Genetic Algorithms (NSGA) (Deb et al., 2000) is utilized to optimize the DRACS design based on evaluating the construction cost and heat transfer capabilities. The geometric information is listed in Table 7-3 and Table 7-4, where the definition of parameters can be found below Equation 7.2. Horizontal design for the fluted tubes is adopted since less tube length is needed as compared to the vertical orientation arrangement.

Table 7-3. Specification of single-wall fluted tube DHX

DHX	
Tube arrangement/ tube type	Horizontal triangular/ Fluted tube
Tube material	Hastelloy N
Tube size (mm)	D_{bi} = 10.67, D_{eo} = 16.64, t_w = 0.508, p = 8.23, N_s = 4, L = 3000
Tube number	2100
Number of rows/columns	140/15
Pitch to diameter ratio	1.5
Tube-side fluid and shell-side fluid	KF-ZrF_4/ FLiBe
Heat removal capacity (MW)	8.5
DHX-NDHX vertical height difference (m)	8.15
DRACS loop piping diameter/ length(m)	0.3/56.3
Core-DHX vertical height difference (m)	10

Table 7-4. Specification of single-wall fluted tube NDHX

NDHX	
Tube arrangement/ tube type	Inline horizontal / Fluted tube
Tube material	SS 316H
Tube size (mm)	D_{bi} = 10.67, D_{eo} = 16.64, t_w = 0.508, p = 8.23, N_s = 4, L = 2500
Tube number	2625
Number of rows/columns	25/105
Pitch to diameter ratio	1.5
Tube-side fluid and shell-side fluid	KF-ZrF$_4$ / Air
Heat removal capacity (MW)	8.5
NDHX-chimney vertical height difference (m)	18.3
Chimney inner/outer shell diameter (m)	3.7/4.7

The heat transfer correlations in fluted tubes are also implemented into the RELAP5/SCDAPSIM/MOD4.0 code. In these correlations, the Nusselt number is a function of the Reynolds number, Prandtl number, and fluted tube geometry. Equations 7.1 and 7.2 are heat transfer correlations for the fluted tube with a certain range of the Reynolds number (Srinivasan., 1993). The geometric parameters of the current tube design are listed in Table 7-5.

$$Nu = 0.014Re^{0.842}Pr^{0.4}e^{*-0.067}p^{*-0.293}\theta^{*-0.705} \quad \text{for } Re \leq 5{,}000 \tag{7.1}$$

$$Nu = 0.064Re^{0.773}Pr^{0.4}e^{*-0.242}p^{*-0.108}\theta^{*0.599} \quad \text{for } 5{,}000 \leq Re \leq 82{,}000 \tag{7.2}$$

where the three dimensionless parameters, p^*, e^* and θ^*, in the fluted tube heat transfer correlations represent:

p^* = nondimensional flute pitch (p/D_v)

p = flute pitch (mm)

D_v = volume-based fluted tube diameter (mm)

e^* = nondimensional flute depth (e/D_v)

e = flute depth (mm)

θ^* = nondimensional flute helix angle ($\theta/90$)

θ = flute helix angle ($tan^{-1}(\pi D_v/N_s)$) (deg)

N_s = number of flute starts

Table 7-5. The geometry parameters of fluted tubes in DHX and NDHX

Flute pitch (mm)	0.0082
Nondimensional flute pitch	0.7083
Flute depth (mm)	0.0025
Nondimensional flute depth	0.2132
Flute helix angle (deg)	50.33
Nondimensional flute helix angle	0.5592
Volume-based fluted tube diameter (mm)	0.012

7.2 Steady-State of Reactor Normal Operation with DRACS Air Chimneys Closed

Tritium generation in FHR or AHTR is also one of the challenges for reactor licensing. To eliminate the tritium release into the ambient, the air chimney is considered to be closed during reactor normal operation. The conditions of steady-state are calculated for reactor normal operation in the AHTR RELAP5 model with air chimneys closed. Trip valves locate in the air chimneys are utilized to control the chimney opening.

For the boundary conditions of the model, the reactor core provides 3400 MW thermal power as the AHTR design value. The inlet temperature and total mass flow rates of the three intermediate loops are set as 600 °C and 43,200 kg/s, respectively. The inlet temperatures of the air loops from ambient air is assumed at 30 °C. In Table 7-6, the simulation results of the RELAP5 AHTR model are set to match the design values, including the core inlet temperature, core outlet temperature, and core mass flow rate.

Table 7-6. AHTR design value and RELAP5 simulation results in a steady-state of reactor normal operation (Varma et al., 2012).

	AHTR design value	AHTR RELAP5 model
Thermal power (MWth)	3400	3400
Core mass flow rate (kg/s)	28,500	28,500
Core inlet/outlet temperature (°C)	650/700	650/700
One bypass mass flow rate (kg/s)	N/A	2700
Parasitic heat loss/thermal power (%)	N/A	0.076
Intermediate loop hot/cold leg temperature (°C)	675/600	675/600
Total intermediate loop mass flow rate (kg/s)	43,200	43,200
One DRACS mass flow rate (kg/s)	N/A	53.5
DRACS hot leg/cold leg temperature (°C)	N/A	642/650

7.3 Heat Transfer from Reactor Vessel Wall to Silo in Reactor Normal Operation

To prevent any potential moisture release from the silo wall, it is suggested that the silo wall temperature should not exceed 100 °C that keeping the silo temperature below 80 °C during reactor normal operation mentioned in AHTR safety design (Varma et al., 2012). Therefore, the safety design of heat transfer from the reactor vessel wall to the silo wall has also been performed. In this study, the effect of the thickness of the thermal insulation to the reactor vessel is investigated to ensure the silo temperature. However, it is challenging to justify the boundary condition of the environment. Therefore, the relatively large distance (5 m) is chosen as the cooling boundary with a constant temperature of 30 °C. Figure 7-2 shows a schematic from the primary salt to the environment (soil). A thickness of 20 cm is assumed in this RELAP5 AHTR model. The thermal radiation model is activated between the thermal insulation wall and the guard vessel, and the guard vessel and the silo wall.

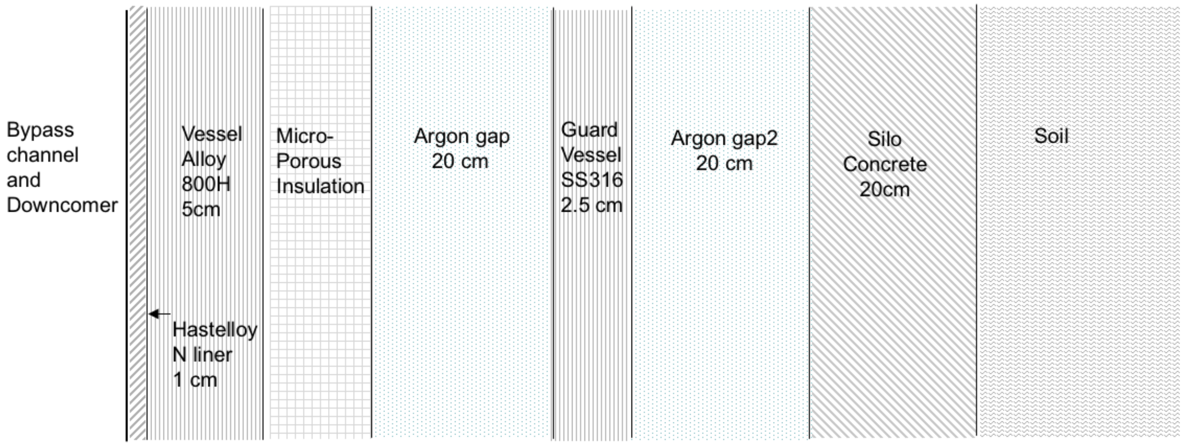

Figure 7-2. Schematic from the primary salt to the environment

Micro-porous insulation is chosen as the thermal insulation material to the outer surface of the vessel wall due to its capability for high temperature conditions. The thickness of the insulation will affect the silo temperature. To keep the silo temperature below 80 °C during reactor normal operation, several thicknesses are tested. Table 7-7 shows the silo wall temperature and the heat loss through the vessel wall during reactor normal operation with different thermal insulation thicknesses. The heat loss is insignificant compared to the full reactor thermal power. The temperature distribution from the vessel wall to the soil surrounding for a 15-cm thick thermal insulation to the reactor vessel wall is shown in Figure 7-3. The thermal insulation provides the largest thermal resistance for the heat transfer process, which limits the temperature rise of the guard vessel and silo wall.

Table 7-7. Steady-state simulation results with different thermal insulation thickness values

Insulation thickness (cm)	**Silo wall temperature (°C)**	**Heat loss to silo wall (MW)**
0	585	1.84
5	104.46	0.24
10	81.78	0.16
15	74.16	0.12

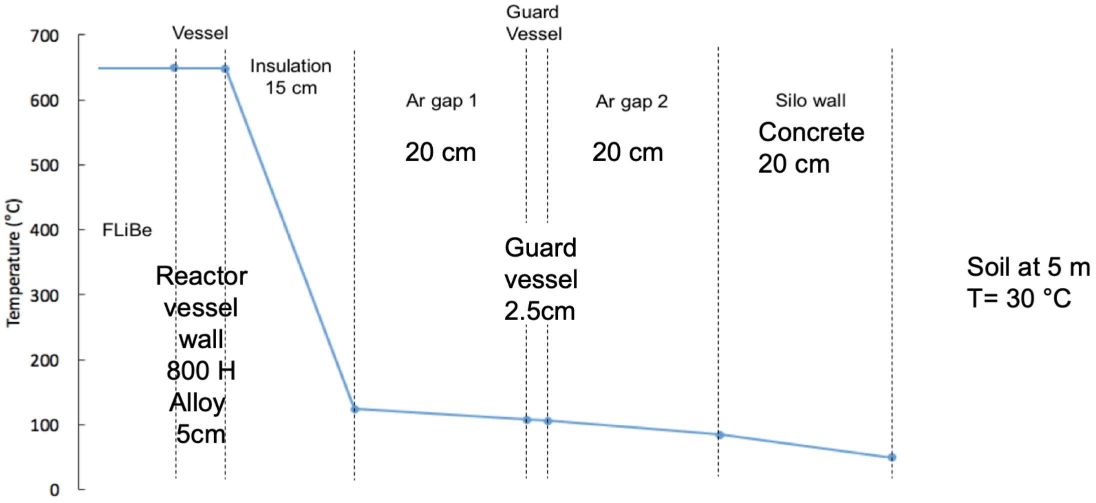

Figure 7-3. The temperature distribution from the vessel wall to the soil surrounding during reactor normal operation

7.4 Station Blackout (SBO)

SBO is identified as one of the most important scenarios in FHR, based on the FHR TH-PIRT study. The performance of decay heat removal in three DRACS loops during SBO is carried out in the AHTR RELAP5 model. Before transient, AHTR is in reactor normal operation, and the air chimneys are closed to reduce the heat loss and lower the tritium release to the environment. The comparison of AHTR design value and RELAP5 simulation results of steady-state conditions in reactor normal operation are listed in Table 7-6. The AHTR RELAP5 model matches the available design value of AHTR, including temperatures and mass flow rates.

When SBO is initiated (0 s), all pumps including the three primary pumps and three intermediate pumps are tripped due to loss of power and assumed to reach fully stop at 100 seconds. The reactor scrams and the three air chimneys are passively opened at 0 s. The decay power curve referenced from the typical pressurized water reactor (PWR) is used to simulate reactor scram in SBO.

For the simulation results, the comparison of the decay power, the heat removal rate of the three primary loops, and the heat removal rate of the three DRACS are shown in Figure 7-4. Due to loss of forced flow, the heat removal rates of the three primary loops drop rapidly after SBO initiation. Though the primary loops lose the forced flow, the result demonstrates the natural circulation is formed in the primary loops and is able to remove a small amount of heat. The decay heat removal rate of three DRACS loops surpasses the reactor decay power at 5 hours after SBO is initiated. It can be observed that the decay heat is mainly removed by the three DRACS loops and the heat removal rate shows fairly stable values during the transient.

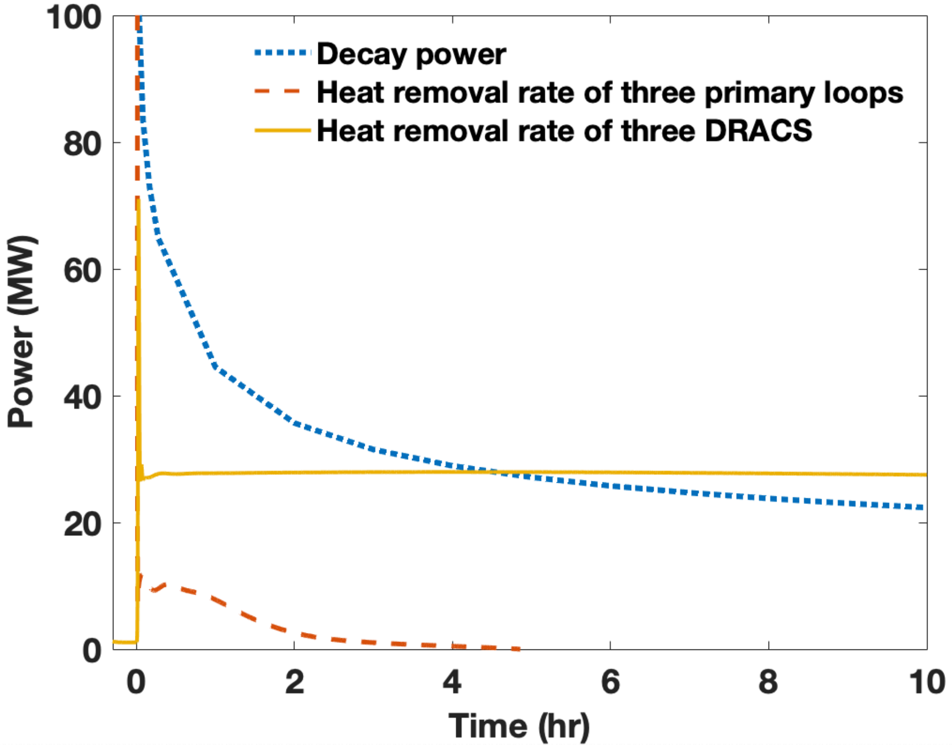

Figure 7-4. Comparison of the decay power, heat removal rate by three primary loops, DRACS heat removal rate of three DRACS loops during SBO.

Before the SBO, the core inlet and outlet temperatures are 650 °C and 700 °C, respectively. In SBO simulation as shown in Figure 7-5, the peak core outlet temperature and maximum fuel temperature during the transient are less than 750 °C, which are hundreds degree lower than the salt boiling (1400 °C) or fuel damage (1600 °C) temperatures (Varma et al., 2012). Alloy 800H has been selected as the AHTR reactor vessel material. To prevent the reactor vessel from salt attack, a Hastelloy N liner in which 1-cm thickness is adopted in the inner surface of the Alloy

800H reactor vessel. Alloy 800H, has been approved in ASME code up to 760 °C (Lommers et al., 2012). Hastelloy N has good resistance to molten fluoride salt corrosion up to 871°C and can be used for continuous operations 982°C. In the current ASME code, the maximum Hastelloy N is codified as 704 °C. However, this value should be revised under the salt environment or for molten salt-cooled design (Ren et al., 2011). The temperature of the core outlet is also below the structure temperatures of the reactor vessel. After around 5 hours, the decay power is lower than the DRACS heat removal rates, which also results in the core inlet and outlet temperatures decrease.

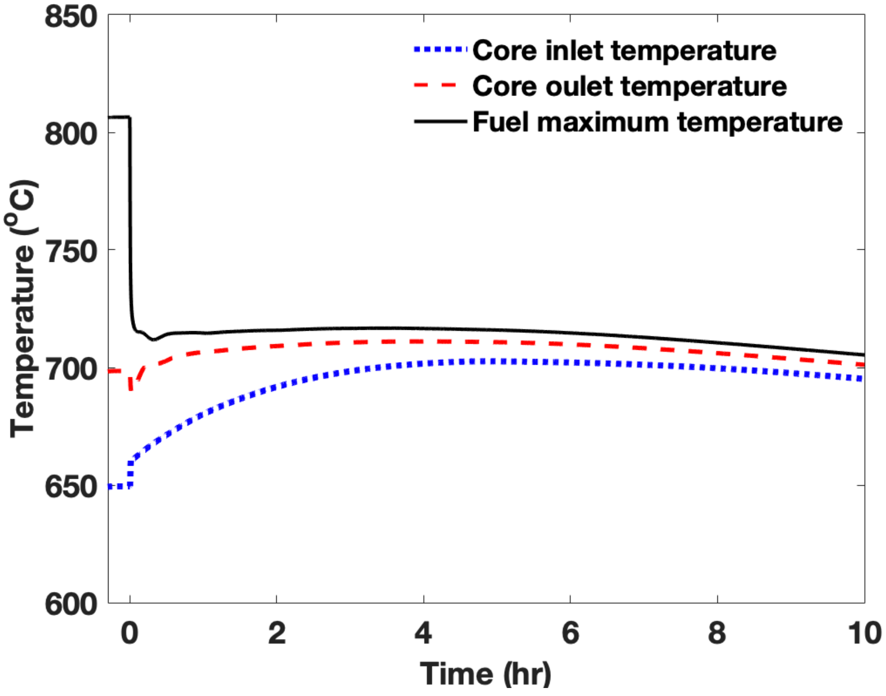

Figure 7-5. Core inlet and core outlet temperature during SBO

The inlet and outlet temperatures of the DHX primary side and the mass flow rate of a single bypass channel are shown in Figure 7-6 and Figure 7-7, respectively. Before SBO, the bypass flow is pumped by the primary pumps from the lower plenum through the fluidic diode and the DHX to the upper plenum. The temperature difference of the DHX inlet and outlet in the bypass side is minimal during normal operation since the air chimney is closed, as shown in Figure 7-6. After losing the forced flow by the primary pumps, the smaller flow resistance in fluidic diodes in the downward flow direction and natural circulation flows formed in the reactor vessel, the bypass flows start to reverse. The reversed flow is indicated by the negative value of the mass flow rate. Figure 7-7 illustrates that the natural circulation in each bypass channel reaches a new equilibrium state of about 400 kg/s at 1,000 s. The flow reversal also results in the temperature increase in the DHX bypass side where the flow comes from the upper plenum which is heated by the core.

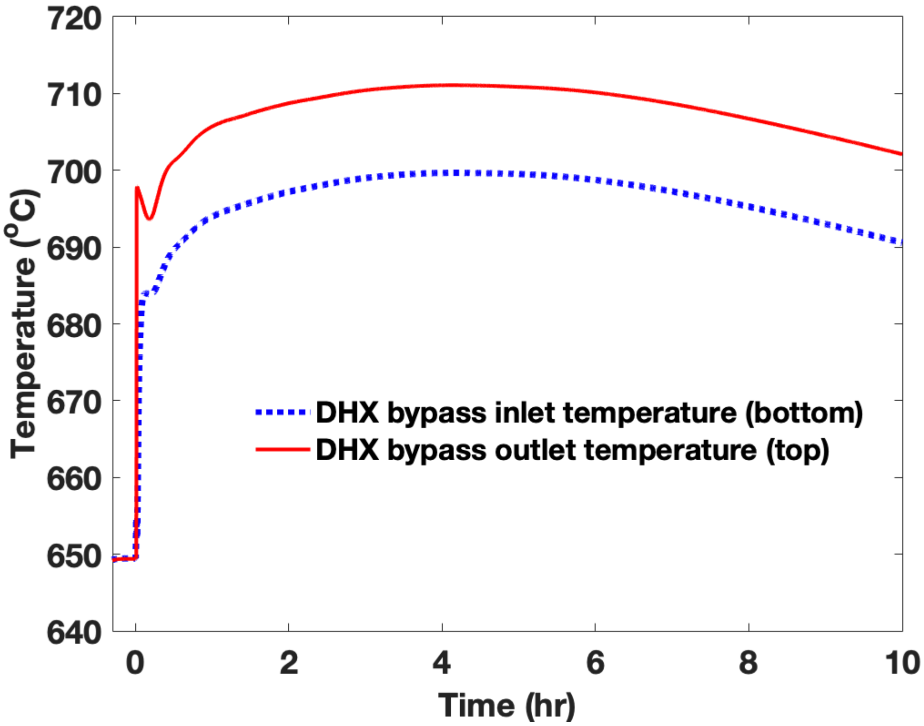

Figure 7-6. DHX inlet and outlet temperatures in bypass channel side during SBO

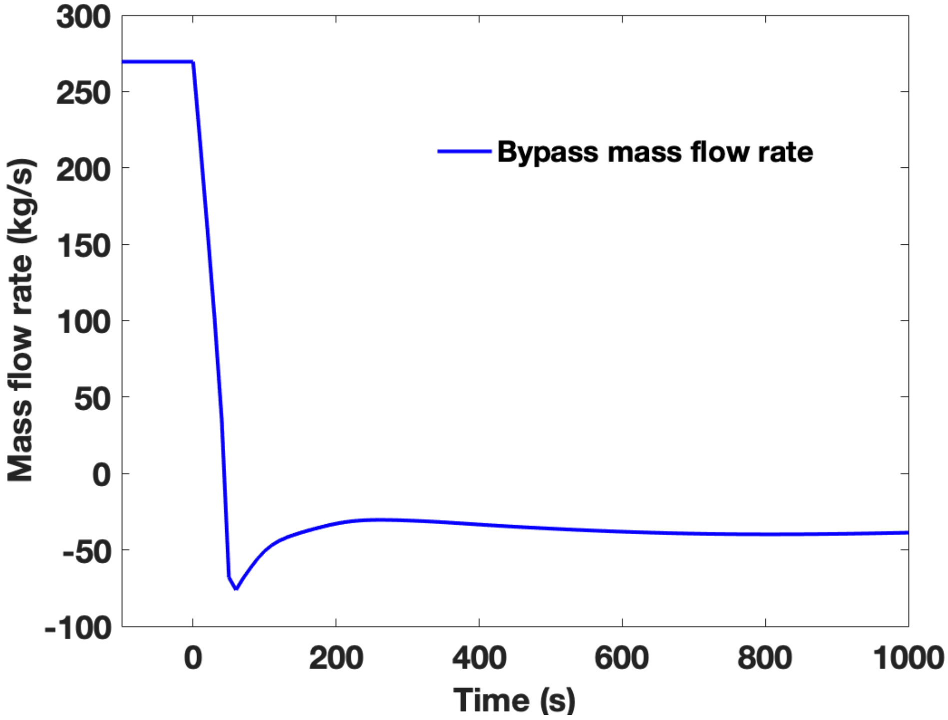

Figure 7-7. Mass flow rates in each bypass channel during SBO (within 1,000 s)

Figure 7-8 demonstrates the DRACS cold leg and hot leg temperatures during SBO. The salt hot leg temperature in the DRACS loop increases during the transient due to the molten salt temperature increase in the DHX bypass side after flow reversal. In addition, the rapid temperature drop in the DRACS cold leg is caused by sudden air cooling. After air chimney is opened in SBO, the large temperature difference between DRACS salt and inlet air (30 °C) in NDHX may result in salt freezing at the cold leg of the DRACS loops. However, the freezing temperature for DRACS salt, KF-ZrF_4 is 390°C, which is not an issue for this SBO analysis. It is still to take care of this issue since the temperature response highly dependent on the reactor design, especially on the heat exchangers.

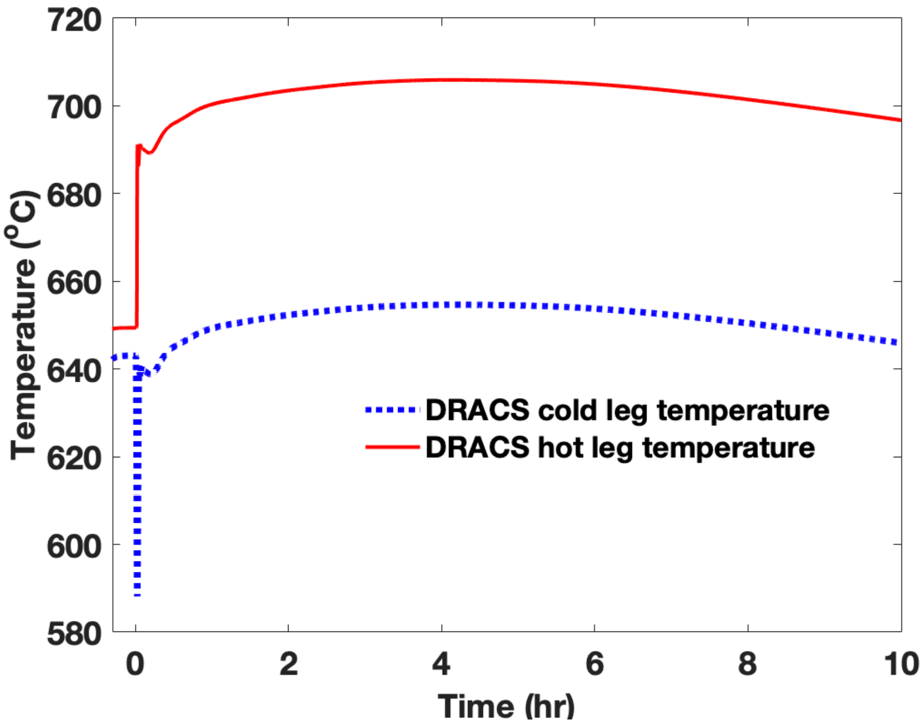

Figure 7-8. DRACS hot-leg and cold-leg temperatures during SBO

The transient responses of DRACS mass flow rates and air mass flow rates are shown in Figure 7-9 from 0 to 2,000 s. After air chimneys are passively opened at 0 s, a natural circulation flow is established in each air loop, and the air flow quickly reaches a stable value. The established natural circulation in each DRACS loop is then followed. At 110 s, the DRACS mass flow rate peak of 232 kg/s is caused by a sudden increase in the primary salt temperature in the bypass channel and increased cooling from the NDHX air side. Based on the RELAP5 simulations results of the SBO scenario in AHTR, it shows that the three DRACS loops with proposed fluted tube DHX and NDHX are capable of removing the decay heat by natural convection. In addition, the temperatures are within the safety limit of structural materials.

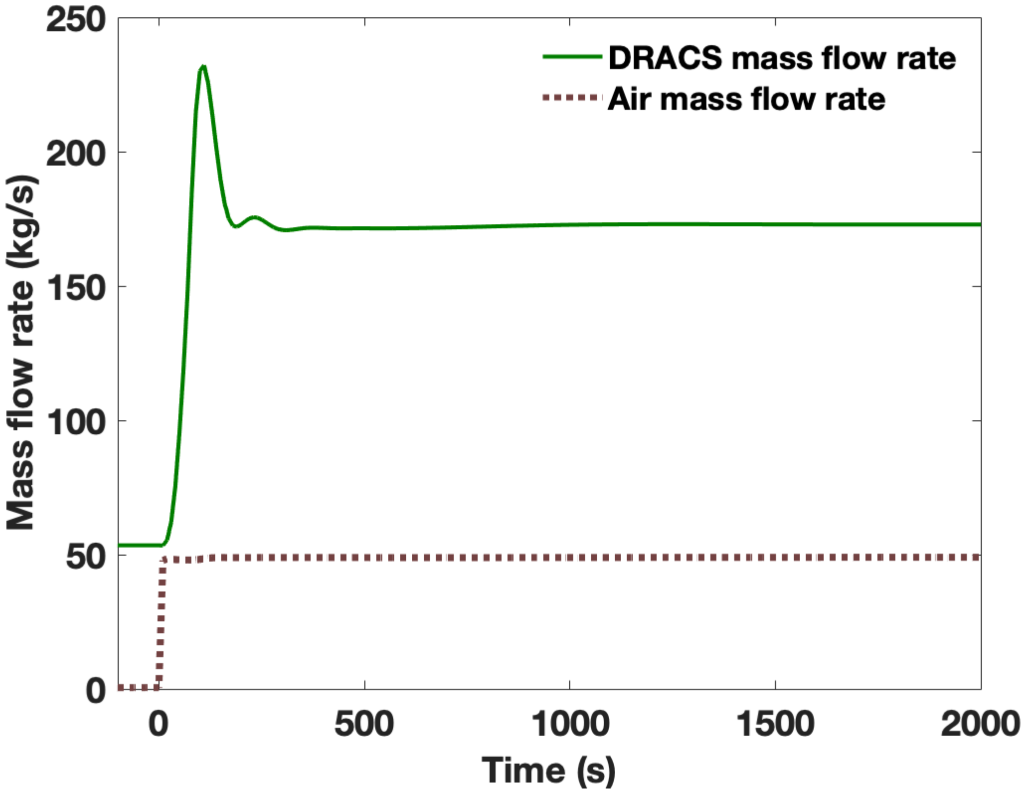

Figure 7-9. Mass flow rates of each DRACS and air loop during SBO (within 2,000 s)

In FHR TH-PIRT, four FOMs are proposed for AHTR during SBO. The simulation results in the RELAP5 AHTR model of these FOMs are as follows:

1. The peak vessel temperature: the Hastelloy N liner inside the reactor vessel should be no more than the core outlet temperature during SBO. The core outlet temperature can be obtained in Figure 7-5.

2. DRACS coolant temperature in the NDHX: Salt freezing is the major concern for this FOM. The temperature is included in Figure 7-8 (DRACS cold leg temperature), which shows the temperature is above the freezing point during SBO.
3. Peak temperature of the DHX: The temperature mainly focuses on the tube temperature since the tube wall is very thin which may affect the integrity of the DHX tube. The bypass side salt temperature is provided in Figure 7-6 which corresponds to the hot side of DHX.
4. Average temperature increase of the carbonaceous materials in the core: See the fuel maximum temperature change in Figure 7-5.

7.5 Simulation of Loss of Two DRACS Loops

During the reactor normal operation, the air chimneys of the three DRACS loops remain closed to minimize the heat losses and any tritium release to the environment. Only one DRACS loop is capable of removing the decay heat when the event of loss of two DRACS loops occurs. Two out of three air chimneys in DRACS failed to open, which results in the ambient air being blocked from the DRACS that losing their designed cooling capabilities. When this scenario is initiated, the reactor is scrammed at 0 s and the primary salt mass flow rates driven by the three primary pumps decrease to 0 kg/s linearly during the first 100 s. Figure 7-10 shows a comparison of the decay power and heat removal rate from DRACS and primary loops. From the simulation results of the loss of two DRACS loops, the open/available DRACS loop is capable of removing about 10 MW decay heat during the transient. The DRACS total heat removal rate shows about 2 MW larger than that provided by the open DRACS loop since the other two closed DRACS loops also can remove 1-MW decay heat each by natural convection and heat conduction. After 50 hours of SBO occurs, the DRACS heat removal rate exceeds the decay power. Figure 7-11 demonstrates the DRACS heat removal in a smaller time frame, and the results show the DRACS heat removal rate increases linearly within the first 2,000 s after the scenario is initiated.

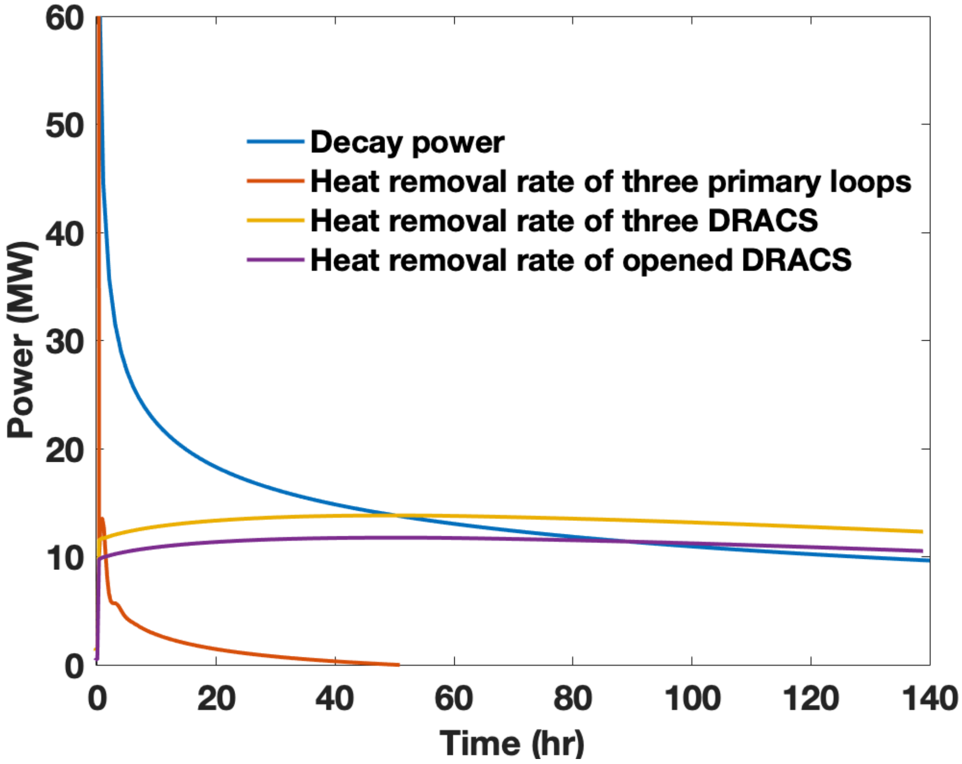

Figure 7-10. Comparison of heat removal rates by DRACS and primary loops, and decay power during loss of two DRACS loops

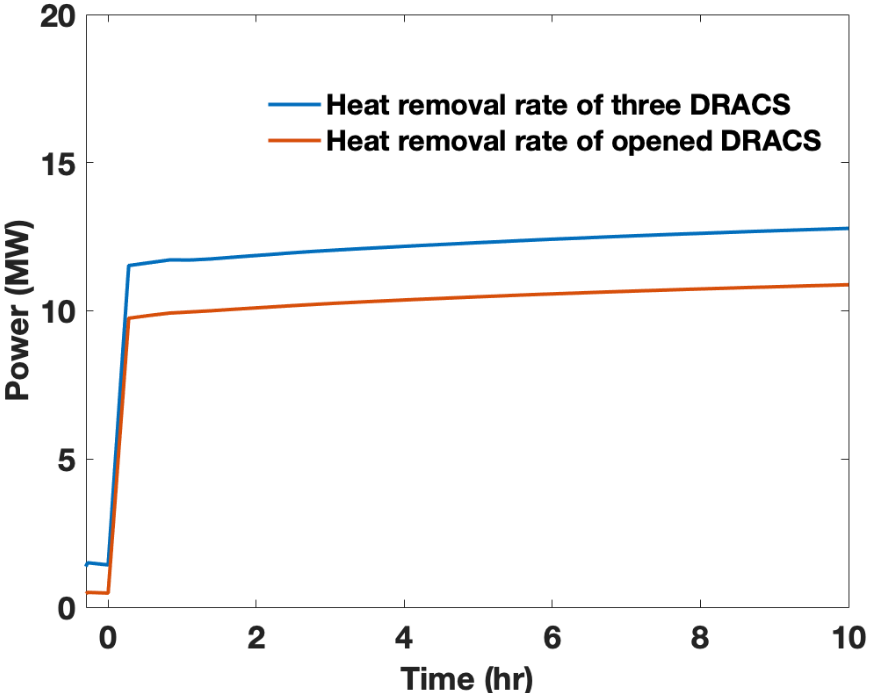

Figure 7-11 Heat removal rates by three DRACS loops and open DRACS loop during loss of two DRACS loops

Figure 7-12 shows the core outlet peak temperature and fuel peak temperature reach 830 °C and 832 °C for about 50 hours into the scenario. Similar to SBO, the maximum fuel temperature is close to the molten salt core outlet temperature since the fuel stripe is fairly thin (25.5 mm) and the fuel can be effectively cooled by the primary molten salt. The core outlet peak temperature is about 130 °C higher than that during the reactor normal operation but is still hundreds degree lower than the molten salt boiling temperature. As mentioned previously, the peak temperature in the primary salt may exceed the structural temperature limit of the reactor vessel, which needs further investigation for the limit temperature of structural material and the reactor design.

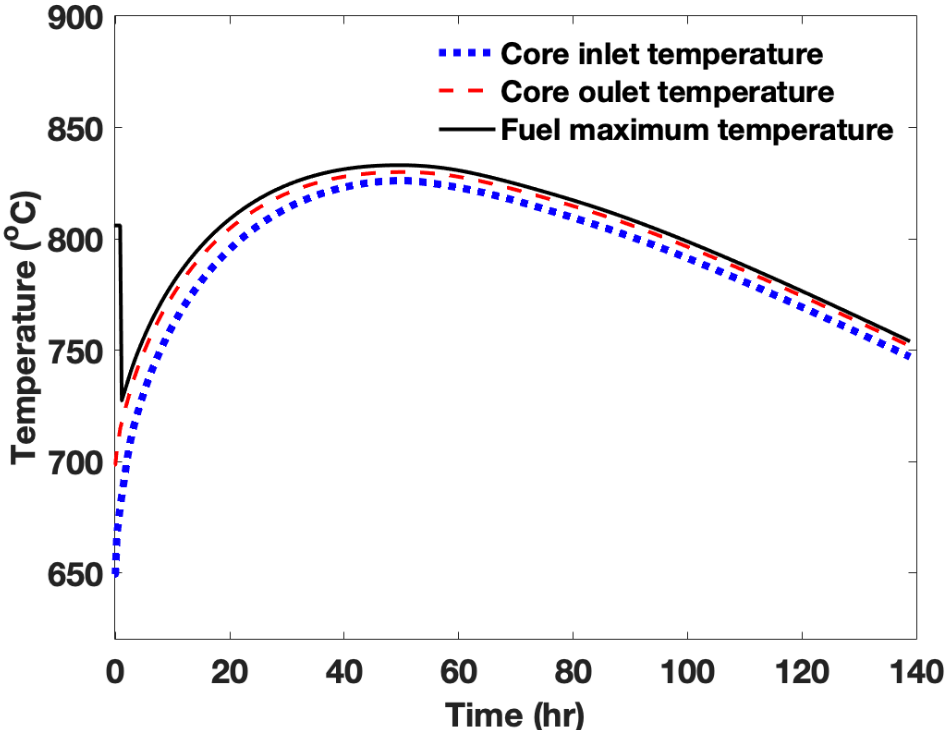

Figure 7-12 Core inlet and core outlet temperature during loss of two DRACS loops

The temperatures on the DHX bypass side and mass flow rates are shown in Figure 7-13 and Figure 7-14, respectively. The flow reversal also occurs in this event as indicated by the negative values of the mass flow rates in Figure 7-13. The higher mass flow rate corresponds to the working DRACS loop (the blue line). The results also show that the salt mass flow rate is about 125 kg/s in the other two closed DRACS loops, which indicates the establishment of natural circulation in the two bypass channels even the heat removal rate is small. For the inlet and outlet temperatures of the DHX bypass flow, the temperature differences are about 10 °C and 55 °C for the closed and opened DRACS loops, respectively.

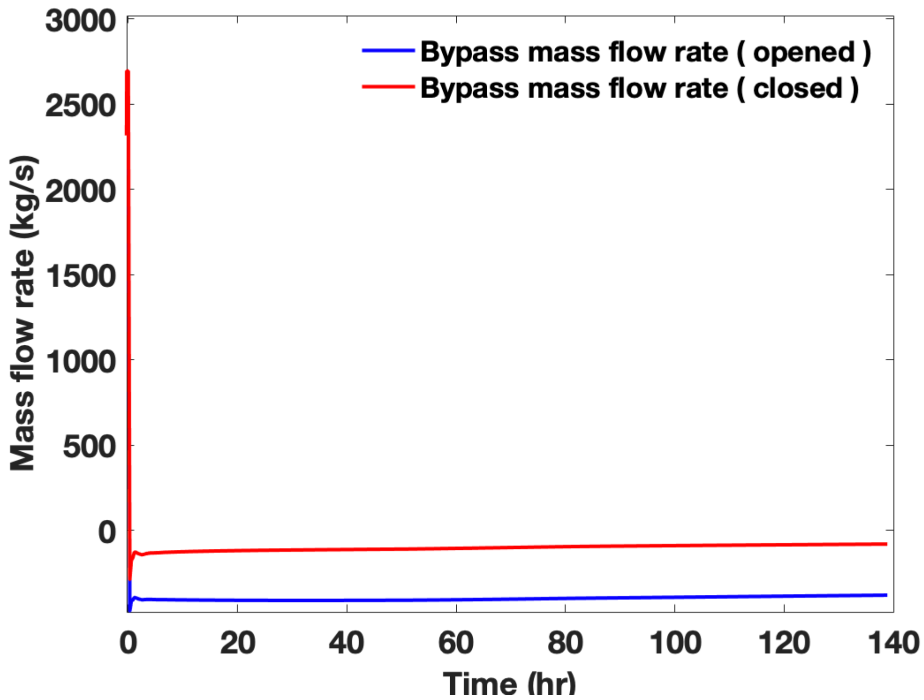

Figure 7-13 Mass flow rates in each bypass during loss of two DRACS loops

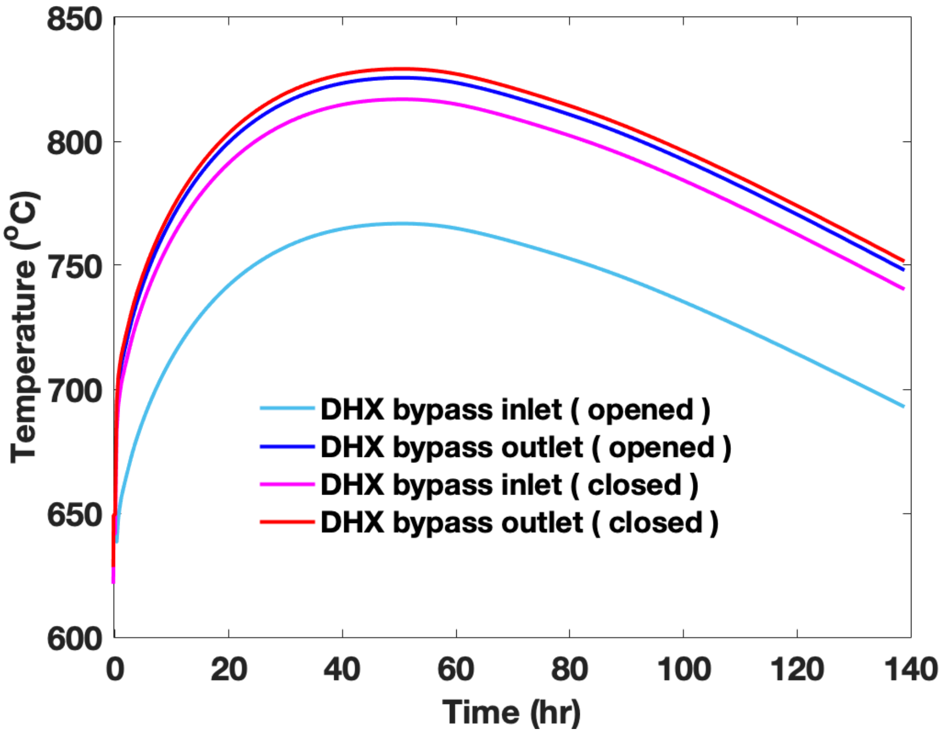

Figure 7-14 DHX inlet and outlet temperatures in bypass channel side during loss of two DRACS loop

The DRACS cold leg and hot leg temperatures are shown in Figure 7-15 and Figure 7-16 in different time scales. After the pump trip and reactor scram, the decay heat removal relies on the cooling of the open DRACS loop. From Figure 7-15, the DRACS temperatures of the closed and open loop hot legs increase almost linearly to above 680 °C in 0.3 hours after the scenario is initiated. In Figure 7-16, the DRACS temperatures slowly decrease with time after about 50 hours. Similar to DHX bypass flow temperatures, the closed DRACS loops have relatively higher temperatures compared with the open DRACS. Due to cooling from the opened air chimney, the DRACS cold leg temperature is about 70 °C lower than its hot leg temperature. The mass flow rate in each of the DRACS loops is shown in Figure 7-17. The results show there is natural circulation flow established in the closed DRACS loops with lower mass flow rates due to the temperature difference between DHX shell-side and NDHX air side.

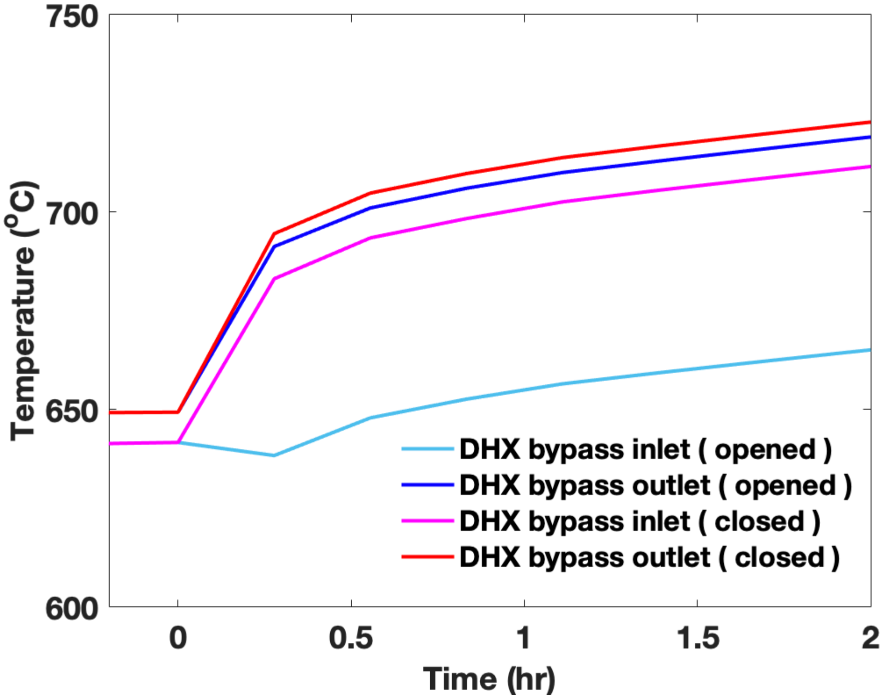

Figure 7-15 DRACS hot-leg and cold-leg temperatures during the first hour of the loss of two DRACS loop scenario

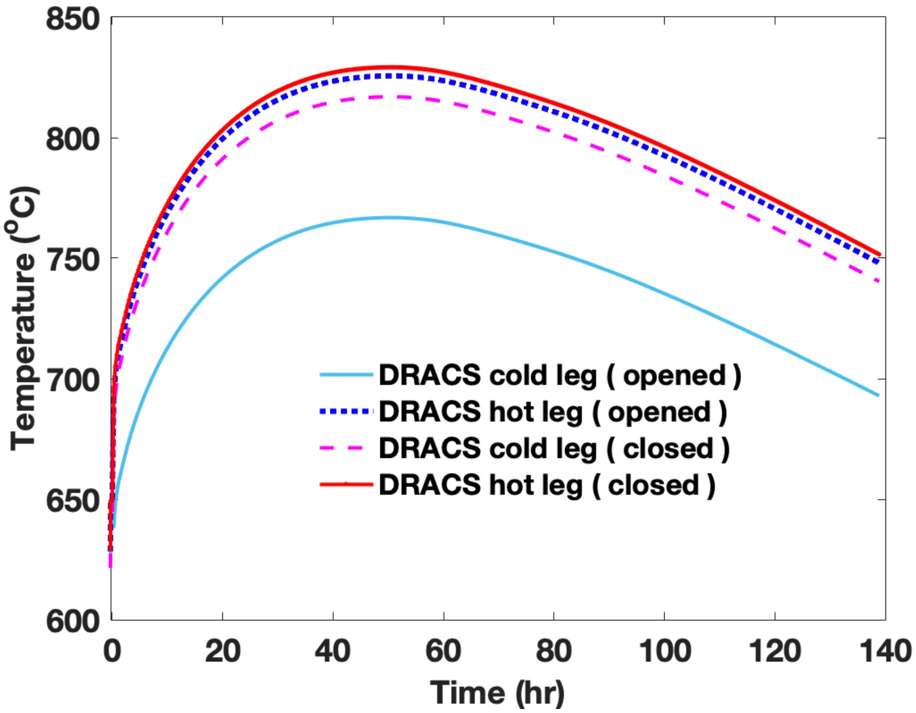

Figure 7-16 DRACS hot-leg and cold-leg temperatures during loss of two DRACS loops

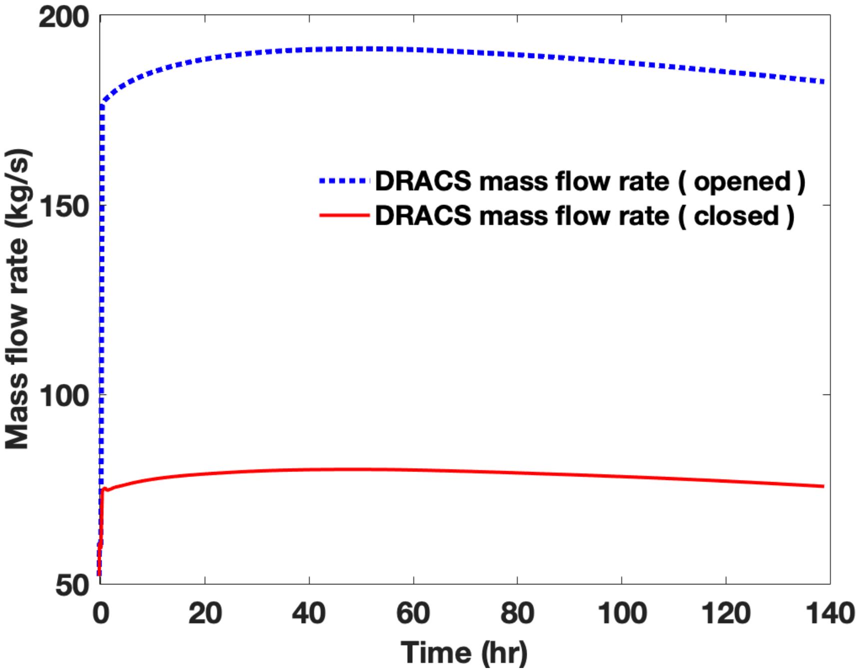

Figure 7-17 Mass flow rates of the DRACS loops during loss of two DRACS loops

Figure 7-18 and Figure 7-19 show the air inlet and outlet temperatures and air mass flow rates. The air inlet temperature is set at a constant temperature of 30 °C as one of the boundary conditions of the system. For the open air chimney, the air outlet temperature increases from 80 to 200 °C. In addition, the rapid increase of the air mass flow rate after the air chimney opens indicates that the natural circulation flow is formed to remove the decay heat from the core to the ambient air.

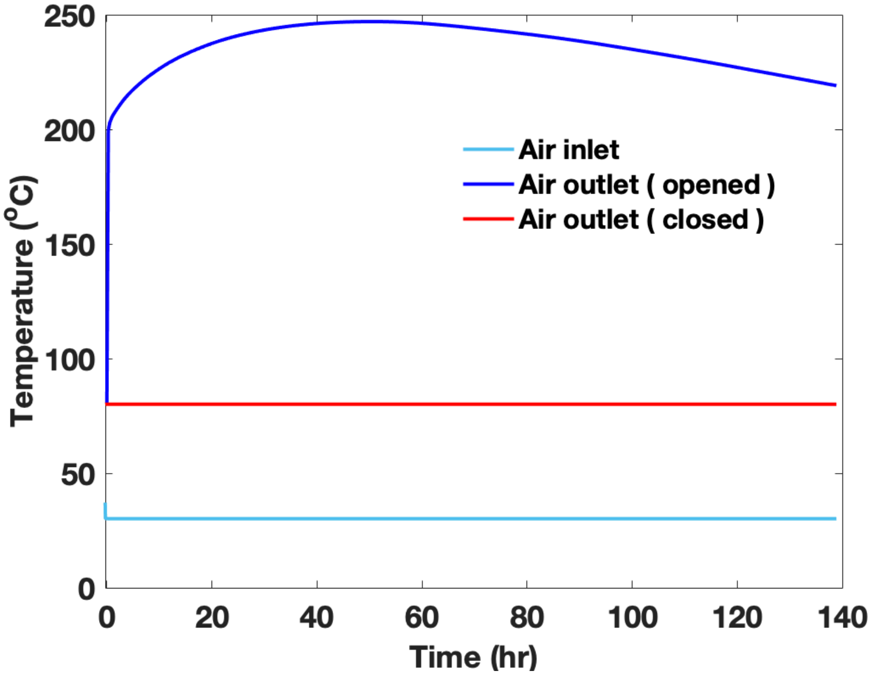

Figure 7-18 Air inlet and outlet temperatures during loss of two DRACS loops

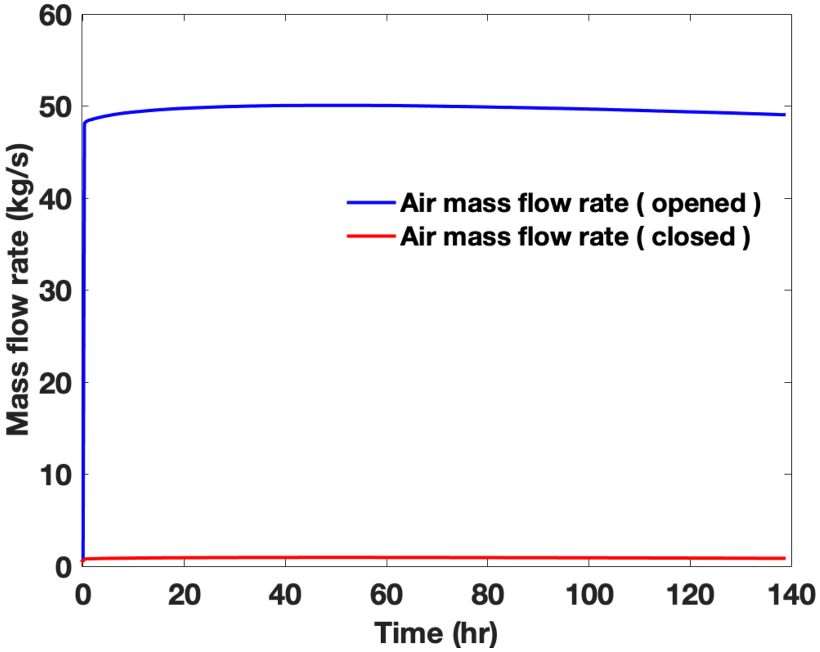

Figure 7-19 Mass flow rates of the air loops during loss of two DRACS loops

Chapter 8 Summary and Conclusions

8.1 Conclusions

In FHR TH-PIRT, it is stated that the code V&V is one of the most important tasks for FHR licensing. FHR TH-PIRT also identified key phenomena that have a high impact on FHRs in various transients and need to be further studied. The principal objective of this research was to demonstrate the code capability and applicability for FHR applications to ensure reactor safety under various transient and accident conditions by system code validation. Several limitations of existing system-level analysis codes are identified in this research, including large uncertainties in liquid fluoride salt thermophysical properties and a lack of accurate heat transfer and friction factor models/correlations for advanced/novel heat exchanger designs.

AHTR is one of the most well-developed FHR pre-conceptual designs. Therefore, this research mainly focuses on the reactor transient analysis of AHTRs, especially on the passive heat removal capability of the DRACS, which fully relies on natural circulation flow/convection to remove the decay heat from the core. Therefore, the system-level code validation in this research uses existing natural circulation flow experimental data in the literature. For the system-level code, RELAP5/SCDAPSIM/MOD 4.0 is chosen for this study due to the flexibility of implementing the thermodynamic properties of molten salts and heat transfer correlations. On the other hand, SAM is also selected since it provides advanced numerical options and has demonstrated successful validation against experimental data related to SFRs.

For code validation on surrogate fluid for molten salt, the experimental data from the single-phase natural circulation test loop at Purdue University and LTDF at OSU are used for the study. From the comparison with the Purdue natural circulation data, the simulation results of RELAP5 and SAM agree well with the experimental data for the parallel-flow arrangement in the source tube bundle. However, for the countercurrent-flow configuration in the source tube bundle, both the SAM and RELAP5 simulation results show larger temperature differences of 3 °C between the inlet and outlet of the source leg than the experimental data. The heat transfer correlations used to model the source leg on the shell side should be the reason for this discrepancy. Three transients of LTDF were performed for code validation, including pump trip with constant power, pump trip with decay power, and startup scenarios. The flow reversal phenomenon and could be clearly captured by the simulation in RELAP5 and the SAM. From the simulation results, the total heat loss in the LTDF is about 7% based on a total power of 2 kW provided in the core when the system reaches a steady state. The computed water temperature differences between the inlet and outlet on the DHX tube side (DRACS loop) is about 3 °C smaller than those in the experimental data in the three transients. Both the experimental and simulation results indicated that although the temperature responses of the entire DRACS system can be affected by daily variations of the ambient air temperature, the overall DRACS thermal performance can still be clearly observed and its functionality confirmed. Overall, the simulation results are in good agreement with the experimental data for both natural circulation and forced circulation flow regimes.

The steady-state experimental data of the FLiBe natural circulation loop at the University of Wisconsin was utilized for the SAM code validation work for the salt loop. It was found that the flow resistance in the loop is under-estimated in the SAM model, which results in higher natural circulation velocity and a smaller temperature gradient along the loop. Based on the uncertainty analysis, there is little effect of uncertainties of FLiBe thermophysical properties on the large flow resistance in the experiment. From CFD analysis, the freezing film in the salt outlet may exist to increase the flow resistance in the loop. Experimental data also identified potential pipe corrosion that affects heat transfer, especially in the heater section. The potential issues of salt freezing and pipe corrosion need to be investigated in further experiments. Further data collection is needed to determine exactly how the two issues affect heat transfer and flow resistance in the loop. This research demonstrated the challenges in molten salt modeling and experimental facilities.

For molten salt code validation, the uncertainties of molten salt thermophysical properties are identified as one of the challenges. Therefore, uncertainty analyses of a molten salt loop on HT-FSTF were performed. The results of the uncertainty analysis show that molten salt thermophysical properties contribute to a large degree on the molten salt temperatures and natural circulation velocity. The standard deviations of DRACS salt temperatures are 4.8 °C and 10.8 °C in overpower transient and overcooling transient respectively. The standard deviations of DRACS salt natural circulation velocities are 0.3 cm/s and 0.4 cm/s in overpower and overcooling transient. From sensitivity analysis of both transients in HT-FSTF, viscosity and thermal conductivity have a higher influence on molten salt temperatures while natural circulation velocities can be affected mainly by viscosity and heat capacity. The pump trip scenario of HT-FSTF is also performed to predict the transient response of the system during a loss of forced circulation.

Based on the good code validation results, the two system codes strengthen the confidence for performing safety analysis on FHRs/AHTRs. Consequently, an AHTR model has been developed using RELAP5/SCDAPSIM/MOD 4.0 for evaluating the proposed DRACS design and reactor response of AHTRs under various transient scenarios. Three primary loops and three DRACS loops are included in this AHTR RELAP5 model. In addition, the design parameters of the fluted-tube DHX and NDHX proposed for AHTR based on their enhanced heat transfer capability are used in the RELAP5 model. The heat transfer correlations for fluted tubes are also implemented into the code. System analyses for two transient scenarios – namely, SBO and the loss of two DRACS loops out of the three loops – are performed. For the SBO scenario, the RELAP5 simulation indicates that an AHTR provides sufficient decay heat removal capability, which leads to sufficient temperature margins from fuel damage and salt boiling. The vessel structural temperatures are also lower than the limit temperature during the whole transient. The decay heat removal rate from the three DRACS loops would exceed the decay heat generation rate in about five hours from the transient initiation. The primary flow reversal in the DRACS systems can be observed in the simulation after the primary pump trip and the natural circulation flows in the primary loops, DRACS loops, and air loops are established within 500 s. After air chimneys are passively opened, the DRACS loop cold leg temperature decreases significantly, which may cause local salt freezing due to the large temperature difference between the incoming air and DRACS salt. This may need additional studies. For the scenario of the loss of two DRACS loops out of three loops, the simulation results indicate that the only available DRACS loop is capable of removing the decay heat at a rate of 10 MW, which would surpass the decay heat generation rate at about 50 hours after reactor scram. The simulation results of both scenarios demonstrate the fluted tube designs of DHX and NDHX for AHTRs can effectively remove the decay heat from the reactor core in the two transient scenarios.

8.2 Main Contributions

In this section, the four objectives and how they are accomplished are summarized as follows:

(1) Understand the capabilities of existing analysis codes, with necessary modifications, for FHR applications: the code validation study demonstrates that both codes can establish credibility in predicting natural circulation flow and fluid temperatures based on several cases of code validation. The good agreements between RELAP5 and the SAM simulations and the experimental data for surrogate fluid tests provide verification of the modeling approach for natural circulation flow.

(2) Identify additional modifications and improvements needed: The code validation against the FLiBe natural circulation loop shows that there is potential for freezing film to exist in the loop. The current 1-D simulation codes are not able to model a freezing phenomenon in the cold spot. Therefore, the research also identifies the freezing model as an additional need in modeling FHRs with current system codes, such as RELAP5 and the SAM. Additionally, the uncertainty of molten salt should be considered in molten salt loop FHR analyses since it significantly influences the output results, including fluid temperatures and natural circulation flow rate.

(3) Enhance, with the improved code capabilities, understanding of the reactor response under different transient and accident scenarios in FHRs and (4) inform and improve FHR reactor designs: Molten salt thermophysical properties and heat transfer correlations were implemented in RELAP5 for modeling FHRs. From the RELAP5 simulation results of the two transient scenarios, DRACS can effectively remove the decay heat from the reactor core to ambient air with the proposed DHX and NDHX designs.

8.3 Future Works

Significant effort will still be required for FHR code validation. Therefore, some of the future work that needs to be performed are suggested.

1. Code validation against FLiBe natural circulation loops has been performed. However, due to potential salt freezing and pipe corrosion issues, flow resistance is under-predicted in the SAM model. Additional code validation is needed to confirm the credibility of system codes in modeling molten salt data.

2. Most of the heat transfer and pressure drop correlations of novel-designed heat exchangers were developed using non-molten salts as the working fluids. The heat transfer correlations should be tested using molten salt as a coolant and further compared with other heat transfer correlations developed under different fluids. For example, the HT-FSTF will test fluted tube heat exchangers to determine if the heat

transfer correlations should be updated or not compared to the fluted heat transfer correlations tested by water.

3. The predicted pump trip results of the HT-FSTF were carried out in this research. However, the code validation should have been conducted once the experimental data become available, including steady state and transient scenarios.

4. Compare to current LWRs, FHRs features high operating temperatures and very high boiling temperatures. However, freezing is a potential issue if molten salt loops are over-cooled. Most system codes were developed for modeling LWRs; therefore, the salt freezing model is not available in these codes. Therefore, the molten salt freezing model is recommended to be implemented into system codes to model over-cooled scenarios.

5. More transient scenarios could be investigated, such as simultaneous withdrawal of all control rods, reactor core partial flow blockage, and loss of coolant accidents (LOCAs). These scenarios are identified as events that significantly affect the safety of AHTRs in FHR TH-PIRTs. To better understand the system behavior and transient response of AHTRs/FHRs, thermal hydraulics system-level codes coupled with other neutronics or CFD codes may be necessary to model some of the events.

6. Tritium control, radiation heat transfer, neutron kinetics and reactivity feedbacks during transients, fuel development, and qualification, structural alloy

development, the adequacy of models and reactor design are the remain topics that still needed to be addressed for FHR licensing. Thermal hydraulics system-level codes coupled with other codes or models are also needed to perform analyses on these topics.

Bibliography

Abrams, B., S. Levy, and D. Chapin, "A Technology Roadmap for Generation IV Nuclear Energy Systems," In U.S. DOE Nuclear Energy Research Advisory Committee and the Generation IV International Forum, (2002).

Adler, R., "An introduction to continuity, extrema, and related topics for general Gaussian processes," Institute of Mathematical Statistics. 12, i–155, (1990).

Andreades, C., A. T. Cisneros, J. K. Choi, A. YK Chong, M. Fratoni, S. Hong, L. R. Huddar et al, "Design Summary of the Mark-I Pebble-Bed, Fluoride Salt–Cooled, High-Temperature Reactor Commercial Power Plant," *Nuclear Technology*, **195**, no. 3, pp. 223-238, (2016).

Ball, S.J., Corradini, M., Fisher, S.E., Gauntt, R., Geffraye, G., Gehin, J.C., Hassan, Y., Moses, D.L., Renier, J.P., Schultz, R. and Wei, T., "Next Generation Nuclear Plant Phenomena Identification and Ranking Tables (PIRTs) Vol. 2: Accident and Thermal Fluids Analysis PIRTs," ORNL/TM-2007/147, Oak Ridge National Laboratory, (2008).

Bettis, E. S., W. B. Cottrell, E. R. Mann, J. L. Meem, and G. D. Whitman, "The aircraft reactor experiment—operation," *Nuclear Science and Engineering*, **2**, no. 6, pp. 841-853, (1957).

Bettis, E. S., and C. R. Roy, "The design and performance features of a single-fluid molten-salt breeder reactor," *Nuclear applications and technology*, **8**, no. 2, pp. 190-207, (1970).

Briggs, D., E. Young, E, "Convection Heat Transfer and Pressure Drop of Air Flowing across Triangular Pitch Banks of Finned Tubes," Chem. Eng. Prog. Symp. Ser, 59 (41), pp. 1–10, (1963).

Britsch, K., M. Anderson, P. Brooks, and K. Sridharan, "Natural circulation FLiBe loop overview," International Journal of Heat and Mass Transfer,134, pp. 970-983, (2019).

Brooks, A., and T. Hughes, "Streamline Upwind/Petrov-Galerkin Formulations for Convection Dominated Flows with Particular Emphasis on the Incompressible Navier-Stokes Equations," *Computer Methods in Applied Mechanics and Engineering*, **32**, pp. 199-259, (1982).

Brown, N. R., B. R. Betzler, J. J. Carbajo, A. J. Wysocki, M. S. Greenwood, C. Gentry, and A. L. Qualls, "Preconceptual design of a fluoride high temperature salt-cooled engineering demonstration reactor: Core design and safety analysis," *Annals of Nuclear Energy*, **103**, pp. 49-59, (2017).

Chen, M., X. Sun, R. Christensen, S. Shi, I. Skavdahl, V. Utgikar, and P. Sabharwall, "Design and testing of helically coiled fluted tube heat exchangers for FHR applications," In: 11th International Topical Meeting on Nuclear Reactor Thermal Hydraulics, Gyeongju, South Korea, Oct 9–13, (2016).

Chen, M., I.H. Kim, X. Sun, R. Christensen, V. Utgikar, P. Sabharwall, P, "Transient analysis of an FHR coupled to a helium Brayton power cycle," Prog. Nucl. Energy, 83, pp. 283–293, (2015).

Cottrell, W. B., "Operation of the aircraft reactor experiment," Oak Ridge National Laboratory, (1959).

Churchill, S.W., and H. Chu, "Correlating equations for laminar and turbulent free convection from a horizontal cylinder," International journal of heat and mass transfer, 18, no. 9, pp. 1049-1053, (1975).

Davis, C., "Implementation of molten salt properties into RELAP5-3D/ATHENA," No. INEEL/EXT-05-02658. Idaho National Laboratory (INL), (2005).

Deb, K., S. Agrawal, A. Pratap, and T. Meyarivan, "A fast elitist non-dominated sorting genetic algorithm for multi-objective optimization: NSGA-II," In International conference on parallel problem solving from nature, pp. 849-858. Springer, Berlin, Heidelberg, (2000).

El-Wakil, M.M., "Nuclear Heat Transport," International Textbook Co., Scranton, PA, (1971).

Engel, J. and P, Haubenreich, "Temperatures in the MSRE during steady-state power operation," ORNL-TM-378, Oak Ridge National Laboratory, (1962).

Engel, J. R., H. F. Bauman, J. F. Dearing, W. R. Grimes, H. E. McCoy, and W. A. Rhoades, "Conceptual design characteristics of a denatured molten-salt reactor with once-through fueling," No. ORNL/TM-7207, Oak Ridge National Laboratory, (1980).

Ergen, W. K., A. D. Callihan, C. B. Mills, and D. Scott, "The Aircraft Reactor Experiment—Physics," *Nuclear Science and Engineering*, **2**, no. 6, pp. 826-840, (1957).

Fletcher, C.D., R.M. Beaton, D. Helton, and C.F. Boyd, "Evaluation of Uncertainties in SCDAP/RELAP5 Station Blackout Simulations," Information Systems Laboratory, Inc., RES-CO5-340, (2006).

Forsberg, C.W., "The advanced high-temperature reactor: high-temperature fuel, liquid salt coolant, and liquid-metal-reactor plant," Prog. Nucl. Energy, 47 (1–4), pp. 32–43, (2005).

Forsberg, C.W., P. Pickard, P.F. Peterson, "Molten-salt-cooled advanced high temperature reactor for production of hydrogen and electricity," Nucl. Technol, 144, pp. 289–302, (2003).

Fu, Z., F. Aydogan, R. Wagner, "Development of conservative form of RELAP5 thermal hydraulic equations, Proceedings of the ASME 2014 International Mechanical Engineering Congress & Exposition (IMECE2014)," November 14-20, 2014, Montreal, Canada, (2014).

Galvez, C., "Design and Transient Analysis of Passive Safety Cooling Systems for Advanced Nuclear Reactors," Ph.D. dissertation, University of California, Berkeley, (2011).

Gaston, D., C. Newman, G. Hansen, and D. Lebrun-Grandie, "MOOSE: A Parallel Computational Framework for Coupled Systems of Nonlinear Equations," *Nuclear Engineering and Design*, **239**, pp. 1768-1778, (2009).

Greene, S. R., J. C. Gehin, D. E. Holcomb, J. J. Carbajo, D. Ilas, A. T. Cisneros, V. K. Varma et al, "Pre-Conceptual Design of a Fluoride-Salt-Cooled Small Modular Advanced High-Temperature Reactor (SmAHTR)," Oak Ridge National Laboratory, ORNL/TM-2010/199, (2010).

Gruszczynski, M., and R. Viskanta, "Heat transfer to water from a vertical tube bundle under natural circulation conditions," ANL-83-7, Argonne National Laboratory, (1983).

Hallinan, K., and R. Viskanta, "Dynamics of a natural circulation loop: analysis and experiments," Heat Transfer Engineering, 7(3-4), pp. 43-52, (1986).

Haubenreich, P. N., and J. R. Engel, "Experience with the molten-salt reactor experiment," *Nuclear Applications and Technology*, **8**, no. 2, pp. 118-136, (1970).

Holcomb, D.E., S.M. Cetiner, G.F. Flanagan, F.J. Peretz, G.L. Yoder, "An Analysis of Testing Requirements for Fluoride Salt-cooled High Temperature Reactor Components," ORNL/TM-2009/297. Oak Ridge National Laboratory, Oak Ridge, TN, (2009).

Hu, R., "SAM user's guide for beta testing," Nuclear Engineering Division, Argonne National Laboratory, Lemont, IL, (2016a).

Hu, R., and T. Sumner, "Benchmark Simulations of the Thermal-Hydraulic Responses During EBR-II Inherent Safety Tests Using SAM," Proceeding of ICAPP'16, San Francisco, US, April 17-20, (2016b).

Hu, R., and Y. Yu, "Pseudo 3-D Full-Core Conjugate Heat Transfer Modeling of Sodium Fast Reactors," Proceeding of NURETH-16, Chicago, US, August 30- September 4, (2016c).

Sun, K., L. Hu, and C. Forsberg, "Neutronics feasibility of an MIT Reactor–driven subcritical facility for the Fluoride-salt–cooled High-temperature Reactor," *International Journal of Energy Research,* **41**, no. 14, pp. 2248-2257, (2017).

Ingersoll, D. T., C. W. Forsberg, L. J. Ott, D. F. Williams, J. P. Renier, D. F. Wilson, S. J. Ball et al, "Status of Preconceptual Design of the Advanced High-Temperature Reactor (AHTR)," United States. Department of Energy, (2004).

International Organization of Standards (ISO 5167-1) Amendment, "Measurement of fluid flow by means of pressure differential devices, Part 1: Orifice plates, nozzles, and Venturi tubes inserted in circular cross-section conduits running full," Reference number: ISO 5167-1:1991/Amd.1:1998(E), (1998).

Knoll, D., and D. Keyes "Jacobian-free Newton-Krylov Methods: A Survey of Approaches and Applications," Journal of Computational Physics, 193, pp. 357–397, (2004).

Langharr, H. and P. No, J. Appl. Mech., Sect. 3, 9, (1942).

Leandro, A., F. Heidet, R. Hu and R. Brown, "Thermal hydraulic model of the molten salt reactor experiment with the NEAMS system analysis module," Annals of Nucl. Energy, 126, pp. 59-67, (2019).

Lin, H. C., "RELAP5 Model Benchmark for Thermal Performance of DRACS Test Facilities," Electronic Thesis or Dissertation. Ohio State University, 2016. https://etd.ohiolink.edu/

Lin, H.C., S. Zhang, S. Shi, X. Sun, and R. Christensen, "Transient modeling of advanced high temperature reactor (AHTR) in RELAP5/SCDAPSIM/MOD 4.0," 26th International Conference on Nuclear Engineering. American Society of Mechanical Engineers Digital Collection (2018).

Lin, H.C., S. Zhang, D. Diamond, S. Bajorek, R. Christensen, Y. Guo, G. Yoder, S. Shi, Q. Lv, and X. Sun, "Phenomena identification and ranking table study for thermal hydraulics for Advanced High Temperature Reactor," Annals of Nuclear Energy 124: 257-269, (2019).

Lindauer, R.B., "Processing of the MSRE Flush and Fuel Salts," ORNL-TM-2578, Oak Ridge National Laboratory, (1969).

Lommers, L., and G. Honma, "NGNP High Temperature Materials White Paper," No. INL/EXT-09-17187. Idaho National Laboratory (INL), (2012).

Lv, Q., M. Chen, X. Sun, R. Christensen, T. Blue, G. Yoder, D. Wilson, and P. Sabharwall, "Design of fluidic diode for a high-temperature DRACS test facility," In: 21st International Conference on Nuclear Engineering, Chengdu, China, July 29–Aug 2, (2013).

Lv, Q., H.C. Lin, I.H. Kim, X. Sun, R.N. Christensen, T.E. Blue, G.L. Yoder, D.F. Wilson, P. Sabharwall, "DRACS thermal performance evaluation for FHR," Annu. Nucl. Energy 77, 115–128, (2015).

Lv, Q., H.C. Lin, S. Shi, X. Sun, R.N. Christensen, T.E. Blue, G.L. Yoder, D.F. Wilson, P. Sabharwall, "Experimental Study of DRACS Steady-State and Transient Performance," In: Proc. of ICAPP'16, San Francisco, CA, April 17–20, (2016).

Lv, Q., H.C. Lin., X. Sun, R.N. Christensen, T.E. Blue, G.L. Yoder, D.F. Wilson, P. Sabharwall, "Experimental Study of DRACS Thermal Performance in a Low- Temperature Test Facility". Nucl. Tech. 196 (2), 319–337, (2016).

Lv, Q., X. Wang, I.H. Kim, X. Sun, R.N. Christensen, T.E. Blue, G.L. Yoder, D.F. Wilson, P. Sabharwall, "Scaling analysis for the direct reactor auxiliary cooling system for FHRs," Nucl. Eng. and Des. 285, 197–206, (2015).

MacPherson, H. G., "The molten salt reactor adventure," *Nuclear Science and Engineering*, **90**, no. 4, pp. 374-380, (1985).

Marelli, S., and B. Sudret, "UQLab: A framework for uncertainty quantification in Matlab,". in: Proc. 2nd International Conference on Vulnerability and Risk Analysis and Management, Liverpool, United Kingdom, (2014).

Martínez-Quiroga, V., C. Allison, R. Wagner, F. Aydogan and S. Akbas, "NIRK3D and 3DKIN: General description and current status of the new 3D kinetics capabilities of RELAP5/SCDAPSIM/MOD4.0," In 11th International Topical Meeting on Nuclear Reactor Hydraulics (NUTHOS-11), Operation and Safety, Gyeongju, South Korea, October, (2016).

McKay, M., R. J. Beckman, and W. J. Conover, "Comparison of three methods for selecting values of input variables in the analysis of output from a computer code," Technometrics, 21, no. 2, 239-245, (1979).

NRC, "RELAP5/Mod3.3 code manual," Volumes I to VIII. NUREG/CR-5535/Rev 1, (2001).

NRC, "TRACE V5.0 Theory Manual, Field Equations, Solution Methods, and Physical Models," Office of Nuclear Regulatory Research, U.S. Nuclear Regulatory Commission, Washington, DC, (2008).

Perez, M., "Integration of a Quantitative-based Selection Procedure in an Uncertainty Analysis Methodology for NPP Safety Analysis," Thesis supervisor: F. Reventos Puigjaner, UPC, September, (2011).

Perez, M., C. Allison, R. Wagner, V. Martinez, Z. Fu, J. Hohorst and A. Abarca, "The development of RELAP/SCDAPSIM/MOD4. 0 for advanced fluid systems design analysis," In 23th International Conference on Nuclear Engineering (ICONE-23), Chiba, Japan, May, (2015).

Peterson, P. F., and Z. H. Zhao, "A flexible base-line design for the advanced high-temperature reactor utilizing metallic reactor internals (AHTR-MI)," In Proc., 2006 International Congress on Advances in Nuclear Power Plants (ICAPP'06), pp. 4-6, (2006).

Prince, B. E., S. J. Ball, J. R. Engel, P. N. Haubenreich, and T. W. Kerlin, "Zero-power physics experiments on the molten-salt reactor experiment," No. ORNL-4233, Oak Ridge National Laboratory, (1968).

Ren, W., G. Muralidharan, D. F. Wilson, and D. E. Holcomb, "Considerations of alloy N for fluoride salt-cooled high-temperature reactor applications," In ASME 2011 Pressure Vessels and Piping Conference, pp. 725-736. American Society of Mechanical Engineers Digital Collection, (2011).

Robertson, R.C., "MSRE Design and Operations Report, Part I, Description of Reactor Design," ORNL-TM-0728, Oak Ridge National Laboratory, (1965).

Robertson, R. C., "Conceptual design study of a single-fluid molten0salt breeder reactor," No. ORNL-4541. Comp, Oak Ridge National Laboratory, (1971).

Roglans, J., W. Ragland, D. Hill, "A PRA case study for extended long term decay heat removal for shutdown risk assessment," American Nuclear Society International Topical Meeting on Probabilistic Safety Assessment. American Nuclear Society, Clearwater Beach, FL, (1993).

Romatoski, R., and L. W. Hu, "Fluoride-salt-cooled high-temperature test reactor thermal-hydraulic licensing and uncertainty propagation analysis," Nuclear Technology, 1-18, (2019).

Sabharwall, P, S M. Bragg-Sitton, and C. Stoots, "Challenges in the development of high temperature reactors," Energy conversion and management, 74, pp. 574-581, (2013).

Scarlat, R., and C. Andreades, "Solid fuel, salt-cooled reactors," Molten Salt Reactors and Thorium Energy, pp. 435-474. Woodhead Publishing, (2017).

Shaffer, J. H., "Preparation and handling of slat mixtures for the molten salt reactor experiment," No. ORNL-4616, Oak Ridge National Laboratory, (1971).

Srinivasan, V., "Experimental and Numerical Investigation of Heat Transfer and Pressure Drop in Flow through Spirally Fluted Tubes," Ph.D. Dissertation, The Ohio State University, (1993).

Stempien, J. D., "Tritium Transport, Corrosion, and Fuel Performance Modeling in the Fluoride Salt-Cooled High-Temperature Reactor (FHR)," Ph.D. diss., Massachusetts Institute of Technology, (2015).

Sobol, I., "Global sensitivity indices for nonlinear mathematical models and their Monte Carlo estimates," Math Comput. Simulat., 55(1–3), pp. 271-280, (2001).

Sun, X., G.L. Yoder, R.N. Christensen, S. Shi, H.C. Lin, X. Wu, and S. Zhang, "Thermal Hydraulics Phenomena Identification and Ranking Table (PIRT) for Advanced High Temperature Reactor (AHTR)," (2017).

Todreas, N. and M. Kazimi. "Nuclear systems volume I: thermal hydraulic fundamentals," CRC press, (2011).

Trivedi et al, “Incorporation of lithium lead eutectic as a working fluid in RELAP5 and preliminary safety assessment of LLCS,” *Fusion Engineering and Design*, Volume 89, **12**, pp. 2956-2963, (2014).

Varma, V., D. Holcomb, F. Peretz, E. Bradley, D. Ilas, A. Qualls, and N. Zaharia, “AHTR mechanical, structural, and neutronic preconceptual design,” No. ORNL/TM-2012/320. Oak Ridge National Lab. (ORNL), Oak Ridge, TN (United States), (2012).

Wang, D., G. L. Yoder, D. W. Pointer, and D. E. Holcomb, “Thermal Hydraulics Analysis of the Advanced High Temperature Reactor,” Nuclear Engineering and Design, 294, pp. 73-85, (2015).

Williams, D., Assessment of Candidate Molten Salt Coolants for the NGNP/NHI Heat Transfer Loop,” ORNL/TM-2006/69. Oak Ridge National Laboratory, Oak Ridge, TN, (2006).

Wilks, S.S., “Determination of Sample Size for Setting Tolerance Limits, “Ann. Math. Stat, **13**, pp.91-96, (1941).

Wilks, S.S. “Statistical Prediction with Special Reference to the problem of Tolerance Limits,” Ann. Math. Stat., **13**, pp.400-409, (1942).

Wilson, G.E., B.E. Boyack, “The Role of The PIRT Process in Experiments, Code Development and Code Applications Associated with Reactor Safety Analysis,” Nuclear Engineering and Design, 186, pp. 23-37, (1998).

Zhang, D., and F. Rahnema, “Integrated Approach to Fluoride High Temperature Reactor Technology and Licensing Challenges (FHR-IRP),” No. 14-7829. Georgia Institute of Technology, (2019).

Zhang, S., X. Wu, S. Shi, X. Sun, R. Christensen and G. Yoder, “A coupled heat transfer and tritium mass transport model for a double-wall heat exchanger design for FHRs,” Annals of Nuclear Energy, 122, pp. 328-339, (2018).

Zhang, S., H.C. Lin, X. Wu, J. Mao, H. Sun, K. Cheng and X. Sun, “Design of a Direct Reactor Auxiliary Cooling System (DRACS) considering tritium management for Advanced High-Temperature Reactor (AHTR),” 18th International Topical Meeting on Nuclear Reactor Thermal Hydraulics (NURETH-18), Portland, OR, August 18-23, (2019).

Zou, C. Y., C. Z. Cai, C. G. Yu, J. H. Wu, and J. G. Chen, “Transition to thorium fuel cycle for TMSR,” *Nuclear Engineering and Design*, **330**, pp. 420-428, (2018).

Zweibaum, N., Z. Guo, L. Huddar, and P. Peterson. "Validation of best estimate models for fluoride-salt cooled, high-temperature reactors using data from the compact integral effects test (CIET 1.0) facility." In 16th International Topical Meeting on Nuclear Reactor Thermal Hydraulics (NURETH-16) Chicago, USA, (2015).

Zkauskas, A., “Heat transfer from tubes in cross flow,” Adv. Heat Transfer, 18, pp. 87–159, (1987).